1-1-2013

Structural Health Monitoring of Concrete Systems

Matthew Kelly Jones
University of South Carolina - Columbia

STRUCTURAL HEALTH MONITORING OF CONCRETE SYSTEMS

by

Matthew K. Jones

Bachelor of Science
University of South Carolina, 2012

Submitted in Partial Fulfillment of the Requirements

For the Degree of Master of Science in

Civil Engineering

College of Engineering and Computing

University of South Carolina

2013

Accepted by:

Paul Ziehl, Director of Thesis

Juan Caicedo, Reader

Fabio Matta, Reader

Lacy Ford, Vice Provost and Dean of Graduate Studies

DEDICATION

I proudly dedicate this work to my family for their continued love and support. I would especially like to thank my loving mother for being the best mom a son could ask for. Thanks for being awesome Mom. I want to think my father for encouraging me to pursue an education in engineering and for supporting me throughout my time as a student as well as being the person I have looked up to all my life.

ACKNOWLEDGEMENTS

I would like to express the deepest appreciation to my graduate advisor Dr. Paul Ziehl for giving me the opportunity to be a part of his esteemed research team. I consider myself very much improved having had the chance to work with Dr. Ziehl and it is a great honor to have been one of his graduate students. Without his generosity, guidance, and persistent support this thesis would not have been possible.

I would also like to acknowledge and kindly thank my colleagues for all of their assistance during my graduate study including: Dr. Mohamed ElBatanouny, Dr. Aaron Larosche, Dr. Peter Yu, Dr. William Velez, Mr. Michael Miller, Mrs. Marwa Abdelrahman, and Mr. Clark Baer.

I would like to extend a sincere thanks to Dr. Charles Pierce for allowing me to work with him on several rewarding research projects during my undergraduate study.

I would also like to thank my high school construction technology teacher, mentor, and friend Mr. Tommy Maynard for believing in me and for giving me a firm but caring push in a better direction. I am very fortunate to have had the pleasure of knowing Mr. Maynard and being one of his students.

Also a kind thanks to Mr. Eddie Deaver of Holcim Cement for his valuable input regarding this research project.

ABSTRACT

Concrete material is widely used around the world for the construction of many infrastructure including highway bridges, residential and commercial building, dams, electric power generation plants, and nuclear power plants. It is therefore practical to continue development of both improved structural systems as well as innovative condition assessment techniques for new and existing concrete structures. This thesis includes two studies which focus on structural health monitoring of concrete systems. The first project deals with performance assessment of an in-situ precast approach slab system and the second is an investigation of acoustic emission (AE) as a condition assessment technique for alkali-silica reaction (ASR) in concrete.

The first study is aimed at investigating the performance of precast concrete slabs placed on the approaches of a replacement bridge in Union County, S.C. The use of full depth precast panels in bridge construction has been limited by problems associated with the durability of connection joints between adjacent panels. The precast slabs being monitored are designed and constructed using an improved longitudinal joint detail consisting of interlocking looped reinforcement bars. The purpose of this research program is to assess the practicality of further implementation of approach slab system as an alternative to current construction methods. To evaluate the effects of service loads the approach slabs were instrumented with strain and displacement gages and measurements were collected periodically for a period of 18 months. A series of load tests were also

performed on the approach slab system. Results of long-term monitoring and load tests show no adverse indications and the approach slabs appear to be functioning adequately.

In the second study an accelerated alkali-silica reaction (ASR) test was designed to examine the ability of acoustic emission (AE) to detect this damage mechanism. ASR is a chemical reaction occurring between alkaline hydroxides within cement past and certain types of amorphous silica found in mineral aggregates. ASR causes an accumulation of internal pressure due to the formation of a hygroscopic gel which leads to expansion and cracking of the concrete. AE is highly sensitive to stress waves emitted from a sudden release of energy such as formation of cracks in concrete. This allows it to capture and identify propagating damage. AE has the potential to detect micro-cracks forming prior to expansion, which can be related to the degree of ASR damage. The experimental setup consisted of an adapted ASTM C1293 test, twelve specimens of dimensions 3x3x11.25 in. created using a highly reactive aggregate as well as an elevated alkaline content, and 3 control specimens of similar dimensions incorporating innocuous aggregates and low-alkaline cement. The specimens were placed in controlled environment with high temperature and relative humidity to accelerate the ASR reaction. Length change measurements and petrographic examination were performed periodically to detect ASR damage while AE activity was recorded continuously. The results of this study show that AE has the ability to detect ASR damage with a good agreement with length change measurements. Furthermore, AE cumulative signal strength can be related to the length expansion associated with ASR distress and the intensity analysis chart has the potential to classify ASR damage in concrete structures.

TABLE OF CONTENTS

LIST OF TABLES

LIST OF FIGURES

CHAPTER 1

INTRODUCTION

1.1 LAYOUT OF THESIS

The thesis consists of five chapters. Chapter 2 provides a brief review of the pertinent topics focused on in this thesis including: full depth precast concrete panel systems, alkali-silica reaction (ASR) in concrete, and acoustic emission (AE) along with basic AE parameters.

Chapters 3 and 4 are both written in paper form. The paper in Chapter 3 is to be submitted to the South Carolina Department of Transportation (SCDOT) as a deliverable engineering report. The paper in Chapter 4 is to be submitted as a report or for publication as a journal article.

Chapter 3 is titled "Performance Assessment of In-situ Precast Approach Slab Systems", where an overview of a SCDOT sponsored precast approach slab long-term monitoring project is presented including results of in-situ behavior and load testing.

The title of Chapter 4 is "Assessment of Alkali-Silica Reaction Using Acoustic Emission". In this chapter the ability of AE to detect ASR related damage in concrete is discussed and the applicability of AE as a condition assessment technique for structures subject to ASR is addressed.

A summary along with the main findings of the studies discussed in this thesis is presented in Chapter 5. Some recommendations for future researchers are included in this chapter.

1.2 PERFORMANCE ASSESSMENT OF IN-SITU PRECAST APPROACH SLAB SYSTEMS

As the interstate highway system deteriorates, total vehicle miles traveled steadily increases, and the consequence of congested roadways represents a progressively significant burden to economies around the world the need arises to expedite roadway and bridge construction projects. Bridge deck maintenance and replacement account for a large part of highway construction which can result in thousands of hours of delays due to full and partial closures of arterial roadways. The use of prefabricated bridge construction techniques offers the opportunity for minimizing traffic delays, improving work zone safety, and lowering cost. Precast concrete panels are commonly used in a variety of ways including buildings, roadbeds and bridge decks (PCI 1999). Precast concrete offers a substantial time savings in the construction schedule in comparison to cast-in-place concrete. Furthermore setting of precast concrete structural elements is not impeded by inclement weather conditions, such as rain or snow and cold temperatures, which can delay casting of concrete on-site indefinitely. Precast concrete manufacturing also allows for strict quality control and as a result precast panels offer increased strength, durability, and lower creep deformation (PCI 1999).

Although precast concrete offers major advantages for the construction of highway bridge decks their use has been somewhat limited. The primary reason for this are concerns regarding design and construction issues. A common concern is perceived durability problems of the longitudinal and transverse joints connecting adjacent precast panels. Historically, the primary reason for precast bridge deck deterioration is the differential movement in longitudinal and transverse panel joints which leads cracking,

leaking, and ultimately major degradation. Differential joint deflections can be a result of design, improper construction procedures, material selection, overloading, or lack of maintenance. Once cracking occurs ingress of water begins and further deterioration of the joint occurs. The progressive corrosion of reinforcing steel within the joint detail is a particular problem because it exacerbates relative displacements between panels and invites additional cracking and deformation which usually manifests at the roadway surface. The deterioration of precast panels can result in costly repairs or even replacement and more periodic resurfacing of the pavement surface.

This purpose of this research program is to investigate the performance of precast concrete slabs placed on the approaches of a replacement bridge over Big Brown Creek on River Road (S-86) in Union County, S.C. The project is sponsored by The South Carolina Department of Transportation (SCDOT) through The Federal Highway Administration's (FHWA) Innovative Bridge Research and Deployment Program (IBRD).

The approach slabs were fitted with an improved longitudinal shear key detail consisting of lopped interlocking reinforcement bars. SCDOT is considering the use of this structural system in the future for bridge construction. This research program aims to assess the performance of the precast concrete approach slab system and determine the practicality of further implementation as an alternative to current joint designs which historically have been subject to durability problems. Emphasis is placed on the potential changes in long-term behavior of the approach slab systems due to service loadings.

Strain and displacement gages were installed inside the precast approach slabs and on the bridge approach to evaluate the effects of service loads on the bridge approach.

The structural behavior of the precast approach slabs is to be monitored while in service for a period of 18 months immediately after bridge construction is complete. During that time strain and displacement measurements are to be collected periodically as well as during scheduled dynamic and static loading events with loading trucks. Details regarding the type and location of sensors used for monitoring as well as tasks performed by personnel from the University of South Carolina (U.SC) during instrumentation of the precast approach slab system, data acquisition, and load testing methodology are presented. Initial readings and readings taken during the first 6 months of service have been collected along with visual inspections conducted during scheduled site visits. Concrete cylinders were sampled from each batch of concrete used during the casting of the approach slabs as well as the shear key closures adjoining each slab. Concrete cylinders were tested for compressive strength and modulus of elasticity in order to assess the condition of the approach slabs.

1.3 ASSESMENT OF ALKALI-SILICA REACTION USING ACOUSTIC EMISSION

Concrete is widely used around the world for the construction of many infrastructure including highway bridges, residential and commercial building, dams, electric power generation plants, and nuclear power plants. The heterogeneous nature of concrete makes it susceptible to various deterioration mechanisms including corrosion of reinforcement, sulfate attack, alkali-aggregate reaction (AAR), freeze-thaw cycling, leaching, radiation, elevated temperatures, salt crystallization, and microbiological attack (Clifton 1991). Concrete deterioration may jeopardize the serviceability and safety of structures leading to economic losses and ultimately catastrophic failures and fatalities. It

is, therefore, necessary to evaluate the condition of aging concrete structures in order to predict their remaining service life.

The presence of cracks from alkali-silica reaction (ASR) at the Seabrook Nuclear Power Plant (NRC 2011) has brought this type of deterioration of reinforced concrete to the attention of the general public. ASR is a mechanism that depends on material selection of the concrete matrix and permits few mitigation techniques once the structure is in-service. This prompted the U.S. Nuclear Regulatory Commission (NRC) to issue a nationwide warning to all NPPs operators.

Currently the most prevalent means of preventing ASR is proper selection of materials. Most commonly a potential aggregate is screened for ASR subjectivity using laboratory testing procedures. It is noted that the concrete used in the Seabrook Nuclear Power Plant was examined using ASTM C289 and ASTM C295, which are the standards used at the time of construction to detect ASR, yet ASR degradation still occurred. The ASTM C1293 and the ASTM C1260 are the two most popular test methods being used today to evaluate the potential of an aggregate to participate in expansive ASR. Although these methods show a much improved ability to identify aggregates subject to ASR than previous test method, each has limitations. Both the ASTM C1293 and the ASTM C1260 have been shown to falsely identify aggregates as innocuous and conversely reject certain aggregates which have shown satisfactory field performance. It is for this reason that even careful material selection cannot completely eliminate the incidence of deleterious ASR in the field.

ASR initiates when certain types of reactive siliceous aggregates are combined with cement alkaline hydroxides originating from Portland cement. The mechanism requires

as little as 80-percent relative humidity to occur. The reaction product is a gelatinous material that swells when moisture is absorbed and can cause expansion and cracking in concrete structures.

Regular inspections are needed to determine the extent and rate of ASR deterioration. This can be achieved through examination of concrete cores to determine the mechanical properties of concrete as well as in-situ monitoring through crack mapping. However, visual inspection gives only information related to the surface condition of concrete. Therefore, there is a need for an efficient non-destructive testing (NDT) method to monitor the progression of ASR. The NDT technique should enable (1) proper assessment of the rate of ASR deterioration and (2) evaluate the remaining service life. Acoustic emission (AE) method has advanced significantly in the past years as a real-time, passive NDT technique for evaluating damage in concrete structures which paves the way for developing a quantitative method for evaluating ASR (Ziehl 2008). AE is highly sensitive to stress waves emitted from sudden release of energy, such as concrete cracks (Pollock 1986; Ziehl 2008). This allows it to capture and identify propagating damage (ElBatanouny et al 2012; Mangual et al. 2013). Possible applications of AE monitoring related to the progression of ASR include long-term monitoring and prognosis based on received AE data using parameter based methods.

An accelerated ASR test (modified ASTM C1293) was designed to enable detection of ASR expansion in a reasonable time frame. The specimens were continuously monitored using AE. Expansion measurements were performed periodically using a length comparator along with petrographic examination to serve as a benchmark for ASR detection. The objective of the research is to use AE to assess the development

and rate of ASR distress in concrete for use in service life modeling. The results of the test showed the ability of AE to detect ASR progression with a good agreement with length change measurements. The results of petrographic examination of the specimens are to be reported on in the future.

CHAPTER 2

LITERATURE REVIEW

2.1 FULL DEPTH PRECAST CONCRETE BRIDGE PANELS

Precast concrete elements began being integrated into bridge construction standards around the late 1960's primarily because of the ease of construction and increase in productivity they can provide. By the 1980's full depth precast concrete deck panels were being used in construction of bridges by a variety of Department of Transportations (DOTs) around the U.S. Notable bridge design projects that incorporate the use of full depth deck precast panels include the Woodrow Wilson Bridge in Washington D.C (Chi et al. 1985) and the Oakland-San Francisco Bay Bridge.

During the 1990's a movement toward rapid construction methods as well as stronger and more durable infrastructure gained momentum and the Federal Highway Administration's (FHWA) Innovative Bridge Research and Construction (IBRC) helped fund DOTs around the U.S. in an effort to develop innovative bridge design and construction ideas. Full depth precast panels are an ideal choice to satisfy the need for rapid construction and, if properly designed and constructed, they can offer increased strength and durability over other construction methods.

Full depth precast panel replacements began incorporating rapidly curing materials and rigidly sequenced construction practices. Various full depth, rapid construction standards were developed in 1995 and are still in use today including grouted female to female transverse joint connections (Issa et al. 1995). Research continued on full depth

bridge deck panels using female to female connections during the late 1990's and early 2000's (Markowski 2005). Around this time, due to speed of construction, precast panels incorporating similar female-to-female joint connections began to be used as paving and for bridge approaches as well (Merritt et al. 2000).

Dr. Mohsen A. Issa et al distributed a survey to 53 DOTs in the mid 1990's aimed at gauging the overall prevalence of use and performance characteristics of full depth precast concrete deck panels in the U.S. and Canada. Of the 51 DOTs that responded 13 had used full depth precast panels. The results of the survey were reported along with the details pertaining to each of the various construction projects. The type and number of precast deck panels used is shown in Table 2.1. Specifics regarding the current condition of each precast bridge deck project are shown in Table 2.2. The DOT survey requested information pertaining to the age of the bridge deck, any problems that may have been encountered, and the respective causes of those problems.

Out of 9 reported DOT projects, 5 showed various structural problems. All 5 projects with problems reported leaking at the transverse and longitudinal joints as the major issue. The main cause for these problems was perceived as being related to construction procedures. However, only 2 structures were reported as having major deterioration but both were in service for over 10 years.

The use of cast-in-place concrete is prevalent for bridge approach construction. A common serviceability problem encountered with cast-in-place bridge approaches is differential settlement of the paved section of the roadway relative to the foundation supported bridge deck. The use of precast panels on bridge approaches has been somewhat limited by the perceived durability issues associated with the connection

adjoining adjacent panels. However, precast concrete offers overall advantages in both strength and durability over cast-in-place concrete if designed and implemented properly. Recently the use of an improved precast panel connection detail has been investigated that may mitigate the issues that have plagued these systems in the past (Li et al. 2010).

Table 2.1: Results of DOT Survey (Issa et al. 1995)

DOT	# Bridges	Type of Construction			
		Precast Panels	Precast/Prestressed Panels	Rehab	New
Alaska	19		X	X	
Maine	1 - 5	X		X	
Indiana	2		X		X
Washington	> 5		X		X
California	1 - 5	X		X	X
Iowa	1 - 5	X			X
Connecticut	1 - 5		X	X	
Maryland	2		X	X	
New York	12	X	X	X	
Ohio	1 - 5	X		X	
Illinois	2		X	X	
Ontario	1 - 5	X		X	
Texas	1	X		X	
Virginia	2	X		X	

Table 2.2: Precast deck problems (Issa et al. 1995)

DOT		AK	ME	IN	WA	IW	CT	IL	CA	MD
Age (yrs)		1.5	4.5	24	7		4	7	15	10
Problems	Cracking	NONE	X		NONE	UNDER CONSTRUCTION	NONE		X	X
	Leaking		X	X				X	X	X
	Settlement									
	Deterioration								X	X
Reason	Material Quality		X						X	
	Maintanence									
	Construction Procedures		X	X				X	X	X

Currently the most common female-to-female connection joint used for precast concrete panels consists of welded steel connectors usually spaced at 4 ft as well as a grouted shear key. Figure 2.1 shows a typical longitudinal joint detail for a deck bulb tee bridge system (Stanton and Mattock 1986; Ma et al. 2007). To make the connection between panels two steel angles are anchored into the top flange of the precast panel and a steel connector plate is welded to either side of the imbedded steel angles. In between the pockets around the welded steel connectors a grouted shear key is provided along the length of the joint. Grout is placed around the welded steel connectors and within the shear keys in order to tie the adjacent panels together. A backer bar is placed in the bottom of the shear key to prevent drainage of the low-slump grout.

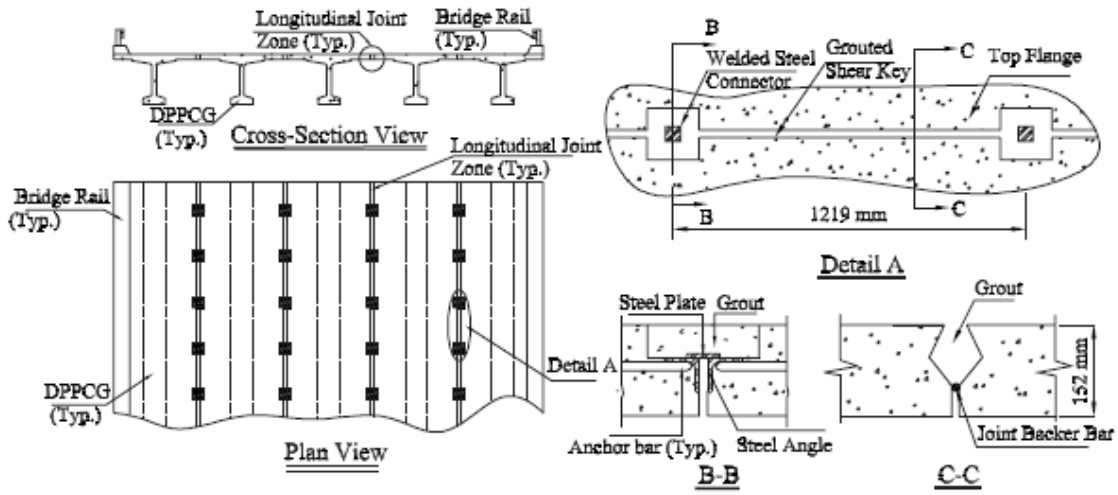

Figure 2.1: Typical longitudinal joint connection with welded steel plates and grouted shear key (Stanton and Mattock 1986; Ma et al. 2007)

The current connection joint general provides the capacity needed to transfer shear forces and a negligible amount of moment from one panel to the next. The spacing and location (mid-depth) of the welded steel plates limits their ability to control cracking due

to flexure. Although this connection joint detail has been used successfully in some cases, problems with crack and deformation around joints has been reported (Stanton and Mattock 1986: Martin and Osborn 1983). Cracking around joints and the related deterioration associated with water infiltrating joints is considered the primary issue inhibiting more widespread use of precast bridge deck systems.

The improved connection joint detail consists of interlocking looped (U-bar) reinforcement bars oriented transversely, relative to the joint, along with a female-to-female shear key as well as two longitudinal reinforcing bars. The U bars are spliced with the transverse reinforcement within the precast panel and have a 0.625 in. diameter (#5). The two longitudinal reinforcing bars have a 0.75 in. diameter (#6) and are located in the middle (plan view) of the joint and tied on the inside of the loop bars at top and bottom. The loop bars have an even spacing where each panel is completely out of phase with the adjacent panel by a half space. A photograph of the longitudinal connection detail is shown in Figure 2.2. The improved connection joint has the potential to more effectively transfer and distribute shear and moments between adjacent panels and therefore enhance the strength and durability of precast bridge deck structures.

The continued development of rapid bridge construction techniques and materials is necessary to provide higher quality, faster construction, minimized traffic disruption, and increased durability and life cycle of bridges. Various state DOTs and research teams around U.S. are currently investigating innovative materials and methods to expedite construction and reduce traffic delays.

Figure 2.2: Improved connection shear key joint detail

2.2 ALKALI-SILICA REACTION

Alkali-silica reaction (ASR) is one of the primary chemical reactions causing degradation and loss of service of hardened concrete structures worldwide. ASR is a reaction that occurs over time in concrete between aqueous alkaline hydroxides within the pore solution of the cement paste (Na_2O and K_2O) and amorphous silica within surrounding aggregates (Swamy 1998). This reaction causes the formation of a viscous alkali silicate gel which expands in the presence of water. The accumulation of expansive pressure created by the hydrated alkali silicate is widely believed to induce the deleterious micro-cracking of aggregates and subsequently of surrounding cement paste matrix. The presence of cracks encourages additional ingress of alkaline pore fluid and thus further exacerbates the ASR reaction and resulting damage. If left uninhibited ASR can lead to severe damage of concrete structures. ASR is typically characterized by map cracking (Figure 2.3), spalling of joints, large movements of affected areas, and

ultimately loss of service and safety of a structure. In some cases demolition of affected areas of a structure may be required.

Figure 2.3: Map cracking of ASR affected barrier parapet

Since its discovery in the 1940 by Stanton (Stanton 1940) ASR has been identified by countries all over the world as a serious concrete durability problem. As a result ASR has been the source of a significant body of research and many discoveries have been made regarding the mechanisms that cause ASR induced expansion and measures by which ASR can be mitigated through proper materials selection and concrete mixture design. Some common measures available to prevent ASR expansion and cracking are use of: low-alkalinity cements, aggregates containing non-reactive minerals, supplementary cementitious materials, and lithium compound admixtures.

If a potentially reactive aggregate is to be used in a concrete structure the most common means of preventing deleterious ASR is the use of low-alkaline cements and the addition of natural pozzolans, such as fly ash, silica fume and slag, as replacement for a portion of the cement. Effective mitigation techniques are very important in order to reduce cost of construction in regions where local aggregates are potentially ASR prone.

Currently one of the most efficient and prevalent practices for preventing ASR related damage in concrete is identifying the susceptibility of aggregates for ASR reactivity. Several test methods have been developed and are currently in use to evaluate an aggregates potential for participation in expansive ASR. Each test method has limitations and many studies are still being conducted in an attempt to develop more accurate and efficient testing protocols for evaluating concrete aggregates subject to ASR.

2.2.1 Alkali-Silica Reaction Mechanisms

Despite being studied so heavily some aspects of the mechanisms causing ASR expansion and cracking are not well understood. In general for ASR to occur three conditions must exist: a high alkaline environment, reactive silica, and moisture.

Reactive silica commonly occurring in various types of minerals reacts with hydroxyl ions present in pore solution of cement matrix. The silica now dissolved in pore fluid is available to react with sodium (Na^+) and potassium (K^+) alkalis. The reaction causes the formation of a volumetrically unstable hygroscopic alkali silica gel. For the sake of simplicity the reaction can be schematically represented as the following (Farney 1997):

Step 1:

Silica + alkali → alkali-silica gel (sodium silicate)

$SiO_2 + 2NaOH + H2O \rightarrow Na_2SiO_3.2H_2O$ (2KOH can replace 2NaOH)

Step 2

Gel reaction product + water →expansion

Once the alkali silicate gel is hydrated it begins to expand and causes the development of internal stresses within the cement matrix and surrounding aggregates.

Expansive pressure continues to accumulate as the bulky alkali silicate gel absorbs water until the tensile limit of the concrete is exceeded. Micro-cracking ensues leading to additional ingress and absorption of water, additional gel formation, and eventually failure of the concrete occurs. A polished section of concrete showing ASR related cracking is shown in Figure 2.4 (Winter 2012).

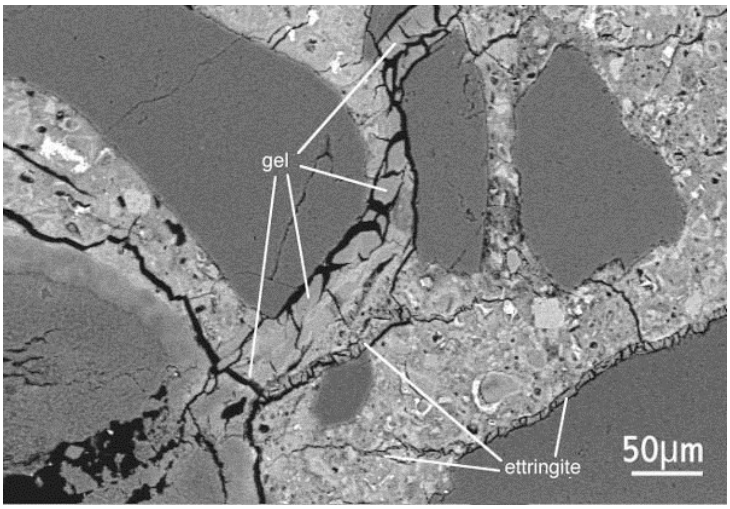

Figure 2.4: Detail of an ASR affected concrete specimen (Winter 2012)

Silica (silicon oxide tetrahedron) can be found in many commonly occurring natural aggregates. The silicon tetrahedron, shown in Figure 2.5, consists of 4 oxygen ions (O^{2-}) bonded to a single silicon ion (Si^{4+}) located in the center of the structure (Leming 1996). A crystalline network is formed in three-dimensional space by the repetition of the silicon tetrahedron (Prezzi et al. 1997). Each oxygen ion is bonded to two silicon ions in order to achieve electrical neutrality. The chemical bonding in crystalline silica shows the ordered regularity of a lattice, whereas non-crystalline silica has more the appearance of a random network. The geometry of crystalline and amorphous lattice structures is shown in Figure 2.6.

Complete tetrahedra cannot form at the surface of the crystalline structure and therefore bonds between oxygen and silicon are broken resulting in charges that are unsatisfied (Prezzi et al. 1997). Regardless crystalline silica structures are chemically and mechanically stable, impermeable, are only reactive at the surface (Leming 1996). Non-crystalline or amorphous silicates are formed when the linking of tetrahedral is random forming a structure that is much more porous and has much larger surface areas. As a result amorphous silica is very reactive. The crystalline structure of silicates is formed when melted silica cools and hardens. The rate of cooling strongly influences the forming of crystals. Rapidly cooled silicates are often non-crystalline to some extent. In general the more amorphous the silica is the more reactive it becomes.

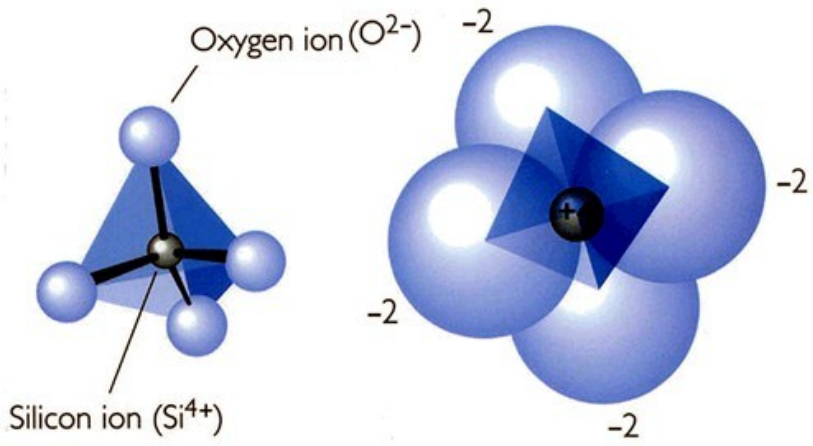

Figure 2.5: Silicon tetrahedron

Another factor influencing the ASR reactivity is the amount of energy stored in the crystalline structure of an aggregate. Various silica structures through heat and pressure may develop large amounts of stored strain energy. Many ASR prone aggregates contain these types of silicates. However these aggregates react with alkaline hydroxides at a much slower rate than that of amorphous silicates. Metamorphic aggregates containing strained quartz are an example of such aggregates (Leming 1996).

Additionally some crystalline silicates, such as chert, contain very fine crystals with very large surface areas and as such are very prone to ASR (Leming 1996).

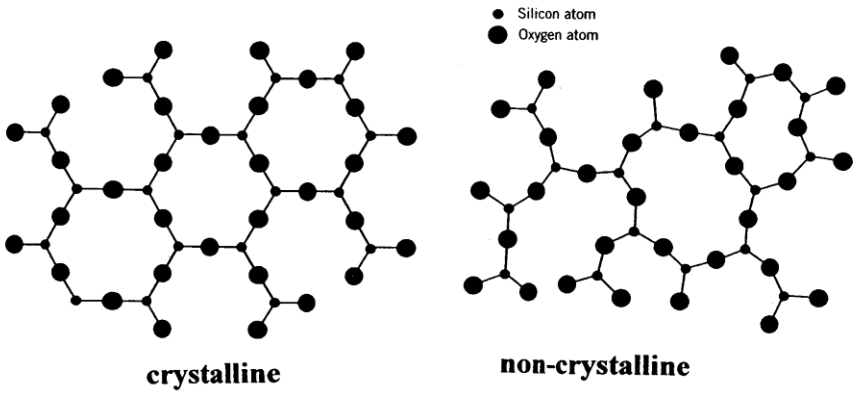

Figure 2.6: Silicon tetrahedron lattice structures

Two conditions that have also been proven to influence ASR induced expansion are the size and proportion of reactive aggregates. A certain proportion of some reactive siliceous aggregate was shown by Stanton to cause the largest expansion in concrete. He further demonstrated that expansion decreased when the content of reactive aggregate in the concrete was increased or decreased from that pessimum proportion (Stanton 1940). Stanton also showed that ASR induced expansion was largest at a certain grain size for a given proportion of reactive aggregate and expansion decreased when the grain size was increased or decreased from that pessimum size (Stanton 1940).

2.2.2 Laboratory Testing Procedures

This section presents a brief description of the most popular testing methods for evaluating the potential of aggregates for ASR reactivity.

2.2.2.1 *ASTM C295: "Guide for Petrographic Examination of Aggregates for Concrete"*

The ASTM C295 test method is used to determine the physical and mineralogical characteristics of aggregates. Typically the petrographic examination requires the use of optical microscopy to classify different rock types and mineral constituents within an aggregate. Identifying constituents of an aggregate is generally a necessary step in determining the properties that may be expected to influence behavior, such as ASR subjectivity, during intended use. Because potentially deleterious minerals such as reactive silica present in an aggregate can be identified using petrographic examination it is commonly used as a criterion in the proper selection of materials in order to prevent ASR. However petrography is limited in that certain types of slowly-reactive minerals such as microcrystalline, strained, or microfractured quartz cannot be clearly identified and these minerals are commonly occurring in a wide variety of aggregates. Another drawback to the C295 is that the interpretation of results can vary widely depending on the petrographers experience level and background.

2.2.2.2 *ASTM C227: "Standard Test Method for Potential Reactivity of Cement-Aggregate Combinations (Mortar-Bar Method)"*

The ASTM C227 is a test method that is used to determine the susceptibility of cement-aggregate combinations to expansive alkali-aggregate reactions including ASR. This test has been proven as inadequate in identifying certain slowly reactive aggregates such as greywackes and argillites (Bérubé and Fournier 1992). Storage containers containing wicks have been shown to cause leaching of alkalis from mortar bars causing seemingly innocuous expansions. The alkali content of cement, which is not specified in

this test, has been shown to largely affect expansion results. Furthermore the water-cement ratio has been shown to influence the amount of ASR expansion observed. The C227 does not have a specified water-cement ratio and as a result a wide range of expansion results can be observed using a single aggregates source.

2.2.2.3 ASTM C289: "Standard Test Method for Potential Alkali-Silica Reactivity of Aggregates (Chemical Method)"

The ASTM C289 is a test method covering the chemical determination of the potential reactivity of an aggregate with alkalis in cement. The test setup consists of crushing aggregates to a passing 300-µm sieve and retained on 150-µm sieve size and then exposing them to a 1 *N* sodium hydroxide solution at a temperature of 80° C for a 24 hour period. After the aggregate is immersed for 24 hours the solution is then filtered and analyzed for the content of dissolved silica and the amount of alkalinity consumed. These two parameters are then plotted on a standard graph with regions defined for innocuous, deleterious, and potentially reactive behavior. Many aggregates are not accurately identified using this test method. A substantial number of well-known ASR reactive aggregates have been shown to pass this test while many innocuous aggregates are identified as deleterious. The interference of certain minerals, such as calcium, magnesium, silicates, gypson, zeolites, clay minerals, organic matter, or iron oxides, have been shown to cause erroneous results (Touma et al. 2001). Concrete aggregate gradation and proportioning in mixture design has been shown to strongly influence ASR expansion (Stanton 1940). For this reason the crushing and preparation of aggregates in this test has been criticized as a significant source of error because aggregate sizes used in typical concrete mix designs are not well represented.

2.2.2.4 *ASTM C1260: "Standard Test Method for Potential Alkali Reactivity of Aggregates (Accelerated Mortar Bar Method)"*

The ASTM C1260 is a test method which permits the detection within 16 days of the potential of an aggregate in mortar bars to develop deleterious ASR expansion. The test is has been proven to be especially useful for aggregates that react slowly or produce expansion late in the reaction. The ASR reaction is accelerated by exposing mortar bars to a 1*N* sodium hydroxide solution which is kept at 80° C. The alkaline soaking solution provides the mortar bars with essentially and 'unlimited' supply of hydroxides in order to accelerate the reaction. This test is considerably valuable because it provides a rapid means of evaluating potentially reactive aggregates for use in concrete. However, this test method has been reported by many researchers as very severe and it has been shown in the past to identify aggregates as reactive that have good long-term service records. Furthermore, recently a group of aggregates shown to be innocuous using the ASTM C1260 developed substantial ASR related damage in the field. In general the ASTM C1260 is commonly used in conjunction with other criteria in order to establish whether an aggregate is suitable or not.

2.2.2.5 *ASTM C1293: "Standard Test Method for Concrete Aggregates by Determination of Length Change of Concrete Due to Alkali-Silica Reaction"*

The ASTM C1293 is a test method that is used to determine, through the measurement of length change of concrete prisms, the susceptibility of a sample of an aggregate for participation in expansive ASR. Commonly referred to as "The Concrete Prism Test" (CPT), this method was developed in order to overcome the failure of the ASTM C227 to accurately identify aggregates subject to ASR (Thomas et al. 2004). The C 1293 is used

to predict the reactivity of an aggregate by monitoring the volumetric expansion of 3" x 3" x 11.25" concrete prisms. Prisms are to have a w/c ratio ranging from 0.42 to 0.45 and a total cement content of 420 kg/m^3. The cement should be a Type 1 ordinary Portland cement conforming to ASTM C150 and should have a total alkali content of at least 0.9% Na_2O_{eq}. Alkali content of the concrete is increased to 1.25% Na_2O_{eq} using a sodium hydroxide (NaOH) admixture. Specific proportions and gradation of course and fined aggregate are also identified. After casting and setting for a period of 24 hours the prisms are demolded and placed in a controlled laboratory environment for a period of one year while comparatory length change measurements are collected. Temperature and relative humidity are maintained at 100° F and 100% respectively. An aggregate is considered potentially deleterious if the expansion after a one year period is equal to or greater than 0.04%.

The CPT offers several advantages over other methods. One of the primary benefits of using this method as opposed to the AMBT is that concrete containing aggregate with gradations more representative of typical mixture designs used for field applications can be tested. Also the method has the advantage of considering cement-aggregate combinations and, further, is much less severe than the exposure conditions of the AMBT and is therefore more representative of field conditions. The primary disadvantage of the CPT is the much longer testing period required than that of the other methods. Also some investigators have shown that CPT expansion results can be substantially influenced by leaching of alkalis from concrete specimens, specifically that leaching of alkalis can decrease the rate, duration, and maximum expansion due to ASR (Rivard et al. 2003).

Much like the ASTM C1260 this test does not duplicate field conditions and as such actual field behavior of aggregates subject to ASR may not be well represented. It is therefore important that the ASTM C1293 be used as a criterion, in conjunction with other practices, to evaluate reactivity of aggregates. Nevertheless the ASTM C1293 has been shown to provide the best correlation with actual field performance and is currently regarded as the most authoritative test for evaluating aggregates for ASR.

2.2.3 Field Assessment of ASR

Current methods used for assessing concrete damage in a field structure mainly rely on visual inspections performed at regular intervals. These inspections provide critical information on the structure condition; however, this information is rather qualitative and it strongly depends on the experience and skill of the inspectors. Furthermore, only the exterior body is inspected. Coring is then usually required. Several tests, such as compressive strength, can be conducted on cores but their sensitivity and reliability regarding ASR may vary significantly (Stanton 1940; Swamy 1998). In fact, there is no universal procedure to assess and quantify damage associated with ASR.

2.2.4 Conclusions

The limitations associated with existing laboratory tests prove that an ideal or all-encompassing method for predicting ASR reactivity of aggregates does not currently exist. More comprehensive investigation of test methods and the mechanisms that cause ASR induced expansion is required in order to develop a singular approach to identifying the susceptibility of aggregates for ASR reactivity. Presently the best means of preventing deleterious ASR, with great certainty, is to select aggregates that have good long-term service records. However, this is not always possible due to regional

availability of aggregates. In addition, current condition assessment methods for existing concrete structures that may be subject to ASR are primarily limited to visual inspections or destructive testing methods. Visual inspection gives only information related to the surface condition of concrete and in some cases, such as NPPs, visual inspection or coring is highly prohibitive. Therefore, there is a need for an efficient non-destructive testing (NDT) method to monitor the progression of ASR in concrete structures.

2.3 ACOUSTIC EMISSION

Acoustic emission is founded upon the phenomena whereby acoustic waves are released as energy from elastic or plastic deformations occurring within a material. ASTM E1316 (2006) defines acoustic emission (AE) as "the class of phenomena whereby transient elastic waves are generated by the rapid release of energy from localized sources within a material, or the transient elastic waves so generated". Propagation of AE waves can result from various sources including dislocations, micro-cracking, and other changes due to an increase in the strain. The method is very sensitive (within the ultrasonic frequency range) which provides the capability of detecting damage long before it is visible. Other advantages include real-time capability and the location damage regions (Hamstad 1986). AE sensors capture and record the vibration of elastic stress waves as they reach the surface of a material. An AE sensor consists of piezoelectric crystal housed in aluminum or steel casing to protect it from damage. The piezoelectric crystal converts acoustic wave to an electric signal. Because changes in pressure on the surface of the material are usually miniscule the change in voltage is also very small. As a result amplification (internally or using external pre-amplifier) is

necessary. Once amplified the signal is sent it to the data acquisition system. Figure 2.7 shows a schematic for AE monitoring process.

Two common sensors are used in practice: resonant sensors and wide band (also known as broad band) sensors. Resonant sensors are sensitive to only a small range of frequencies thereby filtering out most of the frequency content. The resonant sensor is often chosen to give maximum sensitivity while minimizing unwanted background noise. Broadband sensors have nearly the same sensitivity over a wide range of frequencies thereby allowing for a frequency spectrum analysis. Due to wide range of frequencies captured by the broad band sensor it can be difficult to identify genuine AE from nonrelevant data and it is therefore generally a less sensitive sensor than a properly selected resonant sensor.

The passive ability of AE, external excitation or stimulus is not required for data collection once sensors are placed, makes it a suitable candidate for real-time monitoring and structural health monitoring of in-service structures. Numerous investigations were conducted to AE as a non-destructive evaluation (NDE) method for RC and PC structures, which are the main components of infrastructure such as highway bridges. The main challenge in these studies was wave attenuation and reflections due to the heterogeneous nature of concrete. Different measured AE parameters are presented in this chapter.

2.4 ACOUSTIC EMISSION PARAMETERS

As described earlier, AE waves are generated from a sudden release of energy within a material. The strength of AE signals depends on a number of various factors including the distance and orientation of the source with respect to the sensor as well as

nature of substrate material. The individual detected AE signal is usually referred to as 'hit'. A more in-depth analysis can be performed on individual waveforms of each hit and a number of parameters can be calculated such as amplitude, rise time, duration, signal strength, energy, counts, etc. (ASTM E1316). Figure 2.8 shows an AE waveform schematic with some of the parameters described.

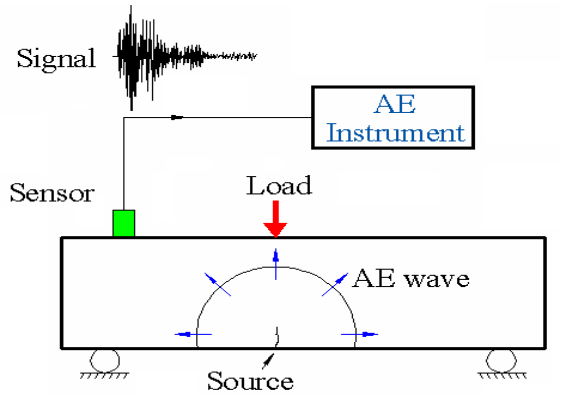

Figure 2.7: AE monitoring process (adopted from ElBatanouny 2012)

Several basic AE parameters are useful in determining when a material is experiencing damage are listed below:

- **Amplitude-** "the peak voltage the largest excursion attained by the signal waveform from and emission event." (ASTM E1316). The amplitude is the highest point on either side of a wave.
- **Duration-** "the time between AE signal start and AE signal end." (ASTM E1316). Measured in microseconds.
- **Energy-** "The energy contained in a detected acoustic emission burst signal, with units usually reported in joules and values which can be expressed in logarithmic form (dB, decibels). (ASTM E1316)
- **Event-** "A local material change giving rise to acoustic emission" (ASTM E1316).

- **Hit-** "The detection and measurement of an AE signal on channel" (ASTM E1316**)**
- **Rise Time-** "the time between AE signal start and the peak amplitude of that AE signal." (ASTM E1316). Measured in microseconds.
- **Frequency-** is the measure of how many cycles per second of pressure variation is present in a particular wave. It should be noted that most waves do not display a single frequency but a complex combination of frequencies that vary over time.
- **Counts-** "the number of times the acoustic emission signal exceeds a preset threshold during any selected portion of a test." (ASTM E1316)
- **Signal Strength-** is defined as the measured area of the rectified AE signal with units proportional to volt seconds (the proportionality constant is specified by the AE instrument manufacturer) (ASTM E1316).

$$S_o = \frac{1}{2}\int_{t_1}^{t_2} f_+(t)dt + \frac{1}{2}\left|\int_{t_1}^{t_2} f_-(t)dt\right|$$

  where: S_o is the signal strength, f_+ is the positive signal envelope function, f_- is the negative signal envelope function, t_1 is the time at first threshold crossing and t_2 is the time at last threshold crossing (Fowler et al. 1989).

- **Source-** "The position of one or more AE events" (CARP, 1999)
- **Threshold-** "a voltage level on a electronic comparator such that signals with amplitudes larger than this level will be recognized. The voltage threshold may be user adjustable, fixed, or automatic floating." (ASTM E1316). The threshold can be used as a data filter that attempts to eliminate unwanted background noise and only recognize genuine emissions.

From the basic AE parameters described above, additional parameters can be calculated that provide additional information:

- **Average Slope of Wave Rise (ASOWR)-**This parameter is a measure of how quickly or slowly an AE signal reaches its peak amplitude.
- **Kaiser and Felicity Effects-** The Kaiser effect is defined as "The absence of detectable acoustic emission at a fixed sensitivity level, until previously applied stress levels are exceeded. (ASTM E1316). The Felicity effect is described as "the presence of detectable acoustic emission at a fixed predetermined sensitivity level at stress levels below those previously applied. (ASTM E1316)
- **Historic Index-** is a parameter used to determine changes of signal strength rate throughout a test. Specifically, it measures changes in slope of the cumulative signal strength vs. time plot.
- **Severity-** The average signal strength of J hits having the maximum numerical value of signal strength.

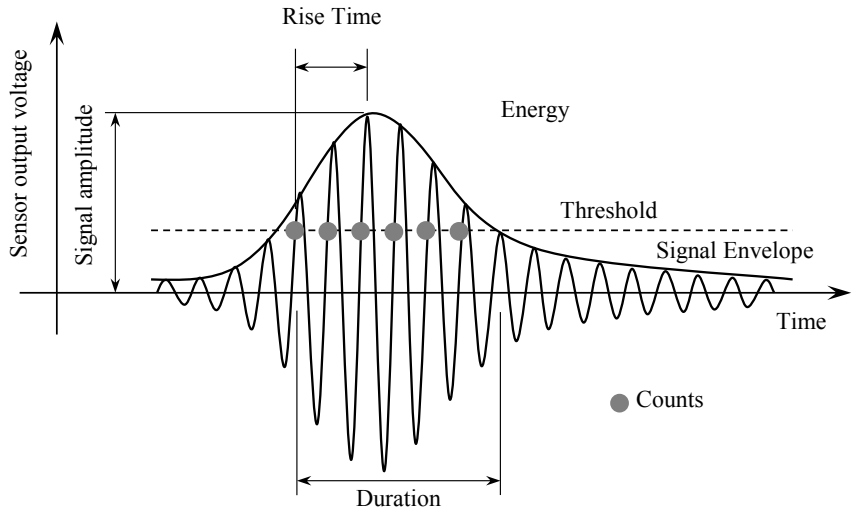

Figure 2.8: Schematic showing some parameters of an AE waveform

CHAPTER 3

PERFORMANCE ASSESSMENT OF IN-SITU PRECAST CONCRETE APPROACH SLAB SYSTEMS[1]

[1] Matthew K. Jones, and Paul H. Ziehl. To be submitted to the SCDOT.

3.1 INTRODUCTION

This report provides an overview of the on-site instrumentation, long-term monitoring, and load testing of precast concrete approach slab systems. The purpose of this research program is to investigate the performance of precast concrete slabs placed on the approaches of a replacement bridge over Big Brown Creek on River Road (S-86) in Union County, S.C.

The approach slabs were fitted with an improved longitudinal shear key detail consisting of lopped interlocking reinforcement bars. The South Carolina Department of Transportation (SCDOT) is considering the use of this structural system in the future for bridge construction. This research program aims to assess the performance of the precast concrete approach slab system and determine the practicality of further implementation as an alternative to current joint designs which historically have been subject to durability problems. Emphasis is placed on the potential changes in long-term behavior of the approach slab systems due to service loadings.

Strain and displacement gages were installed inside the precast approach slabs and on the bridge approach to evaluate the effects of service loads on the bridge approach. The structural behavior of the precast approach slabs is to be monitored while in servicefor a period of 18 months immediately after bridge construction is complete. During that time strain and displacement measurements are to be collected periodically as well as during scheduled dynamic and static loading events with loading trucks. Details regarding the type and location of sensors used for monitoring as well as tasks performed by personnel from the University of South Carolina (U.SC) during instrumentation of the precast approach slab system, data acquisition, and load testing methodology are

presented. Initial readings and readings taken during the first 6 months of service have been collected along with visual inspections conducted during scheduled site visits.

Concrete cylinders were sampled from each batch of concrete used during the casting of the approach slabs as well as the shear key closures adjoining each slab. Concrete cylinders were tested for compressive strength and modulus of elasticity in order to assess the condition of the approach slabs.

3.2 PRECAST APPROACH SLAB SYSTEM

The bridge consists of two approaches at either side of the Big Brown Creek. The south side approach is referred to as the 'Bent One' approach and the north side approach is referred to as the 'Bent Four' approach. Detailed drawings, from Tekna Corporation, showing dimensions of approach slabs and reinforcement schedules are included in the Appendix. Each approach is comprised of four separate precast concrete slabs which are joined with an improved female to female shear key closure joint. The general layout and labeling scheme of the precast slab system on the Bent One approach is shown in Figure 3.1. Each approach has two 'exterior' slabs labeled 'A' and 'D' and two 'interior' slabs labeled 'B' and 'C'. The approach slabs are 12 in. thick and consist of both longitudinal and transverse reinforcing bars located at the top and bottom of the slabs. The shop drawings, from Tekna Corporation, attached in the Appendix refer to slab A as 'Panel 1-2', slabs B and C as 'Panel 1-3' and slab D as 'Panel 1-1'. Interior slabs are identical in size and reinforcing layout and are larger than the exterior slabs. They are situated directly beneath the two traffic lanes with the center shear key joint located directly in the middle of the roadway. The 'exterior' slabs are considerably smaller than the interior slabs and are situated at the edges of the roadway. These slabs make up the shoulder of

the roadway and also support the bridge parapet walls which were formed after approach slabs were set in place. The layout of the Bent Four approach is essentially identical to the Bent One approach but the individual slabs are not labeled because no sensors were placed within the precast slabs on the Bent Four approach.

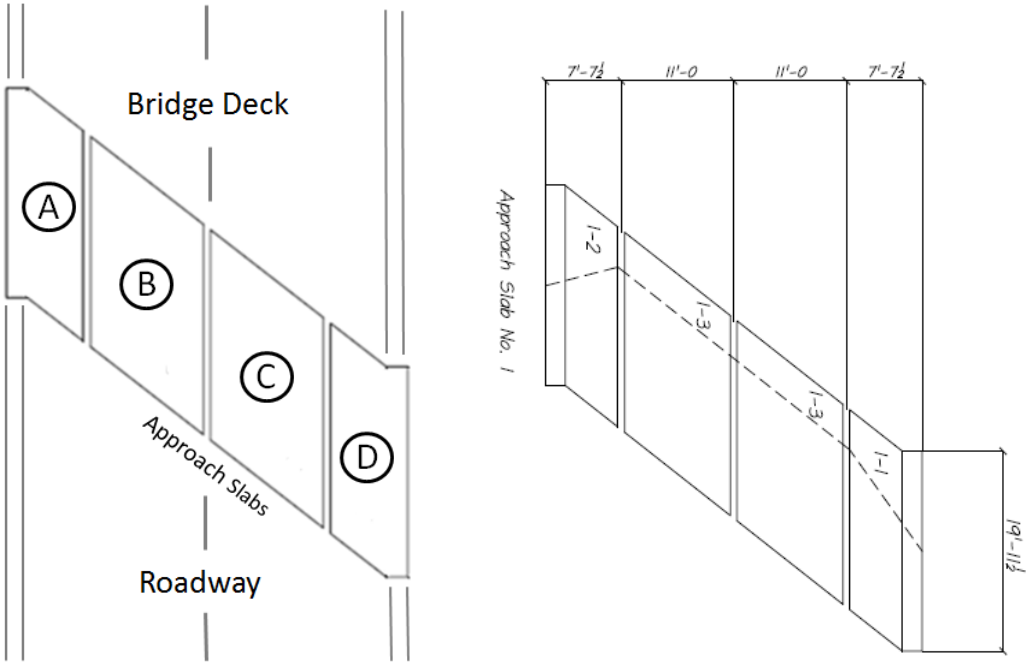

Figure 3.1: Layout of precast approach slab system

The approach slabs rest on a macadam (crushed stone) sub-base material and provide a transition from the paved roadway onto the deck of the bridge superstructure. The sub-base was roller compacted (relative compaction of 100%) to a depth of 6" and is shown in Figure 3.2. Beneath the sub-base a #789 stone (pea-size gravel) was used for back-filling around the wing walls up to the grade of the roadway. A corrugated pipe drain was provided at the base of the wing wall to allow for proper drainage. A 10 mil polyethylene moisture barrier was placed on top of the sub-base just prior to setting of the approach slabs.

The bridge side edge of each approach slab is seated on a ledger formed into the cast-in-place bridge deck. A photograph of the ledger is presented in Figure 3.3. Vertical dowel bars are embedded into the cast-in-place ledger and each approach slab has corresponding vertical sleeves embedded near the bridge side edge of the slab. These sleeves are located such that full alignment with the dowels is achieved. A detailed section view of the bridge approach is shown in Figure 3.4. Alignment of reinforcing dowels can be seen in Figure 3.5 which shows the placement of an interior slab on the bridge approach. Dowel sleeves were filled with grout after the approach slabs were set in place.

Figure 3.2: Compacted crushed stone sub-base material on the Bent One approach

The approach slabs were fitted with an improved connection joint detail consisting of interlocking looped (U-bar) reinforcement bars oriented transversely, relative to the joint, along with a female-to-female shear key as well as two longitudinal reinforcing bars. The purpose of shear keys is to provide resistance to moving traffic loads by facilitating the transfer of shear forces between adjacent slabs. Shear keys allow

the system of discrete panels to react monolithically or as a single piece of concrete under applied loadings. The U bars are spliced with the transverse reinforcement within the precast panel and have a 0.625 in. diameter (#5). The two longitudinal reinforcing bars have a 0.75 in. diameter (#6) , are located in the middle (plan view) of the joint, and are threaded through the inside of the loop bars and tied in at the top and bottom. The loop bars have an even spacing where each panel is completely out of phase with the adjacent panel by a half space. Plan and elevation details of the shear key are shown in Figure 3.6. A photograph of the interlocking of reinforcement bars between adjacent labs is shown in Figure 3.7. The finished shear key connection joint including longitudinal reinforcement is shown in Figure 3.8. The improved connection joint was designed to more effectively transfer and distribute shear and moments between adjacent panels and therefore enhance strength and durability of the approach slab system. After precast slabs were set in place, longitudinal bars were tied to top and bottom loop bars and shear keys were filled with concrete.

Figure 3.3: Cast-in-place bridge deck ledger

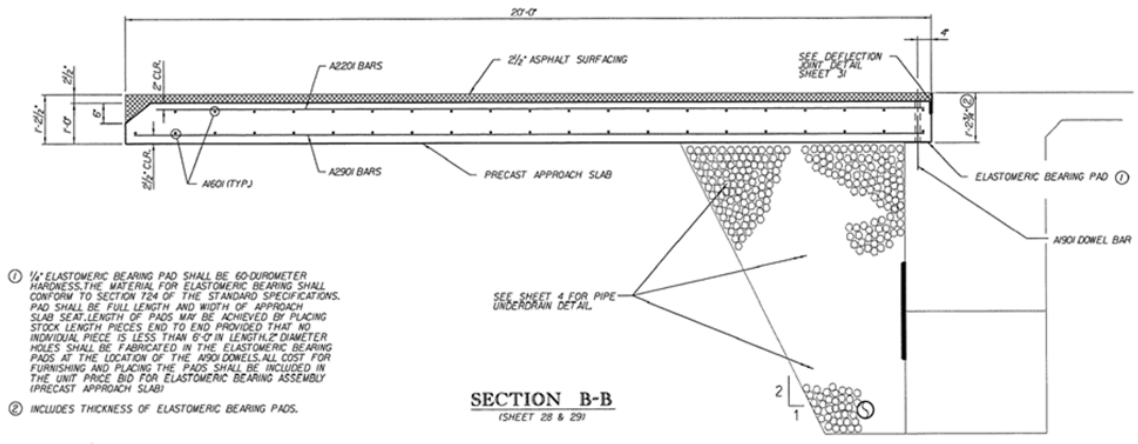

Figure 3.4: Section view of approach slab and bridge deck

Figure 3.5: Interior approach slab being set with vertical dowel alignment

After the approach slabs were set, shear keys filled, and bridge parapets placed each approach was covered with an asphalt pavement. The asphalt surfacing is 2.5 inches thick and extends up to the cast-in-place bridge deck (Figure 3.4). Figure 3.9 shows the bridge after construction was completed.

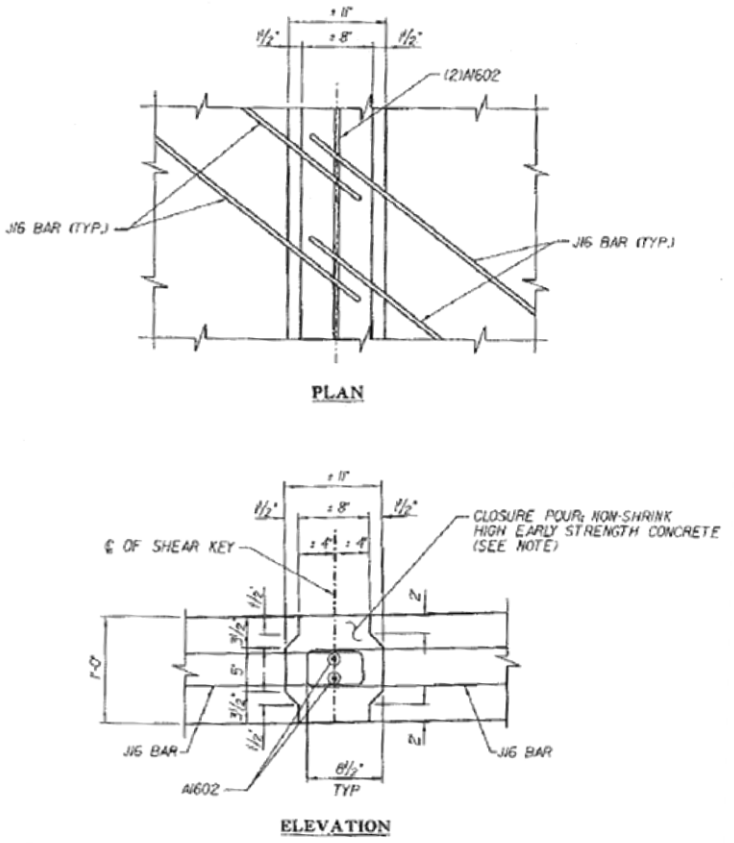

Figure 3.6: Shear key connection detail

Figure 3.7: Interlocking of loop bars after slap placement (typical)

Figure 3.8: Shear key connection joint with longitudinal reinforcing bars tied in

Figure 3.9: The completed replacement bridge over Big Brown Creek

3.3 INSTRUMENTATION

The sensors specified in this report and shown in the included schematics were placed during the fabrication of each individual precast approach slab, during the placement of slabs, and during construction of the bridge approaches. Vibrating Wire Strain Gages (VWSGs), Vibrating Wire Displacement Gages (VWDGs), and Electrical Resistance Strain Gages (ERSGs) were placed on and within the precast approach slabs to observe the strains and displacements due to service level load conditions for a period of 18 months after bridge completion.

3.3.1 Sensor Layout

The two approach slabs are monitored with the following sensors:

(6) Model 4200 Geokon Vibrating Wire Strain Gages (VWSG)

(4) Model 4420 Geokon Vibrating Wire Displacement Gages (VWDG)

(12) Vishay Micro-Measurements Electrical Resistance Strain Gages (ERSG)

3.3.1.1 Bent One Approach

The Bent One approach slab is instrumented with two VWDGs at either side of the approach parallel to the direction of traffic. This approach is also instrumented with 12 ERSGs and 6 VWSGs. A plan view of the Bent One approach slab instrumentation is shown in Figure 3.10 and a cross-section view is shown for clarity in Figure 3.11 An expanded schematic of the details shown in Figure 3.10 is included in the Appendix.

ERSGs were welded onto No. 4 sister bars and placed into the precast slabs during casting. These reinforcing bars, each instrumented with two gages, are constructed with sufficient length such that the bar is fully developed at either end. In exterior slabs a single bar is located closest to the existing reinforcement nearest to the closure pour

connecting the interior slabs. Each interior slab is instrumented with sister bars at either side of the slab. In each of the four slabs sister bars are placed parallel to the direction of traffic at a distance of approximately 4 feet from the bridge side edge of the approach slab. Sister bars are placed and tied in plane with bottom mat reinforcing bars.

A single VWSG is placed in each closure pour perpendicular to the direction of traffic flow. These gages are used to measure concrete strain within the closure pours. Additional VWSGs are located within the precast slabs at the locations shown in Figures 3.10 and 3.11. These gages are situated parallel to the direction of traffic flow at a distance of approximately 4 feet from the bridge side edge of the approach slab. VWSGs are placed and tied in plane with the bottom mat reinforcing bars.

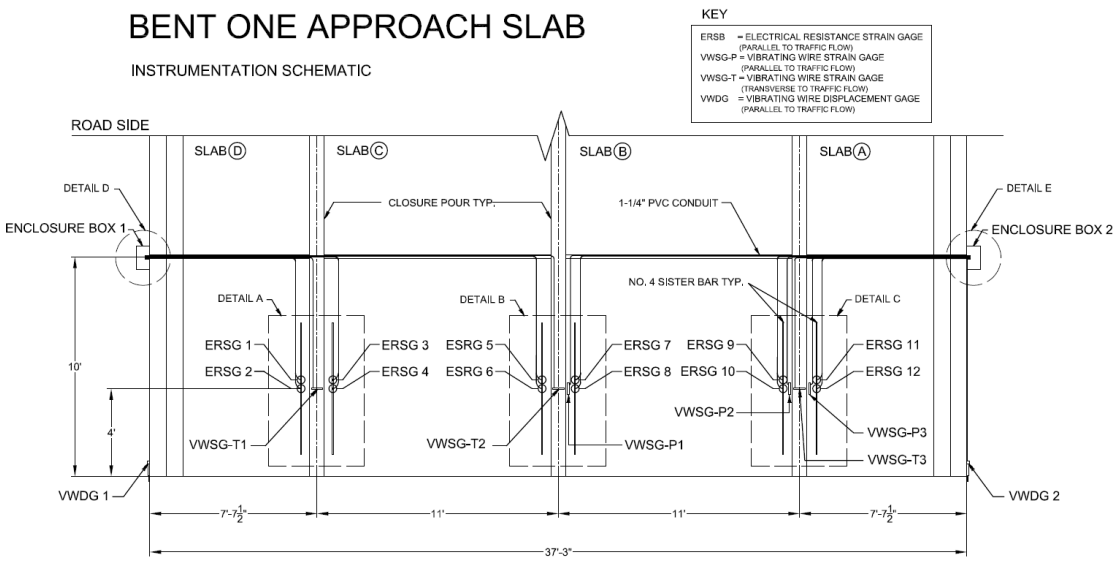

Figure 3.10: Bent One approach slab schematic - plan view

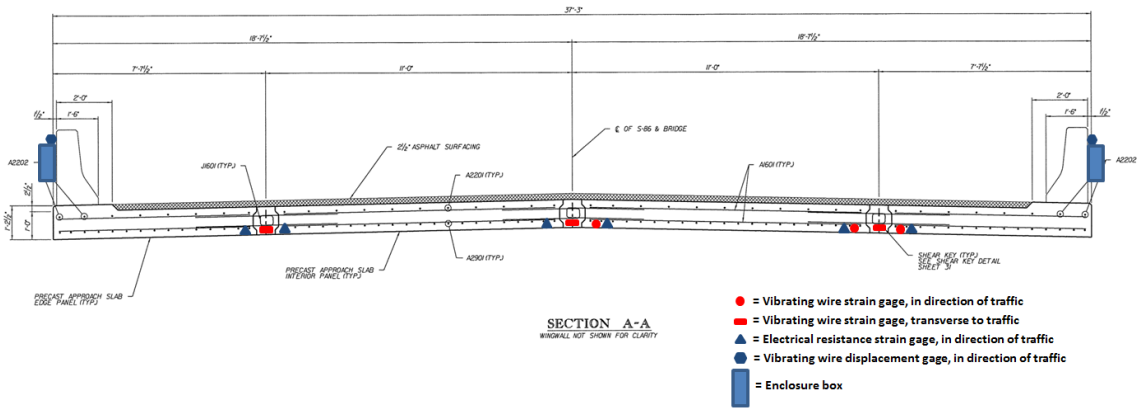

Figure 3.11: Bent One approach slab schematic- cross-section view

3.3.1.2 Bent Four Approach

The Bent Four Approach is instrumented with two VWDGs. These gages are placed in the same manner and location as those placed on the Bent One approach and are shown in Figure 3.12 (plan view) and Figure 3.13 (cross-section view).

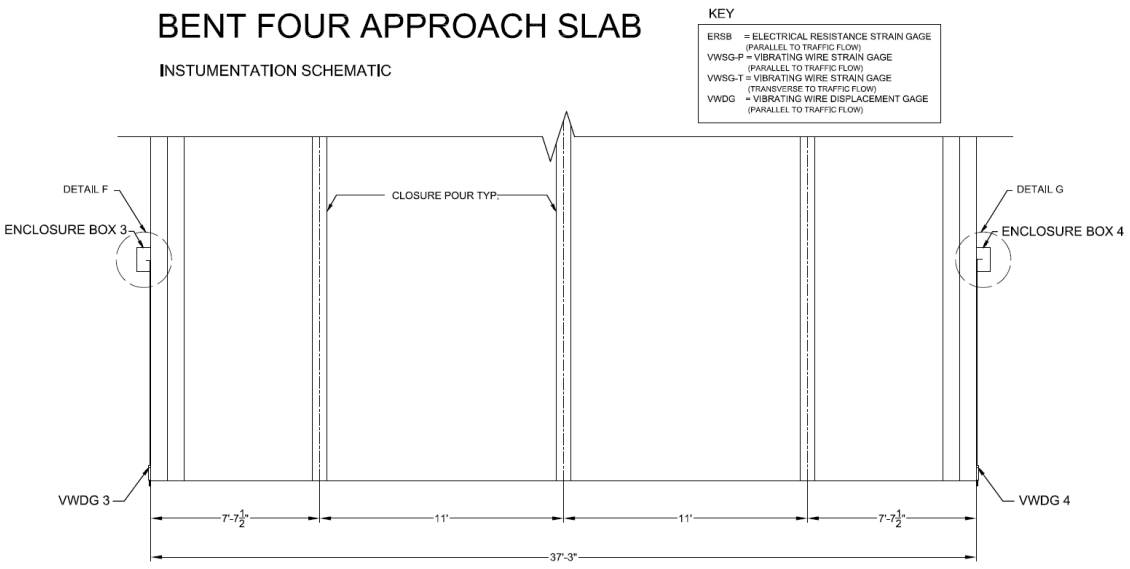

Figure 3.12: Bent Four approach slab schematic – plan view

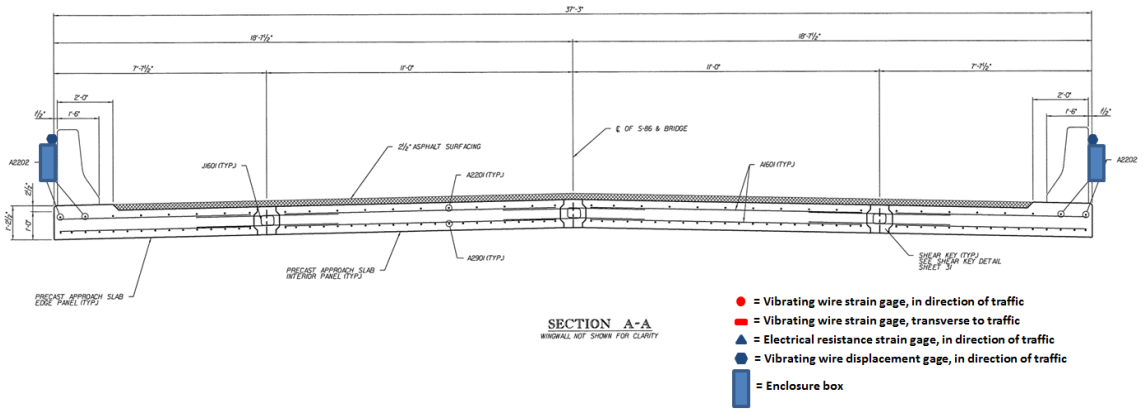

Figure 3.13: Bent Four approach slab schematic – cross section view

3.3.2 Gage Type, Placement, and Protection

All gages located within the precast slabs for the Bent One approach were placed during the casting of each slab. The four slabs are fitted with a 1.5 inch PVC conduit which is used to pass cables through the slabs. This conduit can be seen tied into a reinforcing cage in Figure 3.14. This conduit was sealed at the locations within each slab where sensor cables enter.

Figure 3.14: Conduit for gage cables

Gages not cast into slabs, including the VWDGs and the VWSGs placed in closure pours, were placed during the slab installation process.

Both VWSGs and VWDGs (manufactured by Geokon) are designed to withstand harsh conditions such as being embedded in concrete or full exposure to the environment. Figure 3.15 shows a photograph of both the sensors. The associated cables are also capable of withstanding severe environments. Cable specifications for both VWSGs and VWDGs are shown in Tables 3.1 and 3.2 respectively. The VWSGs have a range of 3,000 μStrain, accuracy of +/- 0.5% of full scale, and 1 μStrain sensitivity. The VWDGs have a range of 100 mm, accuracy of +/- 0.1% of full scale, and sensitivity of 0.025 % of full scale.

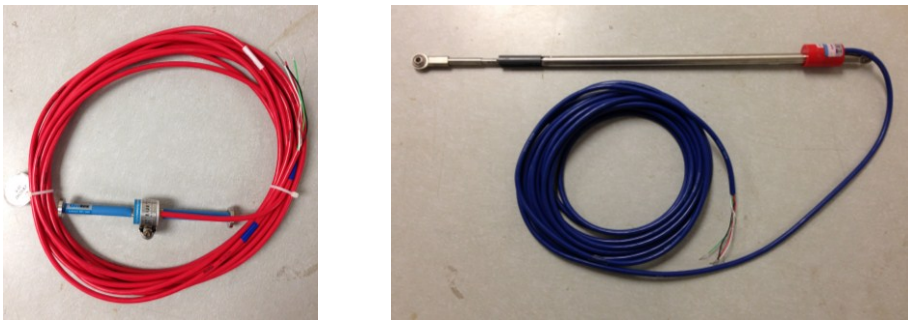

a) b)

Figure 3.15: a) Geokon model 4200 vibrating wire strain gage, b) Geokon model 4420 vibrating wire displacement gage

Table 3.1: VWDG cable specifications

Vibrating Wire Strain Gages - Geokon Model 4200				
Gage#	Orientation	Wire	Length (ft)	Enclosure Box
T1	Transverse	2-250V6	14	1
T2	Transverse	2-250V6	16	1
T3	Transverse	2-250V6	14	2
P1	Parallel	2-250V6	25	2
P2	Parallel	2-250V6	15.5	2
P3	Parallel	2-250V6	13.5	2

Table 3.2: VWDG cable specifications

Vibrating Wire Displacement Gage - Geokon Model 4420			
Gage #	Wire	Length (ft)	Enclosure Box
1	2-250V6	10	1
2	2-250V6	10	2
3	2-250V6	10	3
4	2-250V6	10	4

Each of the Vishay Micro-Measurements CEA-06-W250A-350 model ERSGs was connected to a specially made model 326-DSV copper vinyl shielded cable also provided by Vishay Micro-Measurements. A typical ERSG is shown in Figure 3.16 and ERSG cable specifications are shown in Table 3.3. The 120 Ω and 350 Ω ERSGs both have a sensitivity of +/- 0.4% of full scale and a range of +/- 5000 μStrain.

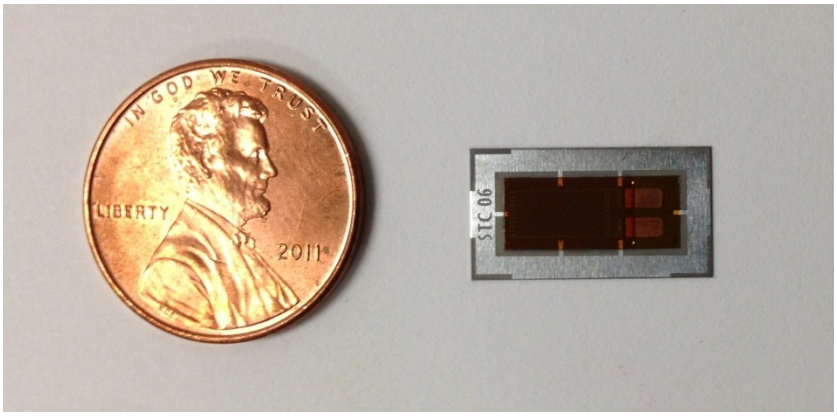

Figure 3.16: Vishay Micro-Measurements model CEA-06-W250A-350 electrical resistance strain gage

Additional protection was provided for each ERSG with a Gagekote No. 5 protective coating (Vishay Micro-Measurements). This coating system is a two part polysulfide material that provides excellent chemical and mechanical resistance including

waterproofing. A No. 4 sister bar with two ERSGs attached, fully waterproofed, and ready for installation is shown in Figure 3.17.

Table 3.3: ERSG cable specifications

Electrical Resistance Strain Gages- Model CEA-06 W250A-120/350					
Bar #	Gage#	Gage Ω	Wire	Length (ft)	Enclosure Box
1	1	350	326- DSV	13.5	1
	2	120	326- DSV	13.5	1
2	3	350	326- DSV	15.5	1
	4	120	326- DSV	15.5	1
3	5	350	326- DSV	25	1
	6	120	326- DSV	25	1
4	7	350	326- DSV	25	2
	8	120	326- DSV	25	2
5	9	350	326- DSV	15.5	2
	10	120	326- DSV	15.5	2
6	11	350	326- DSV	13.5	2
	12	120	326- DSV	13.5	2

Figure 3.17: ERSG attached to No. 4 sister bar, fully waterproofed

Upon exiting each approach, sensor cables are routed directly to waterproof data acquisition enclosure boxes provided by the SCDOT. These enclosures are located on barrier parapets at either side of each instrumented bent. The location of the various gage cables in each enclosure box is shown in the Appendix.

3.3.3 Data Acquisition

Data was acquired continuously during dynamic loading tests and discretely for long term measurements and static loading tests. In addition to data gathered through the instrumentation detailed in this report visual observations were recorded during each site visit. Visual observations include monitoring of cracking as well as other signs of distress. These observations are described in the results section of this report.

Data acquisition systems include Vishay Micro-Measurements P3 strain indicators, a Vishay System 7000 data acquisition system, and a Geokon GK-44 vibrating wire readout system. The GK-404 and P3 systems were used for discrete measurements (Figure 3.18). The GK-404 is used to acquire data from VWSGs and VWDGs and the P3 is used to acquire data from ERSGs. The P3 strain indicator has a 1 μStrain resolution and a +/- 0.1% accuracy.

The System 7000 and Strain Smart software (Figure 3.19) are used to acquire data continuously from ERSGs during dynamic loading. The 7000 System has accuracy of +/- 0.05% of full scale. Because the dynamic loads are applied over a brief period of time the higher data acquisition frequency of the System 7000 is needed for this loading scenario. A data acquisition frequency of 10 Hertz was used during the dynamic load testing.

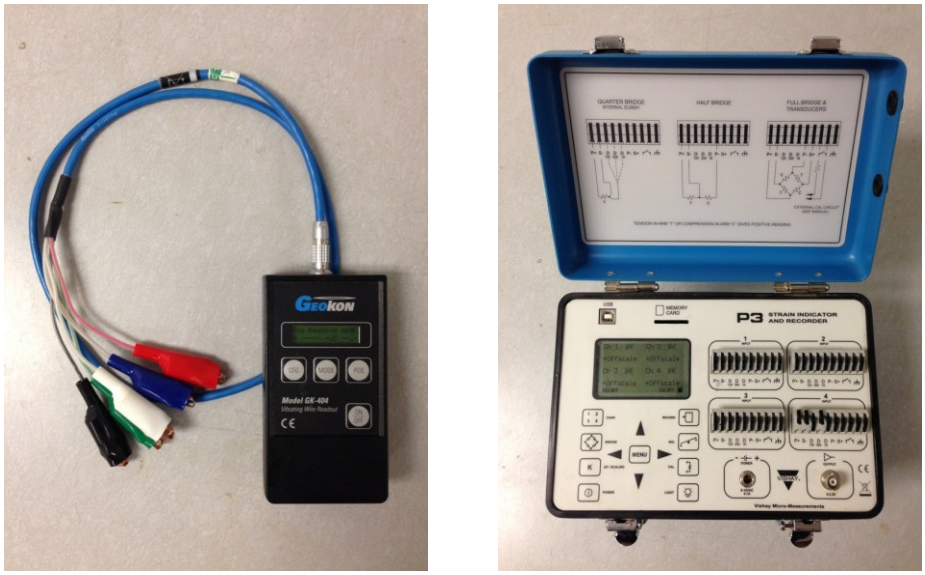

a) b)

Figure 3.18: a) Geokon GK-404 readout system, b) Vishay Micro-Measurements P3 strain indicator

Figure 3.19: Vishay Micro-Measurements System 7000 and Strain Smart data acquisition system

3.3.3.1 Long-term Readings

Initial readings were taken before and just after casting of concrete and are to be recorded every 6 months thereafter for a period of 18 months (Table 3.4). During regularly scheduled site visits at six month intervals data from all sensors is recorded to assess potential changes in the state of the approach slabs. This data set includes initial readings, before and after major events during the slab setting process, and general construction of the bridge approaches.

3.3.3.2 Dynamic and Static Loading Tests

Strain measurements were recorded periodically during dynamic and static loading of the Bent One approach slabs. Continuous readings were recorded for dynamic loading events using the Vishay Micro-Measurements System 7000 and Vishay Micro-Measurements Strain Smart software. Discrete measurements were recorded for the static loading events using the Geokon GK-404 portable readout system. Readings are scheduled to be taken on-site at approximately 6 month intervals to assess changes in behavior due to traffic and environmental conditions. Data up to 6 months after bridge completion has been collected and is presented in the results section of this report.

Table 3.4: Data acquisition schedule

Approach Slab Data Acquisition Schedule						
	Measurement					
Sensor	1	2	3	4	5	6
VWSG	Before Casting	After Casting	After Placement	6 mo. After Placement	12 mo. After Placement	18 mo. After Placement
VWDG	N/A	N/A	After Placement	6 mo. After Placement	12 mo. After Placement	18 mo. After Placement
ERSG	Before Casting	After Casting	After Placement	6 mo. After Placement	12 mo. After Placement	18 mo. After Placement

3.4 INSTRUMENTATION PROGRAM

Instrumentation during the fabrication and casting of the approach slabs occurred over a three day period at the Tekna Corporation precast facility in Charleston, SC. Instrumentation at the bridge site located in Union County, SC occurred over a period of several months during the placement of the approach slabs and during general construction of the bridge and adjoining roadway. A description of the activities performed by personnel from U.SC are presented in this section in a chronological fashion.

3.4.1 Tekna Precast Facility

Activities performed by personnel from U.SC during the instrumentation of approach slabs during casting at the Tekna Precast facility are described in sections 3.4.1.1, 3.4.1.2, and 3.4.1.3.

3.4.1.1 Date of Activity: December 6, 2012

ERSGs and VWSGs were tied into reinforcement cages for both Bent One interior precast approach slabs (Slabs 'B' and 'C'). Figures 3.20 and 3.21 show how gages were tied into bottom reinforcing bars. After gages were installed cables were routed through PVC conduit to the edge of the approach slabs. Initial readings were recorded prior to concrete placement.

Reinforcing cages for the precast approach slabs were incomplete and therefore concrete was not placed on this date.

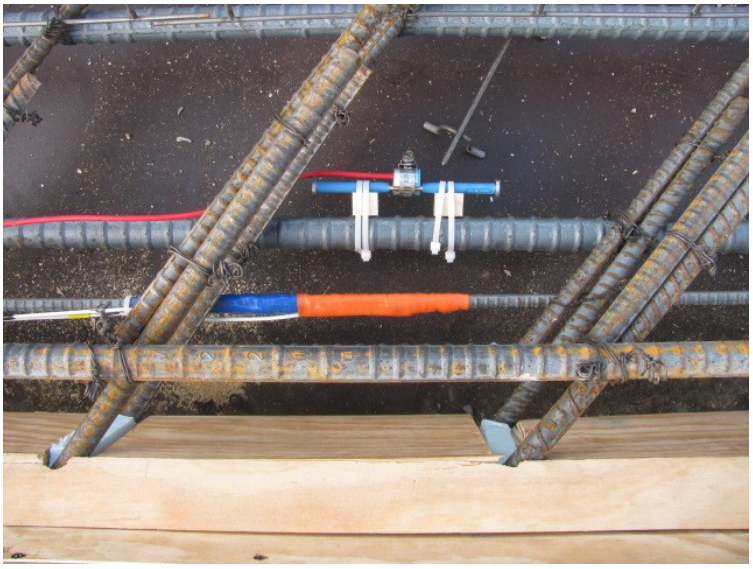

Figure 3.20: ERSG and VWSG placement- top view (typical)

Figure 3.21: ERSG and VWSG placement – side view (typical)

3.4.1.2 Date of Activity: December 7, 2012

ERSGs and VWSGs were tied into reinforcement cages for both Bent One exterior approach slabs (Slabs 'A' and 'D'). Figures 3.20 and 3.21 show how the gages were tied

into the bottom reinforcing bars. After gages were installed cables were routed through PVC conduits to the edge of the approach slabs. Initial readings were recorded prior to placement of the concrete. Readings were also taken just after placement of concrete for both Bent One interior slabs.

Both Bent One interior approach slabs were cast on this date. Concrete placement was monitored closely by U.SC personnel to ensure that strain gages were not damaged or excessively disturbed during casting. Concrete test cylinders were collected and slump tests were performed. For 'Batch 1' concrete used for casting interior slab 'B' a slump of 9.0 inches was measured. For 'Batch 2' concrete used for casting interior slab 'C' a slump of 8.5 inches was measured. Placing of concrete is shown in Figure 3.22. Vertical dowel sleeves can be seen in the lower left corner of the approach slab form.

Figure 3.22: Concrete placement - interior slab 'B'

3.4.1.3 Date of Activity: December 10, 2012

Initial readings from strain gages in both Bent One exterior slabs were recorded prior to placement of concrete. Additional readings from both Bent One interior slabs

were also recorded. Strain readings for both Bent One exterior slabs were recorded just after placement of concrete. After measurements were recorded for all strain gages excess wire was bound and placed inside PVC tubes attached to the edge of each approach slab for protection from weather and damage during shipping.

Both Bent One exterior slabs were cast (Slabs 'A' and 'D'). Concrete placement was again monitored closely by U.SC personnel to ensure the strain gages were not damaged or disturbed during casting. Concrete test cylinders were collected and slump tests performed. A slump of 9.5 inches was measured for 'Batch 3'.

3.4.2 Union County Bridge Site

Activities performed by personnel from U.SC during the instrumentation of approach slabs while on the site of the replacement bridge over Big Brown Creek are described in sections 3.4.2.1, 3.4.2.2, 3.4.2.3, and 3.4.2.4.

3.4.2.1 Date of Activity: January 3, 2013

Measurements were recorded for all Bent One precast approach slabs prior to setting in place on the bridge approach. Figures 3.23 and 3.24 show the slabs during placement. Figure 3.25 shows the approach after all precast slabs have been placed.

Once the precast slabs were placed VWSGs were attached to reinforcing bars for each shear key closure joint (Figures 3.26 and 3.27). Gage cables were then routed through conduit to the outside edges of the bridge. Measurements were recorded for all strain gages just after slab placement. Excess cable was bound and placed inside PVC tubes located near either wing wall to protect against weather and mechanical damage.

Figure 3.23: Placement of interior slab ‘C’

Figure 3.24: Placement of exterior slab ‘D’

Figure 3.25: All approach slabs in place

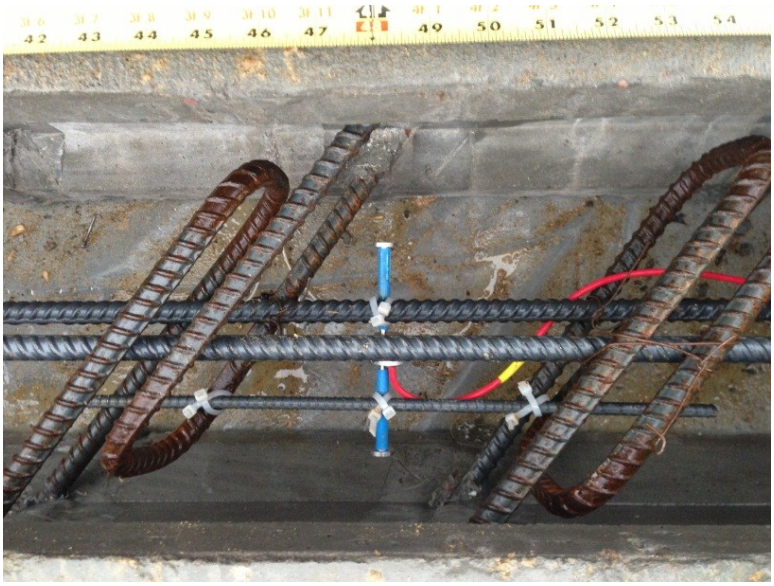

Figure 3.26: VWSG placement in shear key – top view (typical)

Figure 3.27: VWSG placement in shear key – side view (typical)

3.4.2.2 Date of Activity: January 11, 2013

Concrete was placed in all three shear key closures adjoining the approach slabs on this date. A mechanical vibrator was used to ensure concrete was fully consolidated around reinforcement in the closures. Concrete placement and vibration was again monitored closely by personnel from U.SC. Sufficient space was provided between vibrators and strain gages to prevent damage or disturbance of VWSGs. Concrete test cylinders were collected and slump tests performed. A slump of 5.25 inches was measured for 'Batch 4'. Figures 3.28 and 3.29 show concrete being placed in the shear key closures. Figure 3.30 shows the surface of the closure pour being finished with a trowel.

Figure 3.28: Placement of concrete in an instrumented shear key closure

Figure 3.29: Concrete being vibrated during placement

Figure 3.30: Shear key closure being finished

3.4.2.3 Date of Activity: January 23, 2013

Measurements were recorded for all Bent One precast approach slabs before and after concrete placement for the bridge barrier parapets. Figure 3.31 below shows the formed barrier parapet.

Figure 3.31: Barrier parapet

3.4.2.4 Date of Activity: February 14, 2013

All four VWDGs were installed on the outside of parapets on either side of the bridge on the Bent One and Bent Four approaches on this date and initial readings for the VWDGs were recorded. Cables for all gages were routed through conduits to enclosure boxes provided and installed by SCDOT. Cover plates provided by Geokon were also installed to protect the displacement gages from mechanical damage and disturbance. Cover plates are specially designed to be attached to the concrete substrate and to shield the gages without directly contacting the VWDGs or influencing the measurements. Images of the installed VWDGs and cover plates are shown in Figures 3.32 through 3.34.

Figure 3.32: VWDG 3

Figure 3.33: VWDG 1 and Enclosure Box 1

Figure 3.34: Installed cover plate (typical)

3.5 EXPERIMENTAL PROGRAM

3.5.1 Concrete Testing

Concrete cylinders were sampled from each batch of concrete used in casting the approach slabs and for filling shear key closures. These cylinders were used to determine compressive strength and modulus of elasticity of the concrete. A total of 15 cylinders were collected for each batch of concrete to provide three specimens for testing compressive strength at 7, 14, 28, and 56 days and 3 specimens for modulus of elasticity testing at 56 days. The approach slab system required several separate batches of concrete: Batch 1 was used for the casting of approach slab 'B', Batch 2 was used for the casting of approach slab 'C', Batch 3 was used for casting approach slabs 'A' and 'D', and Batch 4 was used for filling shear key closures. Slump tests were also performed on each batch of concrete. Figure 3.35 shows concrete compression testing in progress and the modulus of elasticity test setup.

a) b)

Figure 3.35: a) Concrete compressive strength test, b) Concrete modulus of elasticity test

Concrete compressive strength testing was performed per ASTM C39 / C39M- 12a and modulus of elasticity testing was performed per ASTM C469 / C469MSampling of concrete and slump tests were performed per ASTM C31- 12 and ASTM C143- 12.

3.5.2 Long-term Monitoring

Discrete readings from VWSGs, VWDGs, and ERSGs were recorded on-site in accordance with the data acquisition schedule (Table 3.4) .

Strain and displacement measurements shown in Section 3.6 are relative to the initial readings. For VWSGs and ERSGs the initial reading is considered as the reading taken when instruments were tied securely into reinforcing cages just prior to concrete placement. For VWDGs the initial reading was recorded just after the installation of the gages on the outside of the bridge parapets. Vibrating wire based readings are corrected for effects due to temperature variation and electrical resistance based sensors are corrected for the effect of cable gage length. Photos showing collection of data for VWSGs and ERSGs can be seen in Figures 3.36 and 3.37.

Figure 3.36: VWSG readings being collected with Geokon GK-404 readout system

Figure 3.37: ERSG readings being collected with Vishay P3 strain indicator

3.5.3 Load Testing

A series of load tests is scheduled for the approach slabs positioned on the Bent One approach. These tests are to be conducted during on-site visits at approximately 6, 12, and 18 months (Table 3.4). Dynamic and static forces are applied to the precast approach slabs positioned on the Bent One approach using loading trucks of known weight and dimension made available and operated by personnel from SCDOT. Two load trucks were supplied by SCDOT for the purposes of the first load test occurring approximately 6 months after bridge completion. A photograph of load truck '2' is shown in Figure 3.38.

Figure 3.38: SCDOT load truck (load truck '2')

The axle weights and dimensions for each load truck are shown in Tables 3.5 and 3.6. Each load truck has a total weight of approximately 45,000 lbs and very similar dimensions.

Table 3.5: Load truck weights

Load Truck Specifications		
Truck	Front Axle	Rear Axle
1	10,340	33,580
2	10,620	34,560

Table 3.6: Load truck dimensions

Load Truck Wheel/Axle Dimensions (in)					
Truck	Wheel Base: Front to 1st Rear	Wheel Base: Front to 2nd Rear	Wheel Track	Tread Width-Single Front Tire	Tread Width-Double Rear Tire
1	125	178	95	9	23
2	125	178	95	9	23

3.5.3.1 Dynamic Load Testing

Strain measurements from ERSGs were recorded continuously while the bent one approach slab system was subjected to dynamic loading. A series of low-velocity and high-velocity passes were made by the load trucks on each approach lane. For the low-velocity passes the driver was instructed to travel over each approach lane separately, in the direction of normal traffic flow, at a speed of approximately 5 mph. The drivers were instructed to keep the trucks in the center of the traffic lane during the pass. High velocity passes were made in a similar manner except the speed of travel was increased to 45 mph.

Readings from ERSGs within respective approach slabs were collected from the Vishay Micro-Measurements 7000 system and Strain Smart software throughout the duration of loading. A photo showing the data acquisition setup is shown in Figure 3.39.

Figure 3.39: On-site 7000 System and Strain Smart software data acquisition system setup

ERSGs within approach slabs ‘A’ and ‘B’ on the left side of Bent One were monitored while the load truck traveled in the southbound lane over the approach. These measurements are referred to as ‘Load Case 2’ in the schematic shown in Figure 38. ERSGs within approach slabs ‘C’ and ‘D’ on the right side of Bent One were monitored while the load truck traveled in the north bound lane over the approach. These measurements are referred to as ‘Load Case 1’ in the schematic shown in Figure 3.40. Each approach was loaded and monitored three times as described above for both the low-velocity and high-velocity passes. Figure 3.41 shows a high speed pass on the southbound approach lane in progress during the first load test, conducted 6 months after bridge completion.

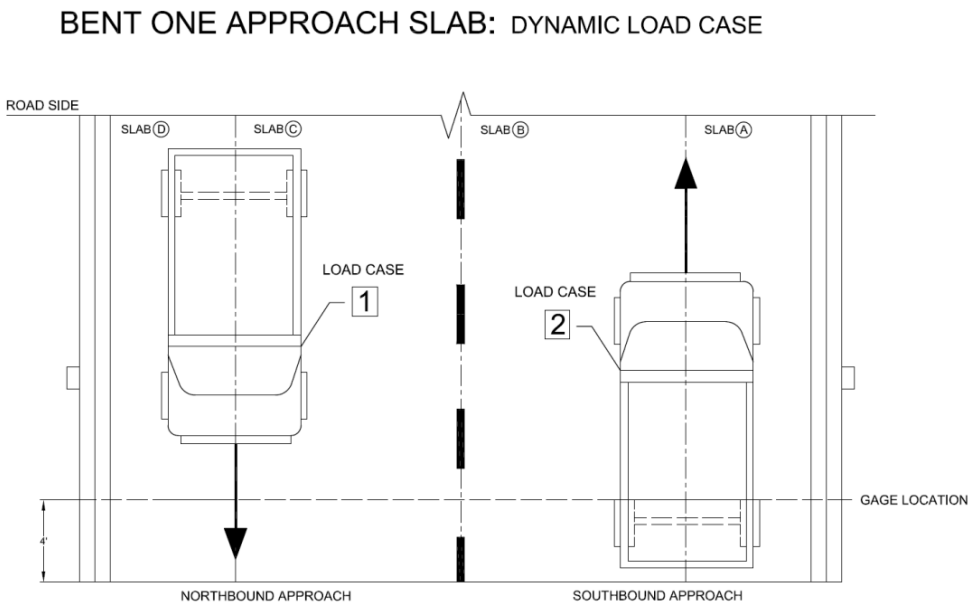

Figure 3.40: Dynamic load case schematic

Figure 3.41: High speed pass on southbound approach lane

3.5.3.2 Static Load Testing

Strain measurements from VWSGs were recorded while Bent One approach slabs were subjected to static loading.

Load trucks were parked with rear axles directly over the strain gages locations for approximately 5 minutes while measurements were recorded manually from the VWSGs. Each approach was loaded and monitored separately. A schematic showing the position of each truck and labeling of the slabs is shown in Figure 3.42. Measurements from the VWSGs within approach slabs 'A' and 'B' and the shear key closures were collected while the load truck was parked in the south bound lane with the rear axle located directly over the gage locations (a distance of 4 feet from bridge side edge of the approach slabs). These measurements are referred to as 'Load Case 4' in the schematic. Measurements from VWSGs within shear key closures were recorded while the load truck was parked in the north bound lane with the rear axles located directly over the gages (a distance of 4 feet from the bridge side edge of the approach slabs). These measurements are referred to

as ‘Load Case 3’ in the schematic. Each approach was loaded three times with initial readings collected prior to each loading. Figures 3.43 and 3.44 show static load testing in progress.

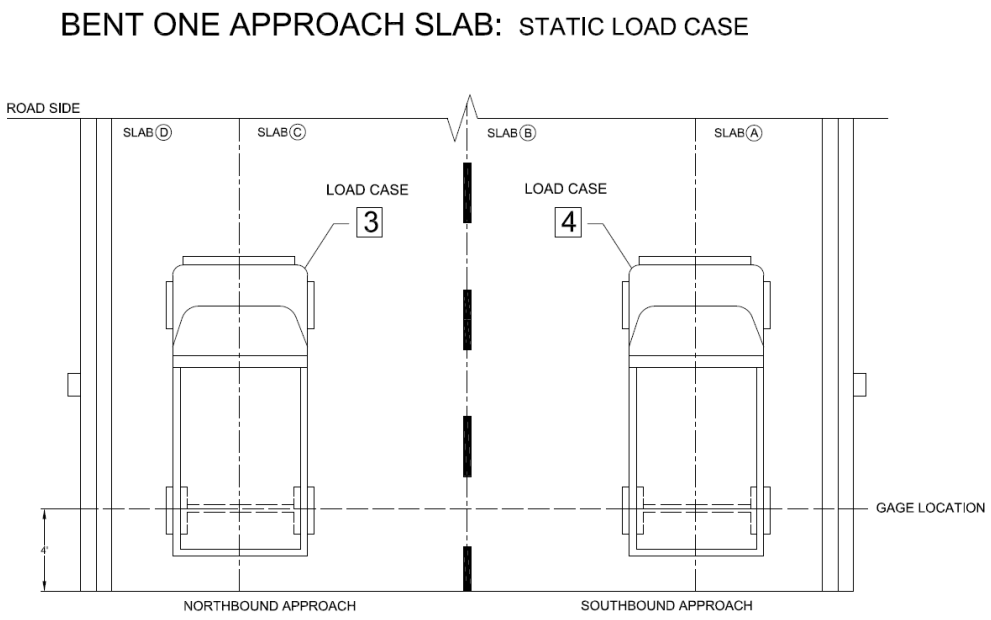

Figure 3.42: Static load case schematic

Figure 3.43: Static load testing: Load Case 3

Figure 3.44: Static load testing: Load Case 4

3.6 RESULTS

3.6.1 Concrete Compressive Strength and Modulus

Compressive strength test results at 7, 14, 28, and 56 days along with modulus of elasticity (E_c) for each the approach slabs are shown in Tables 3.7 through 3.9. Similar results are shown for the shear key closures in Tables 3.10.

Table 3.7: Approach slab 'B' concrete compression test results

Approach Slab 'B'- Batch 1									Slump = 9.0"
Specimen	7-Day		14-Day		28-Day		56-Day		
	P_{ult} (lb)	σ_{ult} (psi)	P_{ult} (lb)	σ_{ult} (psi)	P_{ult} (lb)	σ_{ult} (psi)	P_{ult} (lb)	σ_{ult} (psi)	E_c (10^6 psi)
1	93,810	7,465	103,100	8,508	125,000	9,951	143,400	11,410	5.95
2	92,210	7,338	116,300	9,255	116,900	9,306	126,700	10,080	6.00
3	94,280	7,503	89,850	7,150	122,300	9,732	131,100	10,430	5.05
Average	**93,433**	**7,435**	**103,083**	**8,304**	**121,400**	**9,663**	**133,733**	**10,640**	**5.67**

Table 3.8: Approach slab ‘C’ concrete compression test results

Approach Slab 'C'- Batch 1									Slump = 8.5”
Specimen	7-Day		14-Day		28-Day		56-Day		
	P_{ult} (lb)	σ_{ult} (psi)	P_{ult} (lb)	σ_{ult} (psi)	P_{ult} (lb)	σ_{ult} (psi)	P_{ult} (lb)	σ_{ult} (psi))	E_c (10^6 psi)
1	94,880	7,550	109,300	8,700	126,400	10,060	131,800	10,490	-
2	78,490	6,246	114,900	9,143	106,100	8,440	137,800	10,970	5.70
3	90,680	7,216	101,300	8,059	108,600	8,644	132,000	10,500	5.75
Average	**88,017**	**7,004**	**108,500**	**8,634**	**113,700**	**9,048**	**133,867**	**10,653**	**5.73**

Table 3.9: Approach slab ‘A’ and ‘D’ concrete compression test results

Approach Slab 'A' and ‘D’ - Batch 1									Slump = 9.5”
Specimen	7-Day		14-Day		28-Day		56-Day		
	P_{ult} (lb)	σ_{ult} (psi))	P_{ult} (lb)	σ_{ult} (psi))	P_{ult} (lb)	σ_{ult} (psi))	P_{ult} (lb)	σ_{ult} (psi))	E_c (10^6 psi)
1	78,010	6,208	88,250	7,023	113,000	8,993	113,500	9,033	5.75
2	85,940	6,839	100,400	7,990	99,940	7,953	128,300	10,210	5.95
3	87,010	6,924	100,800	8,022	103,200	8,211	123,100	9,796	5.40
Average	**83,653**	**6,657**	**96,483**	**7,678**	**105,380**	**8,386**	**121,633**	**9,680**	**5.70**

Table 3.10: Shear key closure concrete compression test results

Shear Key Closures – Batch 4									Slump = 5.25”
Specimen	7-Day		14-Day		28-Day		56-Day		
	P_{ult} (lb)	σ_{ult} (psi))	P_{ult} (lb)	σ_{ult} (psi))	P_{ult} (lb)	σ_{ult} (lb/in^2)	P_{ult} (lb)	σ_{ult} (psi))	E_c (10^6 psi)
1	52,560	4,182	62,790	4,997	55,140	4,388	58,900	4,687	3.20
2	53,580	4,264	66,240	5,271	67,750	5,392	69,610	5,540	2.75
3	52,660	4,191	67,070	5,337	59,450	4,731	74,860	5,958	3.60
Average	**52,933**	**4,212**	**65,367**	**5,202**	**60,780**	**4,837**	**67,790**	**5,395**	**3.18**

3.6.2 Long-term Measurements

Long-term strain and displacement measurements are shown in Tables 3.11 through 3.21 and Figures 3.45 through 3.53. Initial readings and readings taken before

and after major events are shown. Vibrating wire based readings shown in Tables and Figures are corrected for effects due to temperature and electrical resistance based readings have been corrected for effects due to cable gage length.

3.6.2.1 Vibrating Wire Strain Gages

Strain measurements collected from VWSGs in approach slabs 'A' and 'B' and within the shear key closures were recorded at different points in time occurring during instrumentation and construction of the bridge approach. These are described in Tables 3.11 through 3.13. Plots corresponding to the data presented in each table are shown in Figures 3.45 through 3.47.

Table 3.11: Vibrating wire strain gage measurements – approach slab 'A'

Measurement	Description	Date	μStrain
VWSG-P3			
1	Initial Reading - 3:00 pm	12/7/2012	0.0
2	After Casting - 4:35 pm	12/7/2012	76.6
3	After Casting - 12:30 pm	12/10/2012	24.1
4	Before Placement/On Truck- 2:05 pm	1/3/2013	-164.4
5	After Placement - 4:50 pm	1/3/2013	-155.4
6	Before Filling Closure - 8:30 am	1/11/2013	-112.4
7	After Filling Closure - 1:00 pm	1/11/2011	-106.3
8	After Barrier Parapet Placed - 12:15 pm	1/23/2013	-204.8
9	After Barrier Parapet Placed - 1:45 pm	1/23/2013	-191.3
10	Before Pavement	2/6/2013	-143.6
11	After Pavement/Bridge Completed	3/27/2013	-136.1
12	3 mo. After Bridge Completed - 11:00 am	6/28/2013	107.1
13	6 mo. After Bridge Completed - 12:30 pm	9/16/2013	49.9

Table 3.12: Vibrating wire strain gage measurements – approach slab 'B'

Measurement	Description	Date	μStrain
VWSG-P1			
1	Initial Reading - 9:40 am	12/7/2012	0.0
2	After Casting - 11:30 pm	12/7/2012	133.2
3	After Casting - 2:50 pm	12/7/2012	137.2
4	After Casting - 12:30 pm	12/10/2012	140.9
5	Before Placement/On Truck - 2:05 pm	1/3/2013	-40.6
6	After Setting in Place - 4:50 pm	1/3/2013	-19.4
7	Before Filling Closures - 8:30 am	1/11/2013	16.8
8	After Filling Closures - 1:00 pm	1/11/2013	22.4
9	After Barrier Parapet Placed - 12:15 pm	1/23/2013	-87.0
10	After Barrier Parapet Placed - 1:45 pm	1/23/2013	-72.3
11	Before Pavement	2/6/2013	-36.7
12	After Pavement/Bridge Completed	3/27/2013	-21.2
13	3 mo. After Bridge Completed - 11:00 am	6/28/2013	207.8
14	6 mo. After Bridge Completed - 12:30 pm	9/16/2013	142.3
VWSG-P2			
1	Initial Reading - 9:40 am	12/7/2012	0.0
2	After Casting - 11:30 pm	12/7/2012	135.0
3	After Casting - 2:50 pm	12/7/2012	151.0
4	After Casting - 12:30 pm	12/10/2012	148.5
5	Before Placement/On Truck - 2:05 pm	1/3/2013	-41.2
6	After Setting in Place - 4:50 pm	1/3/2013	-23.9
7	Before Filling Closures - 8:30 am	1/11/2013	25.6
8	After Filling Closures - 1:00 pm	1/11/2013	32.8
9	After Barrier Parapet Placed - 12:15 pm	1/23/2013	-60.8
10	After Barrier Parapet Placed - 1:45 pm	1/23/2013	-43.3
11	Before Pavement	2/6/2013	-0.1
12	After Pavement/Bridge Completed	3/27/2013	-7.7
13	3 mo. After Bridge Completed - 11:00 am	6/28/2013	218.3
14	6 mo. After Bridge Completed - 12:30 pm	9/16/2013	157.4

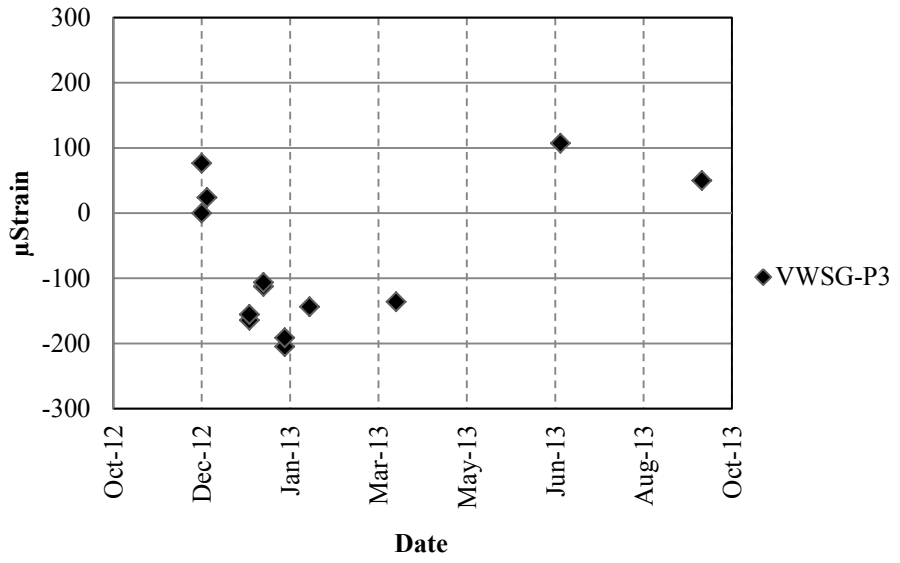

Figure 3.45: Vibrating wire strain gage measurements- approach slab 'A'

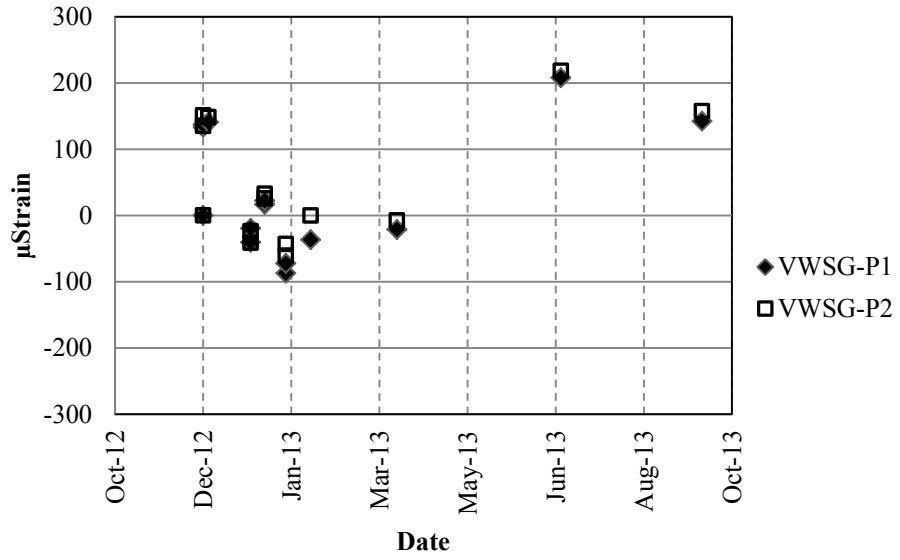

Figure 3.46: Vibrating wire strain gage measurements – approach slab 'B'

Table 3.13: Vibrating wire strain gage measurements – shear key closures

Measurement	Description	Date	μStrain
VWSG-T1			
1	Before Filling Closures - 8:30 am	1/11/2013	0.0
2	After Filling Closures - 1:00 pm	1/11/2013	149.9
4	After Barrier Parapet Placed - 12:15 pm	1/23/2013	-73.9
5	After Barrier Parapet Placed - 1:45 pm	1/23/2013	-55.7
6	Before Pavement	2/6/2013	-13.0
7	After Pavement/Bridge Completed	3/27/2013	56.3
8	3 mo. After Bridge Completed - 11:00 am	6/28/2013	276.0
9	6 mo. After Bridge Completed - 12:30 pm	9/16/2013	195.9
VWSG-T2			
1	Before Filling Closures - 8:30 am	1/11/2013	0.0
2	After Filling Closures - 1:00 pm	1/11/2013	143.8
4	After Barrier Parapet Placed - 12:15 pm	1/23/2013	-91.5
5	After Barrier Parapet Placed - 1:45 pm	1/23/2013	-69.7
6	Before Pavement	2/6/2013	-53.8
7	After Pavement/Bridge Completed	3/27/2013	-11.7
8	3 mo. After Bridge Completed - 11:00 am	6/28/2013	187.8
9	6 mo. After Bridge Completed - 12:30 pm	9/16/2013	92.1
VWSG-T3			
1	Before Filling Closures - 8:30 am	1/11/2013	0.0
2	After Filling Closures - 1:00 pm	1/11/2013	157.2
4	After Barrier Parapet Placed - 12:15 pm	1/23/2013	-105.5
5	After Barrier Parapet Placed - 1:45 pm	1/23/2013	-97.4
6	Before Pavement	2/6/2013	-39.6
7	After Pavement/Bridge Completed	3/27/2013	16.9
8	3 mo. After Bridge Completed - 11:00 am	6/28/2013	247.0
9	6 mo. After Bridge Completed - 12:30 pm	9/16/2013	173.6

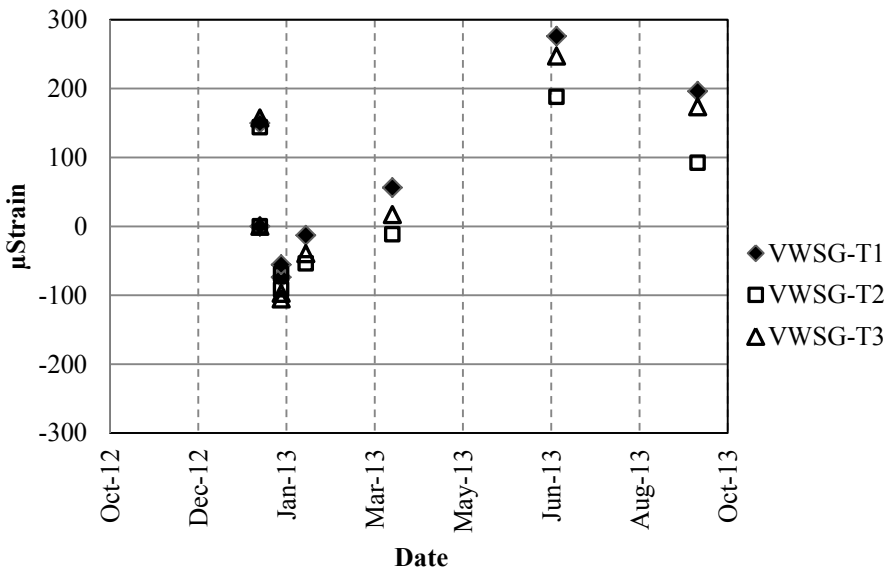

Figure 3.47: Vibrating wire strain gage measurements – shear key closures

3.6.2.2 Electrical Resistance Strain Gages

Strain measurements were recorded from the ERSGs in approach slabs 'A', 'B', 'C', and 'D' as shown below. Measurements were recorded at different points in time occurring during instrumentation and construction of the bridge approach as described in Tables 3.14 through 3.19. Plots showing discrete strain readings corresponding to the data presented in each table are shown in Figures 3.48 through 3.51. In some instances when taking strain readings, anomalies associated with ERSGs and data acquisition systems were encountered and as a result readings from some gages were unable to be collected. Readings marked 'N/A' in the tables presented below are associated with these occurrences.

Table 3.14: Electrical resistance strain gage measurements – approach slab 'A'

Measurement	Description	Date	μStrain
ERSG 11			
1	Initial Reading - 3:17 pm	12/7/2012	0
2	After Casting - 4:35 pm	12/7/2012	1666
3	After Casting - 12:30 pm	12/10/2012	1553
4	Before Placement/On truck - 2:15 pm	1/3/2013	1427
5	After Setting in Place - 5:00 pm	1/3/2013	1525
6	Before Filling Closures - 9:00 am	1/11/2013	1463
7	After Filling Closures - 1:00 pm	1/11/2013	1435
8	After Barrier Parapet Placed - 12:30 pm	1/24/2013	-100
9	After Barrier Parapet Placed - 1:45 pm	1/24/2013	-4433
10	Before Pavement	2/6/2013	1464
11	After Pavement/Bridge Completed	3/27/2013	1554
12	3 mo. After Bridge Completed - 11:00 am	6/28/2013	1610
13	6 mo. After Bridge Completed - 12:30 pm	9/16/2013	1651
ERSG 12			
1	Initial Reading - 3:17 pm	12/7/2012	0
2	After Casting - 4:35 pm	12/7/2012	-257
3	After Casting - 12:30 pm	12/10/2012	-3882
4	Before Placement/On truck - 2:15 pm	1/3/2013	-184
5	After Setting in Place - 5:00 pm	1/3/2013	-481
6	Before Filling Closures - 9:00 am	1/11/2013	-837
7	After Filling Closures - 1:00 pm	1/11/2013	-378
8	After Barrier Parapet Placed - 12:30 pm	1/24/2013	-4670
9	After Barrier Parapet Placed - 1:45 pm	1/24/2013	-1648
10	Before Pavement	2/6/2013	-312
11	After Pavement/Bridge Completed	3/27/2013	-323
12	3 mo. After Bridge Completed - 11:00 am	6/28/2013	30
13	6 mo. After Bridge Completed - 12:30 pm	9/16/2013	358

Table 3.15: Electrical resistance strain gage measurements – approach slab 'B'

Measurement	Description	Date	μStrain
ERSG 7			
1	Initial Reading - 3:17 pm	12/7/2012	0
2	After Casting - 4:35 pm	12/7/2012	N/A
3	After Casting - 12:30 pm	12/10/2012	1221
4	Before Placement/On truck - 2:15 pm	1/3/2013	1422
5	After Setting in Place - 5:00 pm	1/3/2013	1381
6	Before Filling Closures - 9:00 am	1/11/2013	1360
7	After Filling Closures - 1:00 pm	1/11/2013	-61
8	After Barrier Parapet Placed - 12:30 pm	1/24/2013	1430
9	After Barrier Parapet Placed - 1:45 pm	1/24/2013	1462
10	Before Pavement	2/6/2013	1462
11	After Pavement/Bridge Completed	3/27/2013	1403
12	3 mo. After Bridge Completed - 11:00 am	6/28/2013	1414
13	6 mo. After Bridge Completed - 12:30 pm	9/16/2013	-117
ERSG 8			
1	Initial Reading - 3:17 pm	12/7/2012	N/A
2	After Casting - 4:35 pm	12/7/2012	N/A
3	After Casting - 12:30 pm	12/10/2012	N/A
4	Before Placement/On truck - 2:15 pm	1/3/2013	N/A
5	After Setting in Place - 5:00 pm	1/3/2013	N/A
6	Before Filling Closures - 9:00 am	1/11/2013	N/A
7	After Filling Closures - 1:00 pm	1/11/2013	N/A
8	After Barrier Parapet Placed- 12:30 pm	1/24/2013	N/A
9	After Barrier Parapet Placed - 1:45 pm	1/24/2013	N/A
10	Before Pavement	2/6/2013	N/A
11	After Pavement/Bridge Completed	3/27/2013	N/A
12	3 mo. After Bridge Completed - 11:00 am	6/28/2013	N/A
13	6 mo. After Bridge Completed - 12:30 pm	9/16/2013	N/A

Table 3.16: Electrical resistance strain gage measurements – approach slab 'B'

Measurement	Description	Date	μStrain
ERSG 9			
1	Initial Reading - 3:17 pm	12/7/2012	0
2	After Casting - 4:35 pm	12/7/2012	6036
3	After Casting - 12:30 pm	12/10/2012	2340
4	Before Placement/On truck - 2:15 pm	1/3/2013	2230
5	After Setting in Place - 5:00 pm	1/3/2013	2230
6	Before Filling Closures - 9:00 am	1/11/2013	2192
7	After Filling Closures - 1:00 pm	1/11/2013	3439
8	After Barrier Parapet Placed - 12:30 pm	1/24/2013	-3263
9	After Barrier Parapet Placed - 1:45 pm	1/24/2013	-3242
10	Before Pavement	2/6/2013	3272
11	After Pavement/Bridge Completed	3/27/2013	3500
12	3 mo. After Bridge Completed - 11:00 am	6/28/2013	2469
13	6 mo. After Bridge Completed - 12:30 pm	9/16/2013	N/A
ERSG 10			
1	Initial Reading - 3:17 pm	12/7/2012	0
2	After Casting - 4:35 pm	12/7/2012	N/A
3	After Casting - 12:30 pm	12/10/2012	1060
4	Before Placement/On truck - 2:15 pm	1/3/2013	N/A
5	After Setting in Place - 5:00 pm	1/3/2013	N/A
6	Before Filling Closures - 9:00 am	1/11/2013	N/A
7	After Filling Closures - 1:00 pm	1/11/2013	N/A
8	After Barrier Parapet Placed - 12:30 pm	1/24/2013	N/A
9	After Barrier Parapet Placed - 1:45 pm	1/24/2013	N/A
10	Before Pavement	2/6/2013	N/A
11	After Pavement/Bridge Completed	3/27/2013	976
12	3 mo. After Bridge Completed - 11:00 am	6/28/2013	1010
13	6 mo. After Bridge Completed - 12:30 pm	9/16/2013	1032

Table 3.17: Electrical resistance strain gage measurements - approach 'C'

Measurement	Description	Date	μStrain
ERSG 3			
1	Initial Reading - 3:17 pm	12/7/2012	0
2	After Casting - 4:10 pm	12/7/2012	4419
3	After Casting - 12:30 pm	12/10/2012	4239
4	Before Placement/On truck - 1:35 pm	1/3/2013	4270
5	After Setting in Place - 5:00 pm	1/3/2013	4340
6	Before Filling Closures - 9:00 am	1/11/2013	4225
7	After Filling Closures - 1:00 pm	1/11/2013	3770
8	After Barrier Parapet Placed - 12:30 pm	1/24/2013	-4195
9	After Barrier Parapet Placed - 1:45 pm	1/24/2013	1948
10	Before Pavement	2/6/2013	4334
11	After Pavement/Bridge Completed	3/27/2013	4218
12	3 mo. After Bridge Completed - 11:00 am	6/28/2013	4179
13	6 mo. After Bridge Completed - 12:30 pm	9/16/2013	1689
ERSG 4			
1	Initial Reading - 3:17 pm	12/7/2012	0
2	After Casting - 4:10 pm	12/7/2012	-630
3	After Casting - 12:30 pm	12/10/2012	350
4	Before Placement/On truck - 1:35 pm	1/3/2013	131
5	After Setting in Place - 5:00 pm	1/3/2013	170
6	Before Filling Closures - 9:00 am	1/11/2013	-379
7	After Filling Closures - 1:00 pm	1/11/2013	-369
8	After Barrier Parapet Placed - 12:30 pm	1/24/2013	459
9	After Barrier Parapet Placed - 1:45 pm	1/24/2013	863
10	Before Pavement	2/6/2013	190
11	After Pavement/Bridge Completed	3/27/2013	217
12	3 mo. After Bridge Completed - 11:00 am	6/28/2013	-235
13	6 mo. After Bridge Completed - 12:30 pm	9/16/2013	1320

Table 3.18: Electrical resistance strain gage measurements – approach slab 'C'

Measurement	Description	Date	μStrain
ERSG 5			
1	Initial Reading - 3:17 pm	12/7/2012	0
2	After Casting - 4:10 pm	12/7/2012	3613
3	After Casting - 12:30 pm	12/10/2012	3500
4	Before Placement/On truck - 1:35 pm	1/3/2013	3583
5	After Setting in Place - 5:00 pm	1/3/2013	3560
6	Before Filling Closures - 9:00 am	1/11/2013	3568
7	After Filling Closures - 1:00 pm	1/11/2013	3529
8	After Barrier Parapet Placed - 12:30 pm	1/24/2013	-3667
9	After Barrier Parapet Placed - 1:45 pm	1/24/2013	3608
10	Before Pavement	2/6/2013	3570
11	After Pavement/Bridge Completed	3/27/2013	3589
12	3 mo. After Bridge Completed - 11:00 am	6/28/2013	3484
13	6 mo. After Bridge Completed - 12:30 pm	9/16/2013	1337
ERSG 6			
1	Initial Reading - 3:17 pm	12/7/2012	0
2	After Casting - 4:10 pm	12/7/2012	-11308
3	After Casting - 12:30 pm	12/10/2012	2739
4	Before Placement/On truck - 1:35 pm	1/3/2013	1074
5	After Setting in Place - 5:00 pm	1/3/2013	1222
6	Before Filling Closures - 9:00 am	1/11/2013	1089
7	After Filling Closures - 1:00 pm	1/11/2013	627
8	After Barrier Parapet Placed - 12:30 pm	1/24/2013	-1066
9	After Barrier Parapet Placed - 1:45 pm	1/24/2013	-5369
10	Before Pavement	2/6/2013	1113
11	After Pavement/Bridge Completed	3/27/2013	1412
12	3 mo. After Bridge Completed - 11:00 am	6/28/2013	1482
13	6 mo. After Bridge Completed - 12:30 pm	9/16/2013	1579

Table 3.19: Electrical resistance strain gage measurements – approach slab 'D'

Measurement	Description	Date	μStrain
ERSG 1			
1	Initial Reading - 3:17 pm	12/7/2012	0
2	After Casting - N/A	12/7/2012	N/A
3	After Casting - 12:30 pm	12/10/2012	9
4	Before Placement/On truck - 1:35 pm	1/3/2013	23
5	After Setting in Place - 5:00 pm	1/3/2013	26
6	Before Filling Closures - 9:00 am	1/11/2013	-5936
7	After Filling Closures - 1:00 pm	1/11/2013	-11435
8	After Barrier Parapet Placed - 12:30 pm	1/24/2013	-1870
9	After Barrier Parapet Placed - 1:45 pm	1/24/2013	-3819
10	Before Pavement	2/6/2013	10
11	After Pavement/Bridge Completed	3/27/2013	6
12	3 mo. After Bridge Completed - 11:00 am	6/28/2013	-6806
13	6 mo. After Bridge Completed - 12:30 pm	9/16/2013	-2207
ERSG 2			
1	Initial Reading - 3:17 pm	12/7/2012	0
2	After Casting - 4:10 pm	12/7/2012	N/A
3	After Casting - 12:30 pm	12/10/2012	36
4	Before Placement/On truck - 1:35 pm	1/3/2013	15
5	After Setting in Place - 5:00 pm	1/3/2013	15
6	Before Filling Closures - 9:00 am	1/11/2013	137
7	After Filling Closures - 1:00 pm	1/11/2013	110
8	After Barrier Parapet Placed - 12:30 pm	1/24/2013	-4569
9	After Barrier Parapet Placed - 1:45 pm	1/24/2013	-1213
10	Before Pavement	2/6/2013	103
11	After Pavement/Bridge Completed	3/27/2013	51
12	3 mo. After Bridge Completed - 11:00 am	6/28/2013	144
13	6 mo. After Bridge Completed - 12:30 pm	9/16/2013	-1303

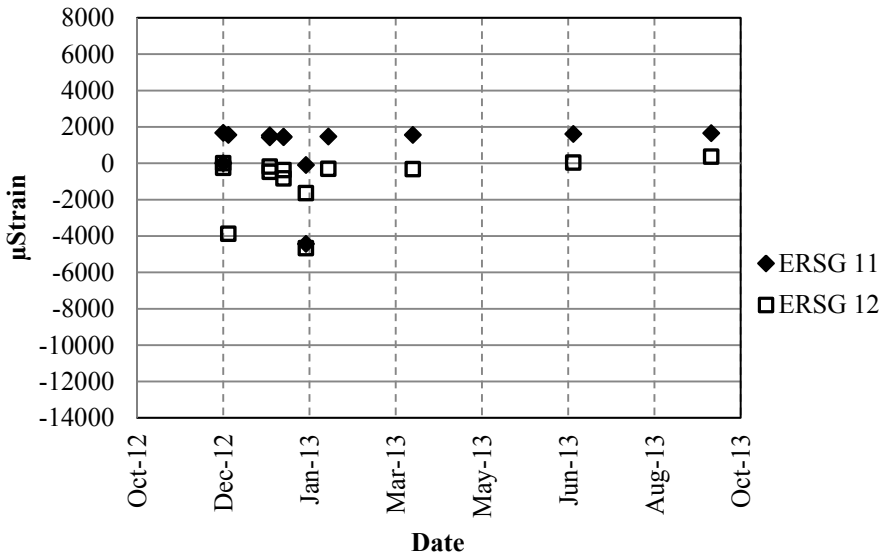

Figure 3.48: Electrical resistance strain gage measurements – approach slab 'A'

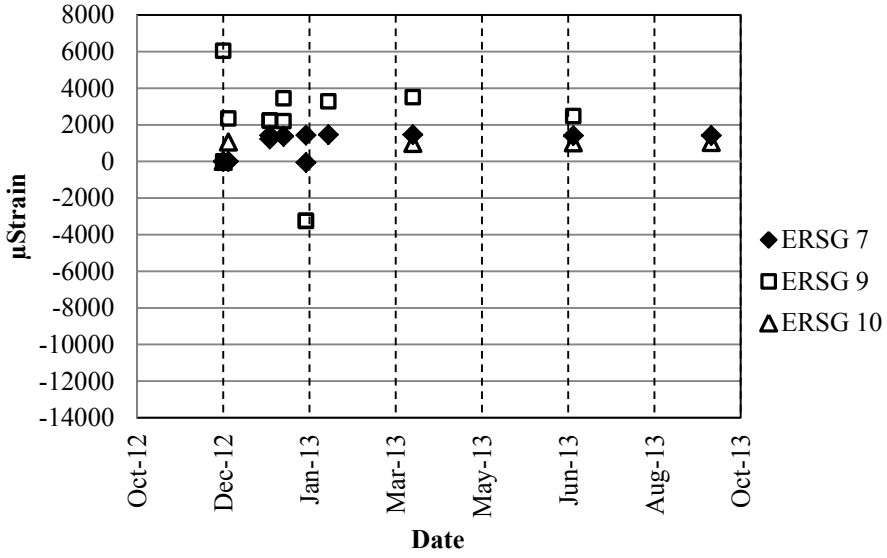

Figure 3.49: Electrical resistance strain gage measurements – approach slab 'B'

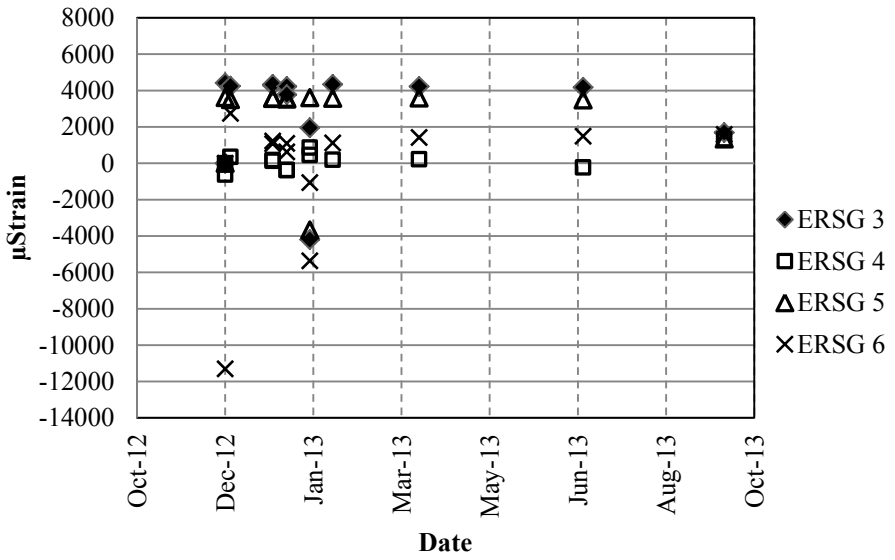

Figure 3.50: Electrical resistance strain gage measurements – approach slab 'C'

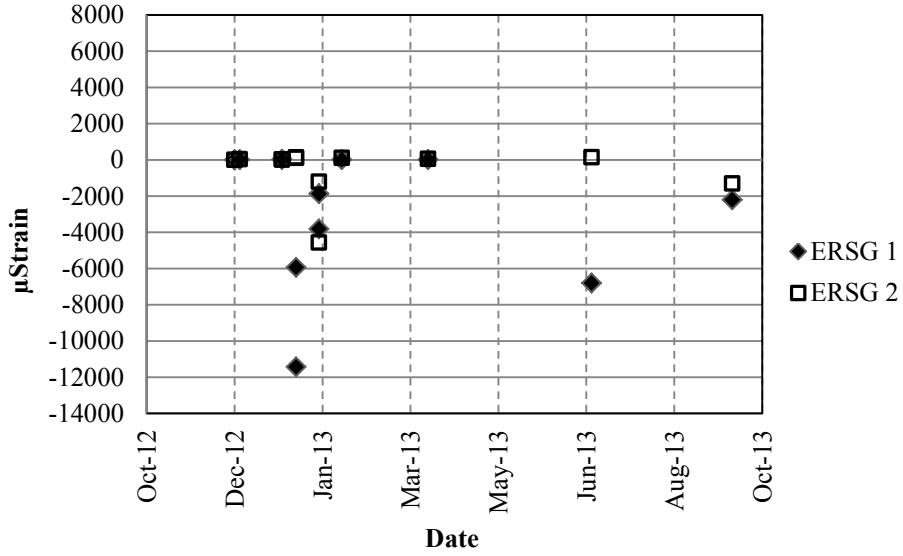

Figure 3.51: Electrical resistance strain gage measurements – approach slab 'D'

3.6.2.3 Vibrating Wire Displacement Gages

Displacement readings from VWDGs located on either side of the Bent One and Bent Four approaches are shown in Tables 3.20 and 3.21 and Figures 3.52 and 3.53.

Table 3.20: Vibrating wire displacement gage measurements – Bent One

Measurement	Description	Date	Displacement (mm)
VWDG 1			
1	Initial Reading - 4:00 pm	2/14/2013	0.00
2	Bridge Completed - Before Cover Plate	3/27/2013	1.19
3	Bridge Completed - After Cover Plate	3/27/2013	0.72
4	3 mo. After Bridge Completed - 11:00 am	6/28/2013	-1.50
5	6 mo. After Bridge Completed - 12:30 pm	9/16/2013	-0.68
VWDG 2			
1	Initial Reading- 4:00 pm	2/14/2013	0.00
2	Bridge Completed- Before Cover Plate	3/27/2013	1.57
3	Bridge Completed- After Cover Plate	3/27/2013	1.08
4	3 mo. After Bridge Completed - 11:00 am	6/28/2013	-0.38
5	6 mo. After Bridge Completed - 12:30 pm	9/16/2013	1.02

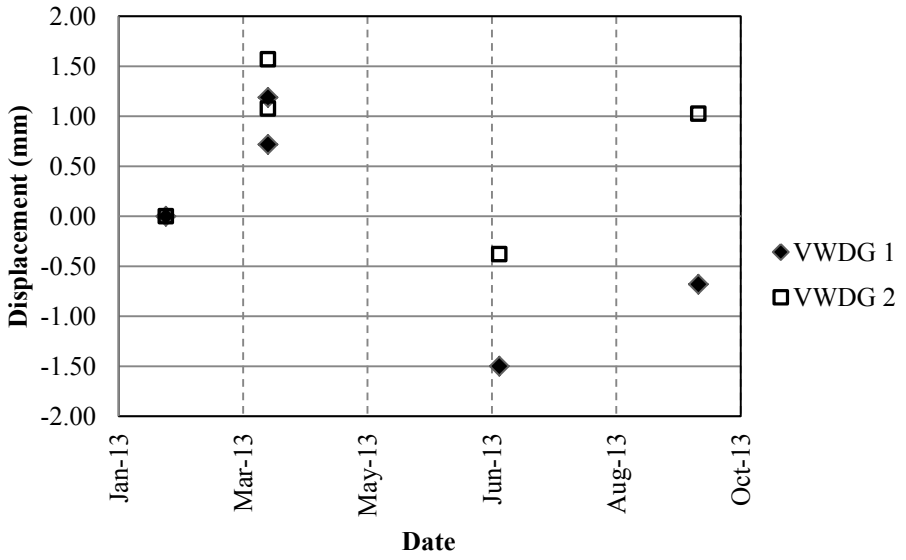

Figure 3.52: Vibrating wire displacement gage measurements – Bent One

Table 3.21: Vibrating wire displacement gage measurements – Bent Four

Measurement	Description	Date	Displacement (mm)
VWDG 3			
1	Initial Reading - 4:00 pm	2/14/2013	0.00
2	Bridge Completed - Before Cover Plate	3/27/2013	0.70
3	Bridge Completed - After Cover Plate	3/27/2013	0.53
4	3 mo. After Bridge Completed - 11:00 am	6/28/2013	-0.04
5	6 mo. After Bridge Completed - 12:30 pm	9/16/2013	-0.11
VWDG 4			
1	Initial Reading - 4:00 pm	2/14/2013	0.00
2	Bridge Completed - Before Cover Plate	3/27/2013	1.41
3	Bridge Completed - After Cover Plate	3/27/2013	1.36
4	3 mo. After Bridge Completed - 11:00 am	6/28/2013	-0.92
5	6 mo. After Bridge Completed - 12:30 pm	9/16/2013	0.17

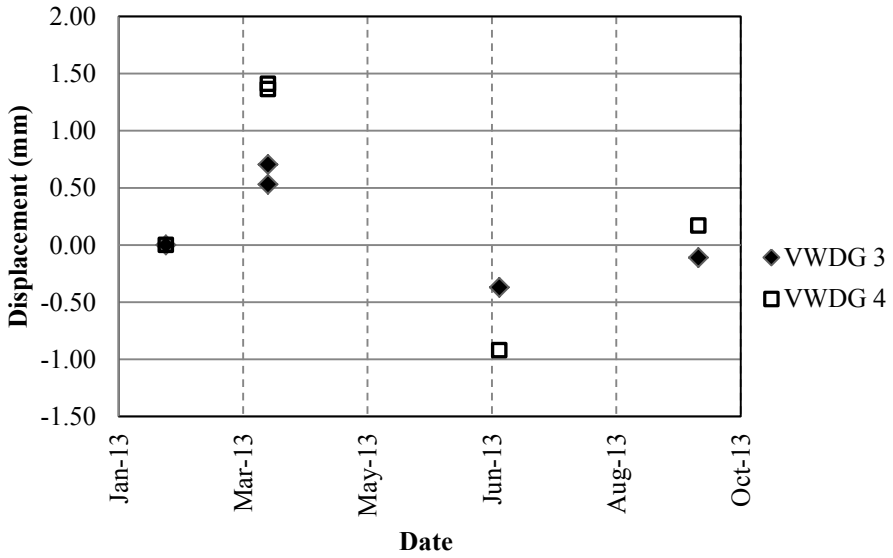

Figure 3.53: Vibrating wire displacement gage measurements – Bent Four

3.6.3 Load Testing Results

Results from the dynamic and static load tests performed on September, 16 2013 are presented in the tables and figures below. ERSGs are corrected for gage length and VWSG readings are corrected for temperature effects.

3.6.3.1 Dynamic Loading

Plots showing the change in strain with respect to time during dynamic loading of the Bent One approach slabs are presented below. Figure 3.54 shows results for the Load Case 1 passes at 5 mph and Figure 3.55 shows the results for the same load case passes at 45 mph. Figure 3.56 shows test results for the Load Case 2 passes at 5 mph and Figure 3.57 shows test results for the same load case passes at 45 mph.

3.6.3.2 Static loading

The results from static loading on the bent one approach slabs are presented below. The tables and figures show the change in strain (ΔμStrain) occurring while the the Bent One approach slab system was subjected to static loading. Initial readings were recorded during live load free conditions and then readings were taken while the load truck was parked on the approach. Load Case 3 test results are shown in Table 3.22 and Figure 3.59. Load Case 4 test results are shown in Table 3.23 and Figure 3.59. Strain readings have been corrected for temperature effects.

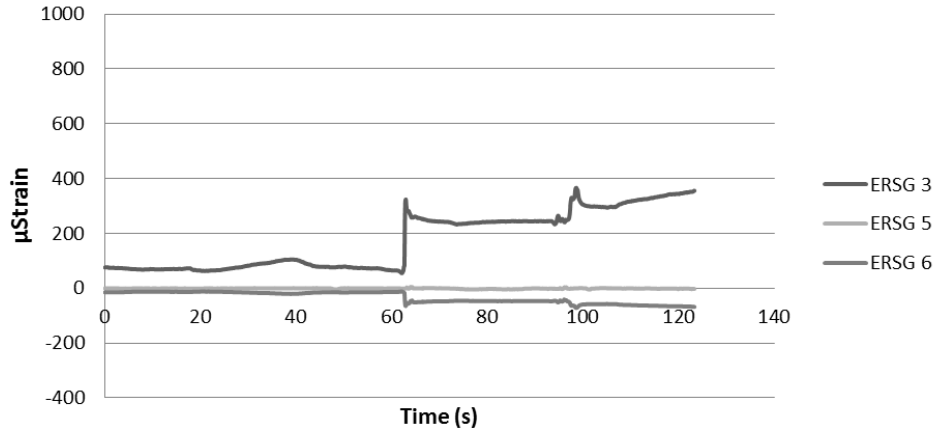

a) Test 1

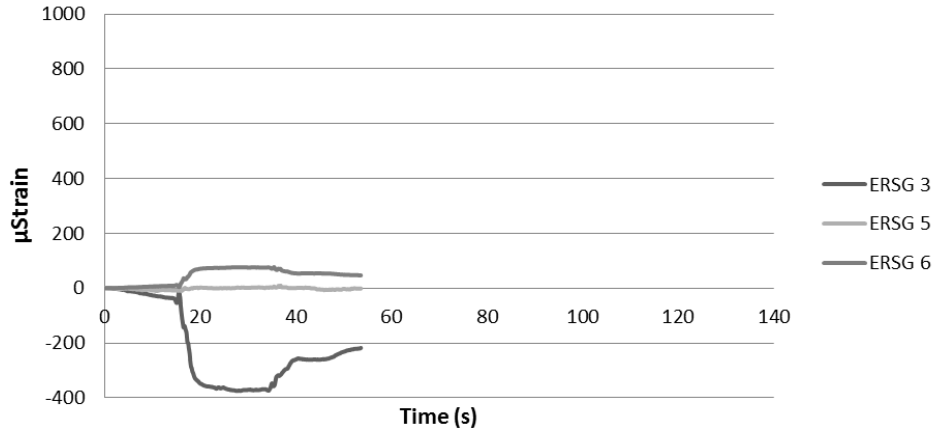

b) Test 2

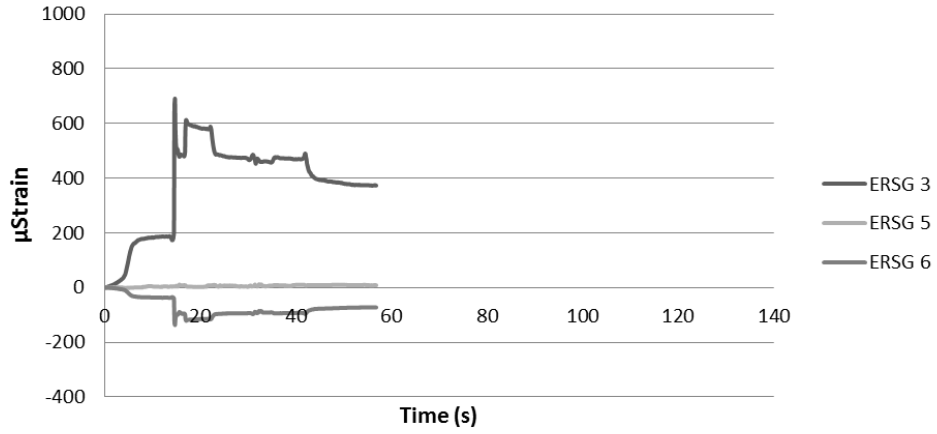

c) Test 3

Figure 3.54: Load Case 1, 5 mph pass

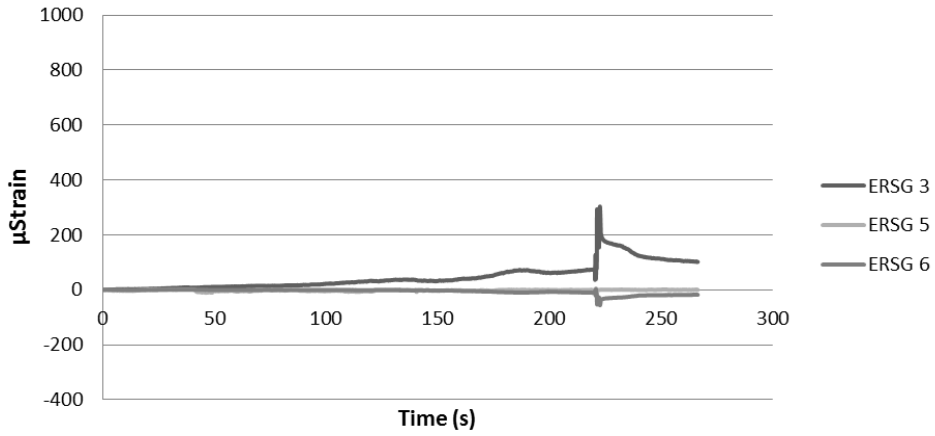

a) Test 1

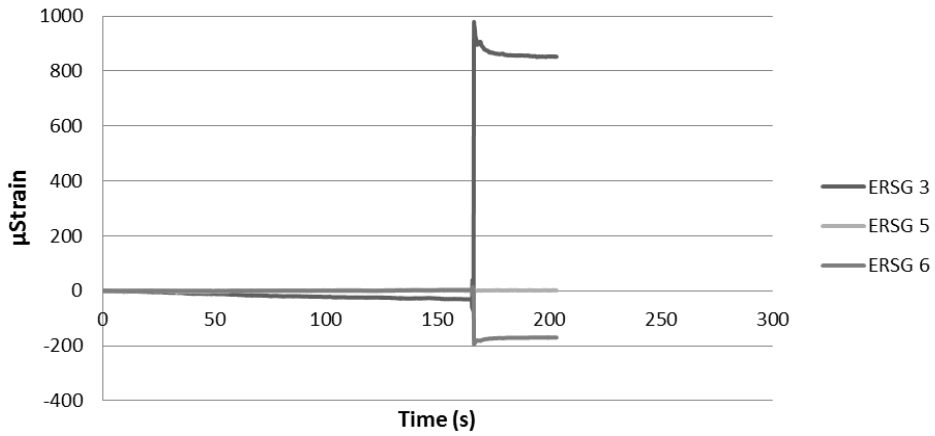

b) Test 2

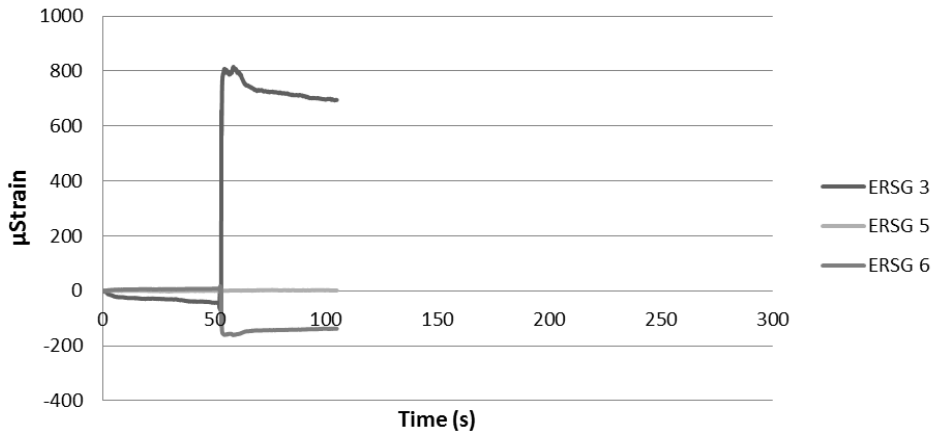

c) Test 3

Figure 3.55: Load Case 1, 45 mph pass

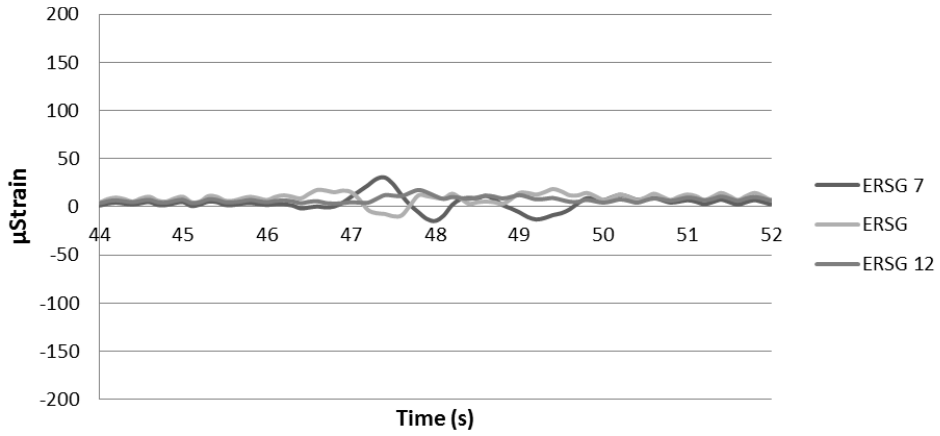

a) Test 1

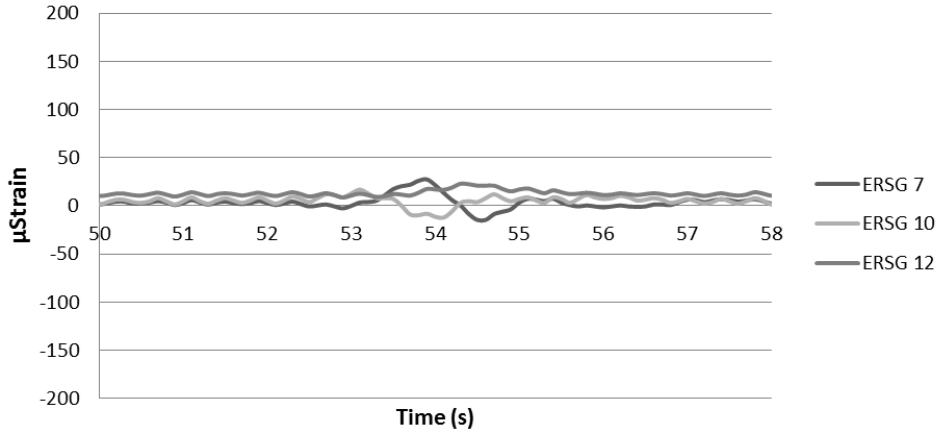

b) Test 2

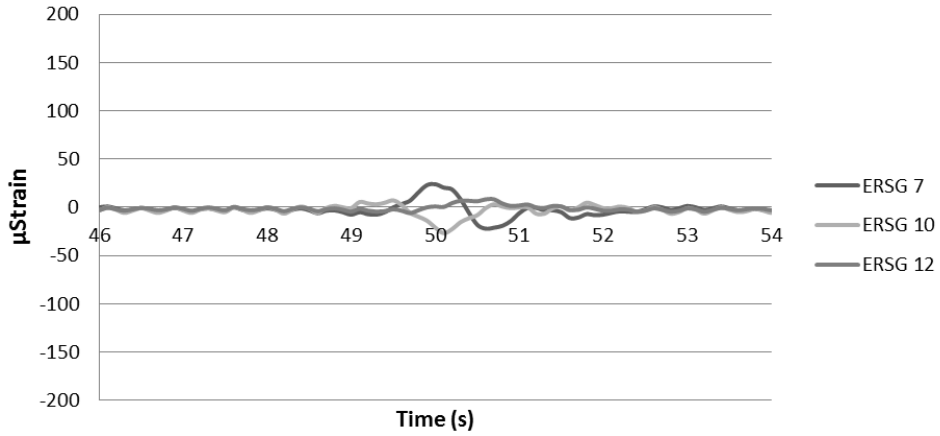

c) Test 3

Figure 3.56: Load Case 2, 5 mph pass

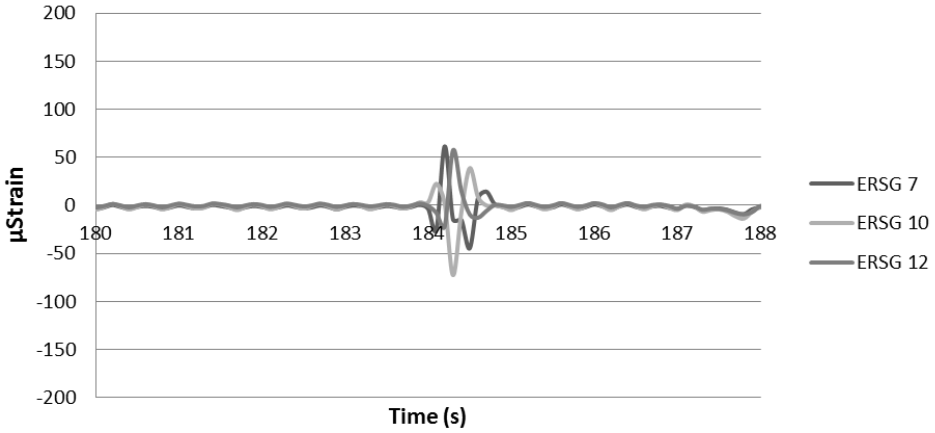

a) Test 1

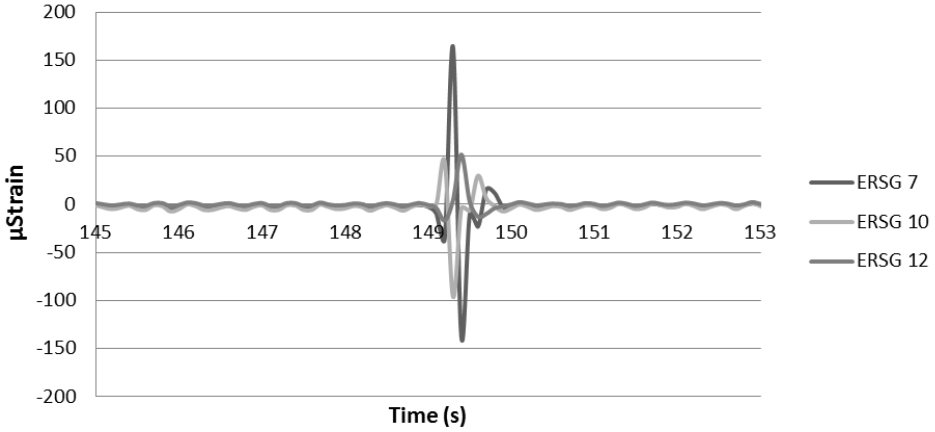

b) Test 2

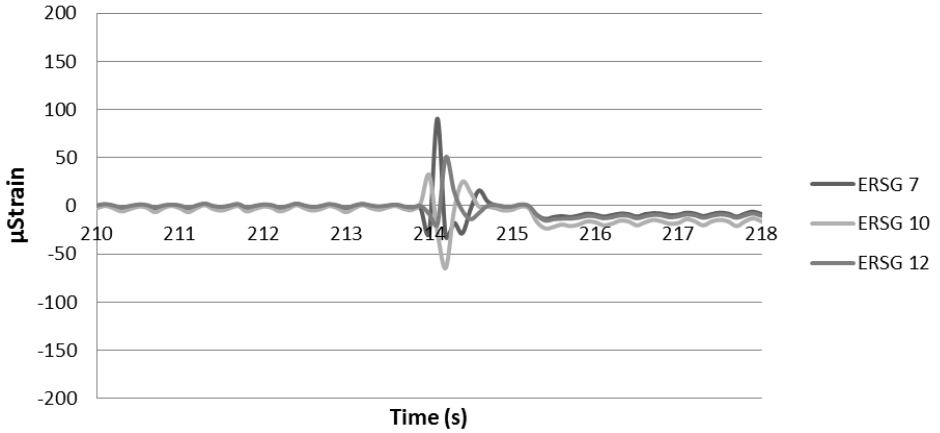

c) Test 3

Figure 3.57: Load Case 2, 45 mph pass

Table 3.22: Static load test results – Load Case 3

Static Load Test Results- Load Case 3				September 16, 2013
Gage	Measurement	Load Condition	μStrain	ΔμStrain
VWSG-T1	1	Before	221.1	-1.1
		During	220.0	
	2	Before	220.2	1.1
		During	221.3	
	3	Before	222.6	0.1
		During	222.7	
VWSG-T2	1	Before	113.9	0.6
		During	114.5	
	2	Before	114.3	1.7
		During	116.0	
	3	Before	114.3	2.7
		During	117.0	

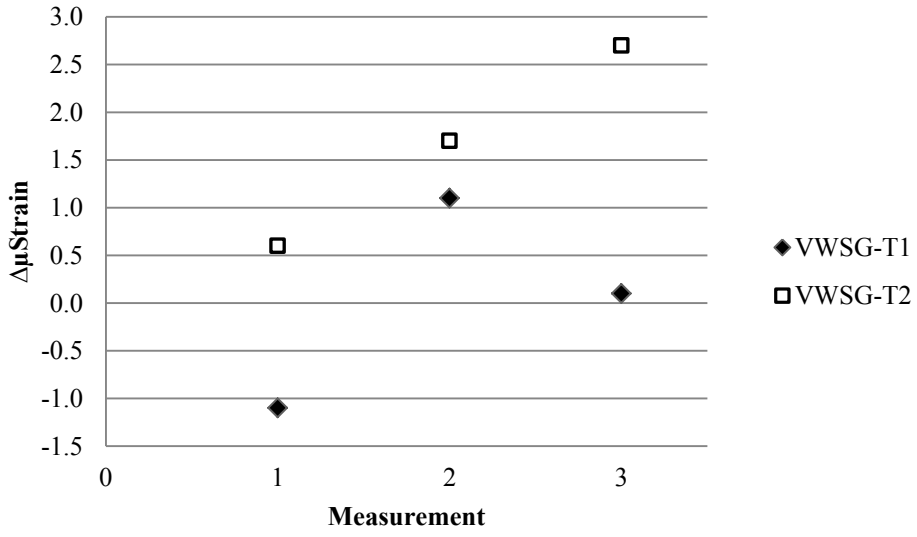

Figure 3.58: Static load test results – Load Case 3

Table 3.23: Static load test results – Load Case 4

Static Load Test Results- Load Case 4			September 16, 2013	
Gage	Measurement	Load Condition	μStrain	ΔμStrain
VWSG-P1	1	Before	178.2	5.9
		During	184.1	
	2	Before	178.2	7.7
		During	185.8	
	3	Before	179.4	6.6
		During	186.0	
VWSG-P2	1	Before	201.2	0.1
		During	201.3	
	2	Before	204.6	-0.1
		During	204.5	
	3	Before	203.0	-0.1
		During	202.9	
VWSG-P3	1	Before	87.2	-1.4
		During	85.9	
	2	Before	88.1	-1.3
		During	86.8	
	3	Before	89.0	0.0
		During	89.0	
VWSG-T3	1	Before	195.4	1.0
		During	196.5	
	2	Before	195.3	3.2
		During	198.6	
	3	Before	199.7	-1.1
		During	198.6	

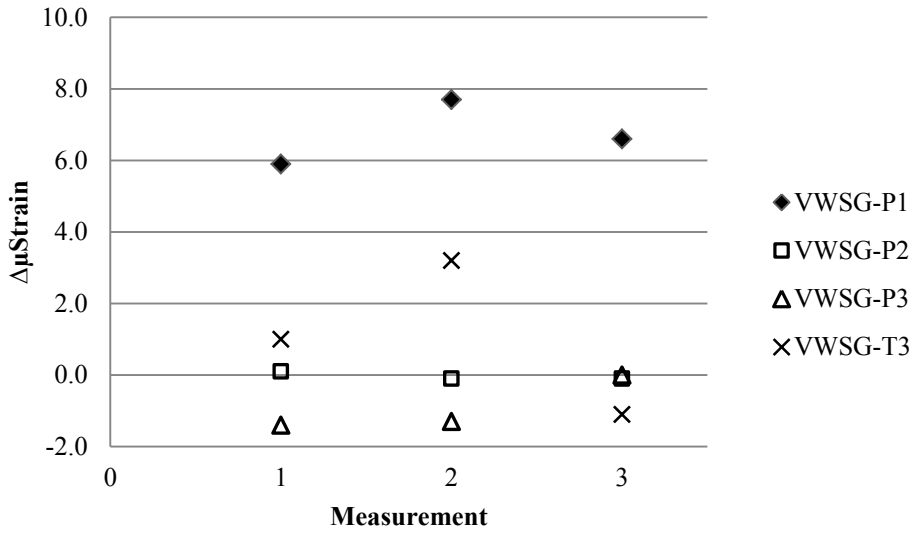

Figure 3.59: Static load test results – Load Case 4

3.7 DISCUSSION OF RESULTS

The results of long-term monitoring of strains and displacements on the Bent One and Bent Four approaches are discussed below as well as the results from the first load test on the Bent One approach.

3.7.1 Long-term Measurements

Discrete measurements collected from VWSGs, ERSGs, and VWDGs during the casting of approach slabs, general construction of bridge approaches and adjoining roadway, and after 3 months and 6 months of service are discussed in the following sections.

3.7.1.1 Vibrating Wire Strain Gage

Discrete measurements collected from VWSGs placed within the Bent One approach slabs and shear key closures show similar trends. Variation in strain is shown in Figures 3.45, 3.46, and 3.47. To assess overall performance of the approach slab system the strain readings collected during the first 6 months of service are considered relative to

measurements recorded 3 days after casting. At this time (3 days after casting) the concrete was hardened and the approach slabs were fully supported by rigid steel decks in the precast yard. In similar fashion, strain readings collected during the first 6 months of service from VWSGs located in the shear key closures were compared with strain readings collected immediately after concrete was placed in the closures.

From Section 9.5.2.3 of the ACI 318-08 code the tensile rupture stress (f_r) for normal weight concrete may be taken as:

$$f_r = 7.5 \lambda \sqrt{f'_c} \qquad \text{(Equation 9-9) ACI 318-08}$$

Where λ, a modification factor for light-weight concrete, is equal to 1.0 for normal weight concrete and f'_c is the compressive strength of the concrete. Equation 9-9 can be used to estimate the tensile rupture stress of the concrete. Using the relationship between stress and strain, given by the modulus of elasticity (E_c), the tensile rupture strains can be estimated for each batch of concrete (Table 3.24). The tensile rupture strains (ε_r) for the concrete used in the approach slab systems are on the order of 150 μStrain.

Based on commentary from Section R10.2.6 of the ACI 318-08 code, the compressive strain at ultimate stress (ε_c), where significant cracking begins to occur, is between 1,500 to 2,000 μStrain. For the purposes of this report, a value of 2,000 μStrain will be considered the cracking strain for areas of the approach slab system in compression. The values of compressive cracking strains are also shown in Table 3.24.

Table 3.24: Concrete cracking strains for approach slab system

Batch	Used For	f'_c (psi)	E_c (10^6 psi)	f_r (psi)	ε_r (10^{-6})	ε_c (10^{-6})
1	Slab B	10,640	5.67	774	136	2,000
2	Slab C	10,653	5.73	774	135	2,000
3	Slabs A, D	9,680	5.70	738	129	2,000
4	Shear Key	5,395	3.18	551	173	2,000

Strain readings collected from VWSGs within the approach slabs are significantly less than the expected tensile rupture strains for the concrete approach slab system. For VWSGs placed within the approach slabs, the measured strains range from around 1 μStrain up to 26 μStrain relative to the strain conditions 3 days after the approach slabs were cast. All three VWSGs within the approach slabs showed tensile strains after 6 months.

Strain readings collected from VWSGs placed within the shear key closures range from around 16 μStrain to around 50 μStrain relative to the strains occurring immediately after concrete placement. Both VWSG-T1 and VWSG-T3, located within shear key closures nearest the perimeter of the roadway, indicate tensile strains whereas VWSG-T2, located in the center shear key closure, showed compressive strains. Overall strains within shear key closures are slightly larger than the strains occurring within the approach slabs but still much less than the expected rupture strains.

Strain measurements collected from VWSGs within both the precast approach slabs and the shear key closures are within the tolerable limits for cracking of the concrete.

3.7.1.2 Electrical Resistance Strain Gages

Discrete strain measurements collected from ERSGs placed within the Bent One approach slabs were inconsistent. Some ERSGs seem to provide data that is reasonable and concurrent with data collected from nearby VWSGs but a significant number of ERSGs show unrealistic strain readings.

Strain readings collected after 6 months of service range from as little as 28 μStrain up to more than 2,600 μStrain relative to strain readings collected immediately after precast slabs were set on the Bent One approach. Based on compressive strength and modulus of elasticity tests, the compressive rupture strains, shown in Table 3.24, for the concrete used in the approach slab systems is on the order of 2,000 μStrain and the tensile rupture strains are on the order of 150 μStrain. Many of the ERSG readings, however, exceed these strains even though the VWSG readings are significantly less than rupture strains. Furthermore, the approaches show no visual signs of distress. Given that these measurements are recorded during live-load free conditions strain readings well beyond the rupture strains are not anticipated. It is likely that the long-term discrete readings collected from ERSGs do not reflect the actual behavior of the approach slab system.

The exact cause of noise within the data set is difficult to determine, however, ERSGs are often unreliable. Some difficulty collecting data from ERSGs arose during the dynamic load testing that could be related to data acquisition systems. It is possible that similar issues could be the reason for scatter in the long-term measurements as well. Furthermore, it is important to note that temperature variations occurring at different

times of data acquisition can cause readings that are not related to stresses due to service load conditions.

Due to the nature of the results no conclusions are drawn as to the performance of the approach slab system based on the long-term discrete ERSG measurements.

3.7.1.3 Vibrating Wire Displacement Gages

Displacement measurements collected from all four VWDGs on both the Bent One and Bent Four approaches show similar trends with respect to initial readings. The total displacement of the VWDGs from the initial reading up to 6 months of service ranges from approximately 0.05 mm up to 1.51 mm. The largest displacement was observed for VWDG 2, (Table 3.20), which is attached to approach slab 'A' located on the Bent One approach. The other VWDGs all show very low displacements, less than 0.25 mm, with VWDG 3 showing virtually no movement. After 6 months of service VWDGs 2, 3, and 4 all exhibited extension relative to the initial reading whereas VWDG 1 showed contraction relative to the initial reading.

Relatively small changes can be observed in the displacement readings before and after the cover plate installation. These changes are not a result of displacement of the bridge approaches and the movements described above take into account the differences between displacement before and after the cover plates were installed. It is difficult to identify with certainty the cause of these small variations. A reasonable conclusion is that during the drilling of holes, which house the anchor bolts by which the cover plates are attached, the displacement gages may have been disturbed slightly by the vibration of the hammer drill. The anchor holes for the cover plates are fairly close to the anchors which attach the displacement gages to the parapet. However, these changes are small, ranging

from 0.05 mm to 0.50 mm, and are accounted for because they are measured immediately before and immediately after the installation.

The displacements measured from VWDGs on both the Bent One and Bent Four approaches are relatively small and show trends that are concurrent with one another. Because readings from VWDGs are small, maximum displacement of approximately 1.50 mm, it is likely that movements or settlement of the approach slabs relative to the cast-in-place bridge deck are also small.

3.7.2 Load Testing

A discussion of load testing results on the Bent One approach slab is presented in the following commentary.

3.7.2.1 Dynamic Loading

Results from the first dynamic load test on the Bent One approach at 6 months after bridge completion were mixed between Load Cases 1 and 2. The individual Load Case 2 tests for both 5 mph and 45 mph were consistent for each case. However, the Load Case 1 tests for both 5 mph and 45 mph were less coherent.

The strain profiles of individual tests for the 5 mph passes are very similar showing maximum strains for each gage that are consistent for all three tests. The largest strains occurred on sensor ERSG 7 which is located near the center shear key closure at the middle of the roadway. Very similar strain magnitudes were recorded for both ERSG 10 and 12 which are located next to the shear key closure adjoining approach slabs 'A' and 'B'. A maximum strain for each test was consistently around 30 μStrain and minimum strain of around 15 μStrain was typical for each test. These strains are well below the calculated rupture strains for the precast concrete approach slab systems shown

in Table 3.24. The Load Case 2 strain profiles for each of the 45 mph tests are similar but show some variations in magnitude. Once again the largest strains occurred on sensor ERSG 7 which is located near the center shear key closure at the middle of the roadway. In general ERSG 10 and 12, located next to the shear key closure adjoining approach slabs 'A' and 'B', experienced lower strains that were similar to one another. The maximum strain for the series of the tests was around 160 μStrain while the minimum strain (based on the largest strain excursion for each gage) was around 50 μStrain. During Test 2 the maximum strain recorded on ERSG 7 exceeded the expected rupture strains by approximately 50 μStrain. It is therefore possible that some cracking of the approach slabs could have resulted from this load event. However, all the other strain readings for each of the Load Case 2 tests are below the expected rupture strains (Table 3.24) of the precast concrete approach slabs.

The Load Case 1 tests results do not represent expected behavior of the approach slab system. Both 45 mph and 5 mph tests show highly variable results with maximum strains varying by magnitudes as much as 1,000 μStrain or more for the same test conditions. Both compressive and tensile strains were recorded during the 5 and 45 mph passes but strain readings do not follow a harmonic profile as for the Load Case 2 results. Virtually every Load Case 1 test results show high residual strains long after loading from the trucks. Maximum strains for the 5 mph tests are around 700 μStrain and for the 45 mph tests are nearly 1,000 μStrain. These strains are greater than the calculated rupture strains for the precast concrete approach slabs.

During the load testing for both Load Case 1 and 2 anomalies with data acquisition occurred. This resulted in a limited number of strain gages being available for collection

of data. Three sensors were able to be utilized for the each load case. The exact reason for this difficulty with data acquisition is being examined at this time. By their nature, ERSGs are sometimes unreliable due to issues associated with damage of the wiring embedded in the concrete and waterproofing of the gages.

When considering the Load Case 2 test results for both 5 mph and 45 mph passes strains are mostly below the calculated rupture strains. A single strain gage experienced strains larger than the rupture strains for the precast concrete slabs during one of the 45 mph pass Load Case 2 tests. However, this strain was much higher than all other strains and still only exceeded the expected rupture strains by about 50 μStrain. Data collected from strain gages during the Load Case 1 does not allow for the drawing of firm conclusions at this time.

3.7.2.2 Static Loading

Results from the first static load test on the Bent One approach at 6 months after bridge completion were very similar for Load Case 3 and 4. Both approaches experienced very low strains during static loading. Strain readings for both load cases range from 0 μStrain to around 8 μStrain and are shown in Tables 3.22 and 3.23. Some gages experienced both tensile and compressive strains during loading and some gages showed either tensile or compressive strains only. VWSG-P1 showed the largest strains ranging from 5.9 to 7.7 μStrain (Table 3.23) whereas the other gages experienced very low strains most of which were around 1 μStrain or less. No clear trends of increasing strains that may be indicative of damage were observed. Overall discrete VWSG readings collected during static load tests at 6 months after bridge completion were very low, with maximum less than 8 μStrain.

3.7.3 Visual Observations

Visual inspections were conducted during on-site visits at 3 months and 6 months after the bridge was completed. No visual signs of distress or damage due to service loads, such as cracking or distortions in the pavement surface or around parapets near the approach slab system, were observed.

3.8 CONCLUSIONS

After 6 months of service, both the Bent One and Bent Four approach slab systems on the replacement bridge over Big Brown Creek in Union, SC appear to be functioning as intended based on long-term strain and displacement measurements as well as strain readings collected during load testing. No cracking or deformations have been observed around shear key joints connecting adjacent precast slabs or in other areas on the approach. Measured strains within precast panels and within shear key joints are generally below the calculated rupture strains for the approach slab system. Displacement readings collected from vibrating wire strain gages were small and indicate negligible movement of the approach slabs relative to the cast-in-place bridge deck.

Long-term strain measurements collected during live-load-free conditions, throughout the first 6 months of service, are generally well below the calculated rupture strains of the concrete approach slab system. Long-term Vibrating Wire Strain Gage (VWSG) readings show very consistent trends among different gages placed in the various locations within the approach slab system and the maximum measured strains relative to initial conditions are below the rupture strains. Long-term Electrical Resistance Strain Gage (ERSG) readings collected during live load free conditions, throughout the first 6 months of service are scattered. The reason for inconsistent long-

term results for the ERSGs is unknown at this time but ERSGs embedded in concrete are often unreliable. Long-term displacement readings collected during the first 6 months of service from Vibrating Wire Displacement Gages (VWDGs) show similar trends for all gages and overall seem to indicate negligible movement of the approach slabs relative to the cast-in-place bridge deck.

The first load test on the Bent One approach has been concluded and both dynamic and static load test results appear to indicate that the approach slab systems are functioning adequately. In general strain readings collected from ERSGs during dynamic load testing are below or, in one case, close to the expected rupture strains of the concrete. Strain measurements collected from VWSGs during static load tests were negligible.

This research project is ongoing. The results from long-term monitoring and load testing to be conducted over the remaining 12 months of the data acquisition schedule will be reported on in the future.

3.9 REFERENCES

ASTM C39 / C39M – 12a. 2012. Standard Test Method for Compressive Strength of Cylindrical Concrete Specimens. American Society for Testing and Materials, 5 1-12.

ASTM C469 / C469M – 10. 2010. Standard Test Method for Static Modulus of Elasticity and Poisson's Ratio of Concrete in Compression. American Society for Testing and Materials, 1-12.

ASTM C31 / C31M – 12. 2012. Standard Practice for Making and Curing Concrete Test Specimens in the Field. American Society for Testing and Materials, 1-7.

ASTM C143 / C143M – 12. 2012. Standard Test Method for Slump of Hydraulic-Cement Concrete. American Society for Testing and Materials, 1-5.

Building Code Requirements for Structural Concrete (ACI 318-08) and Commentary. 2008. An ACI Standard. Farmington Hills, MI.: American Concrete Institute

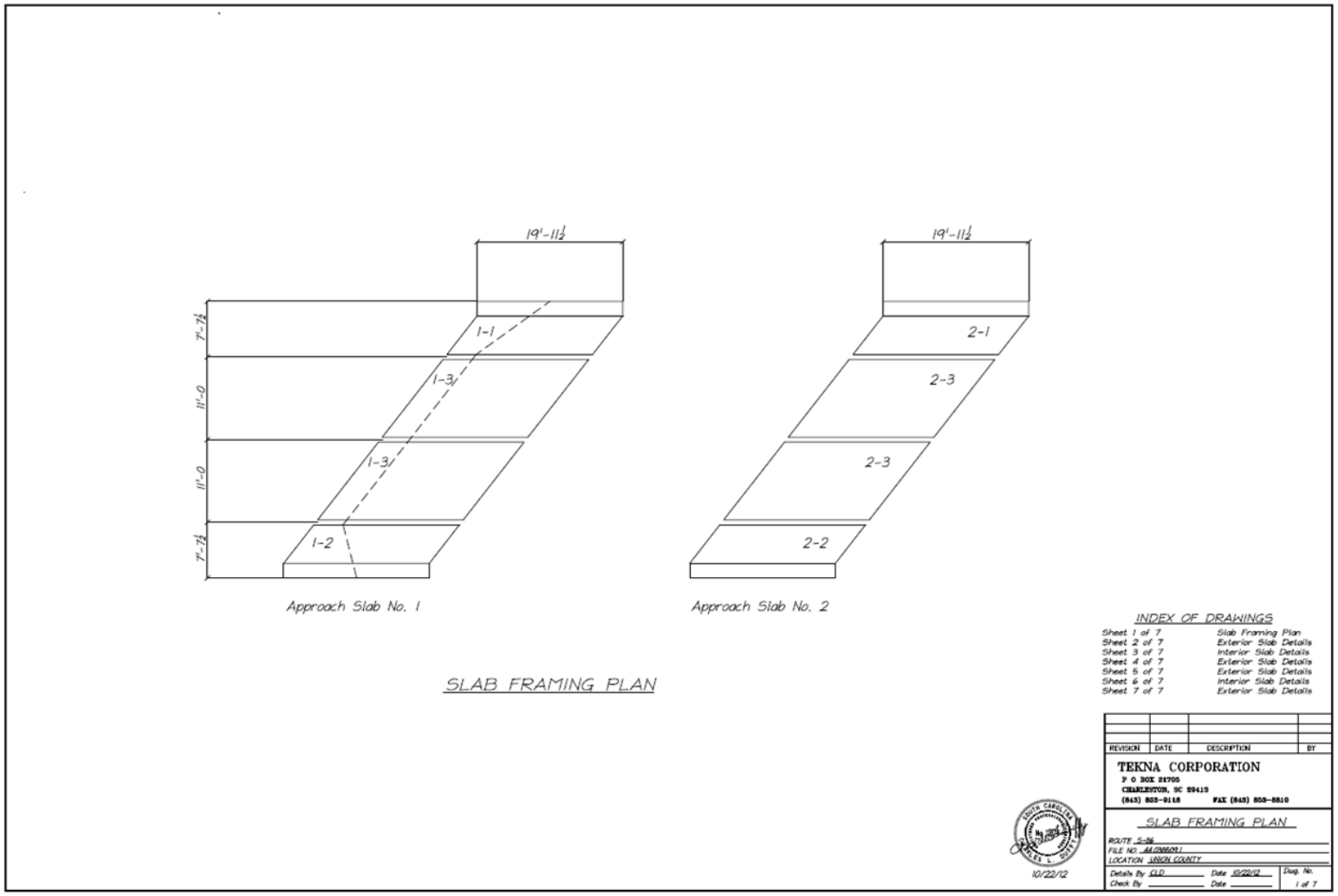

Figure 3.60: Approach slab framing plan

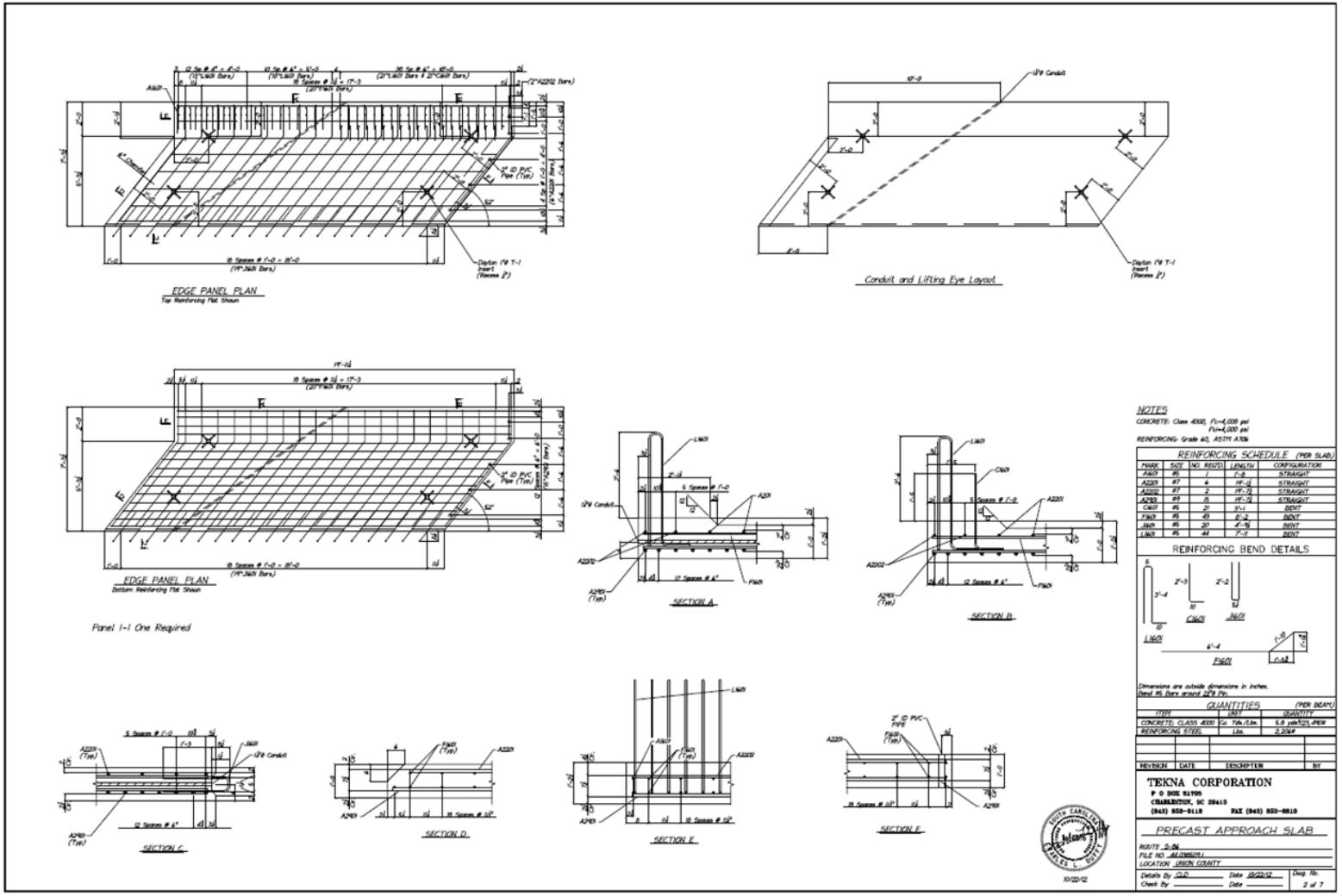

Figure 3.61: Bent One approach slab 'D' reinforcement schematic

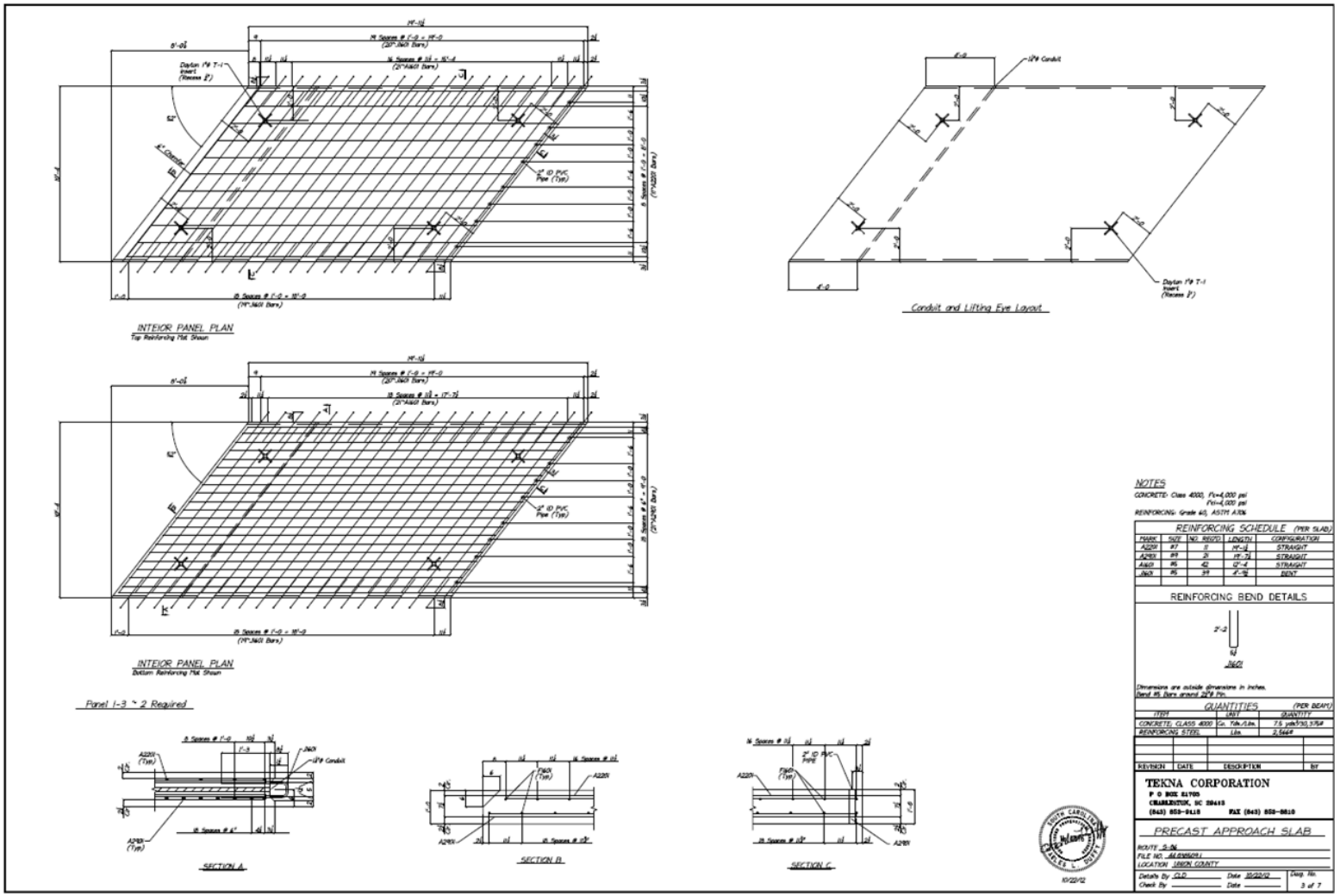

Figure 3.62: Bent One approach slabs ‘B’ and ‘C’ reinforcement schematic

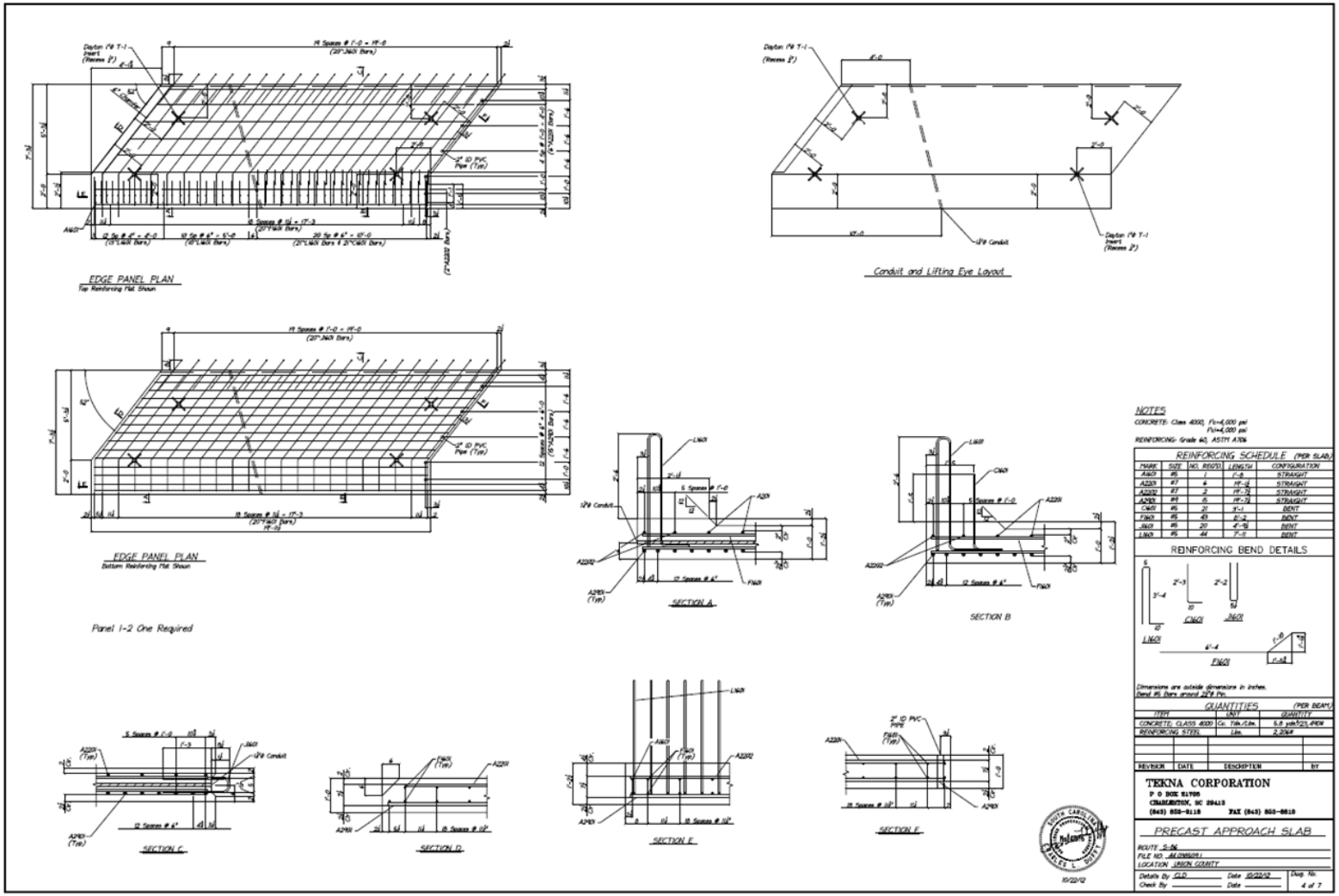

Figure 3.63: Bent One approach slab ‘A’ reinforcement schematic

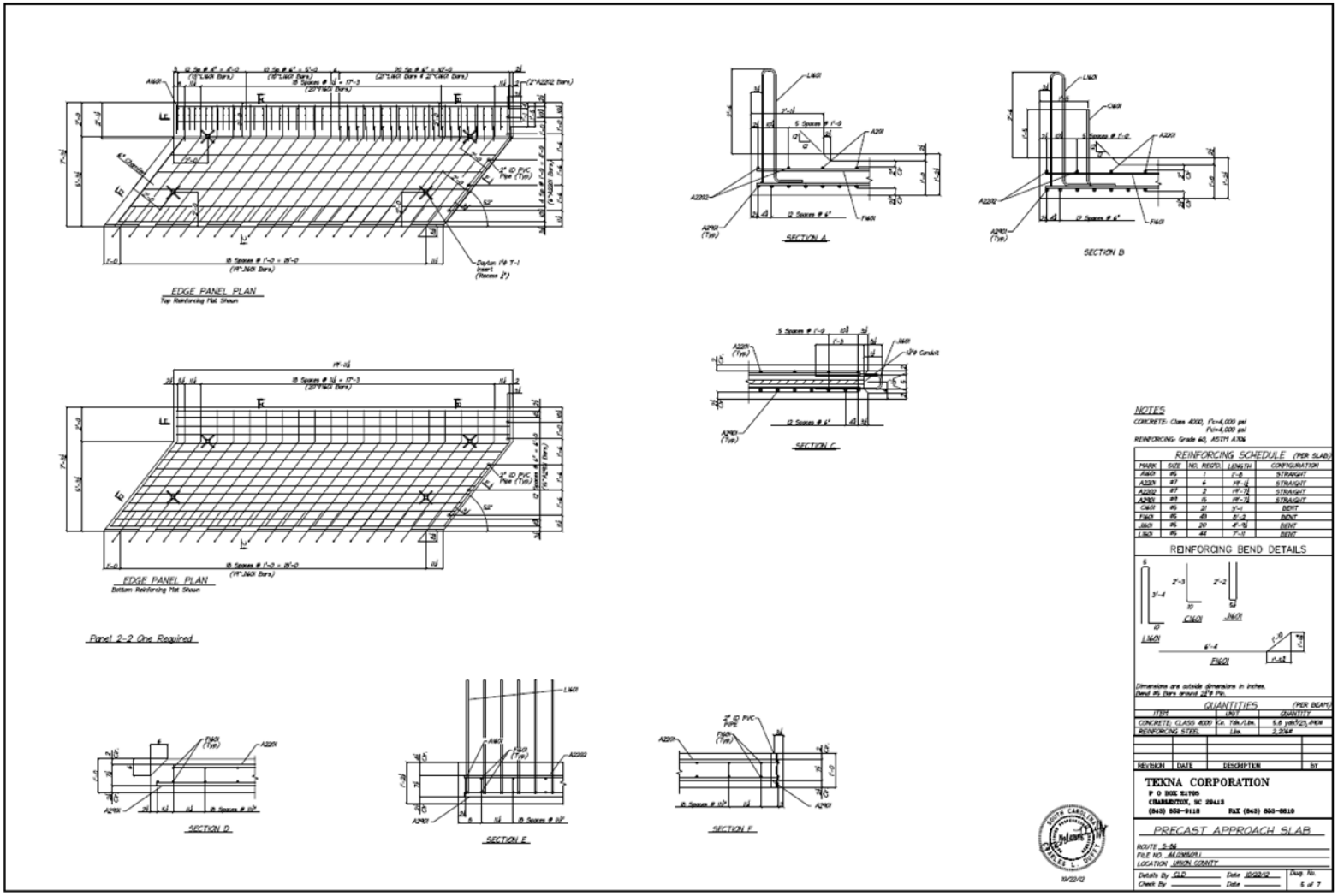

Figure 3.64: Bent Four ‘exterior’ slab 2-2 reinforcement schematic

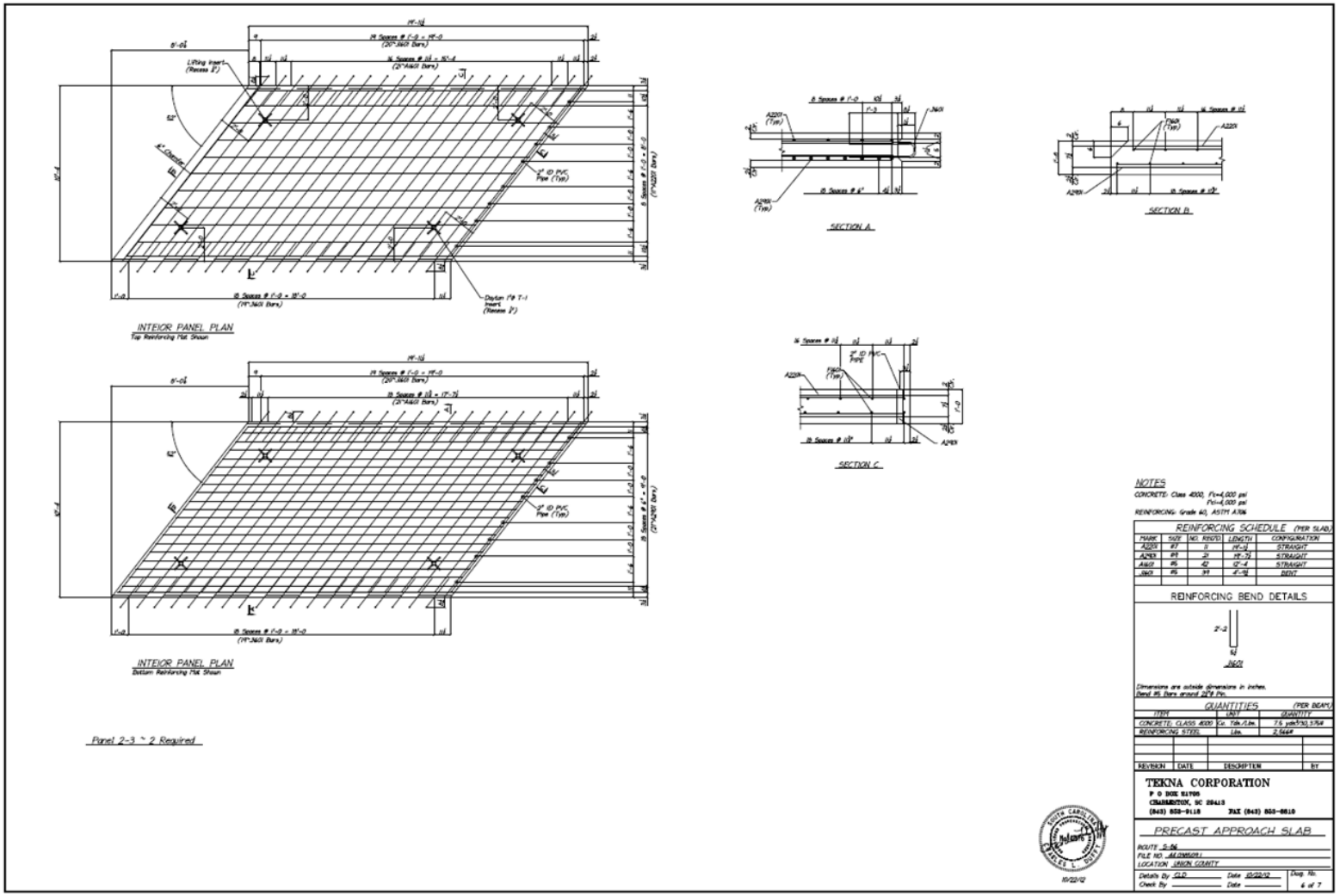

Figure 3.65: Bent Four ‘interior’ slab 2-3 reinforcement schematic

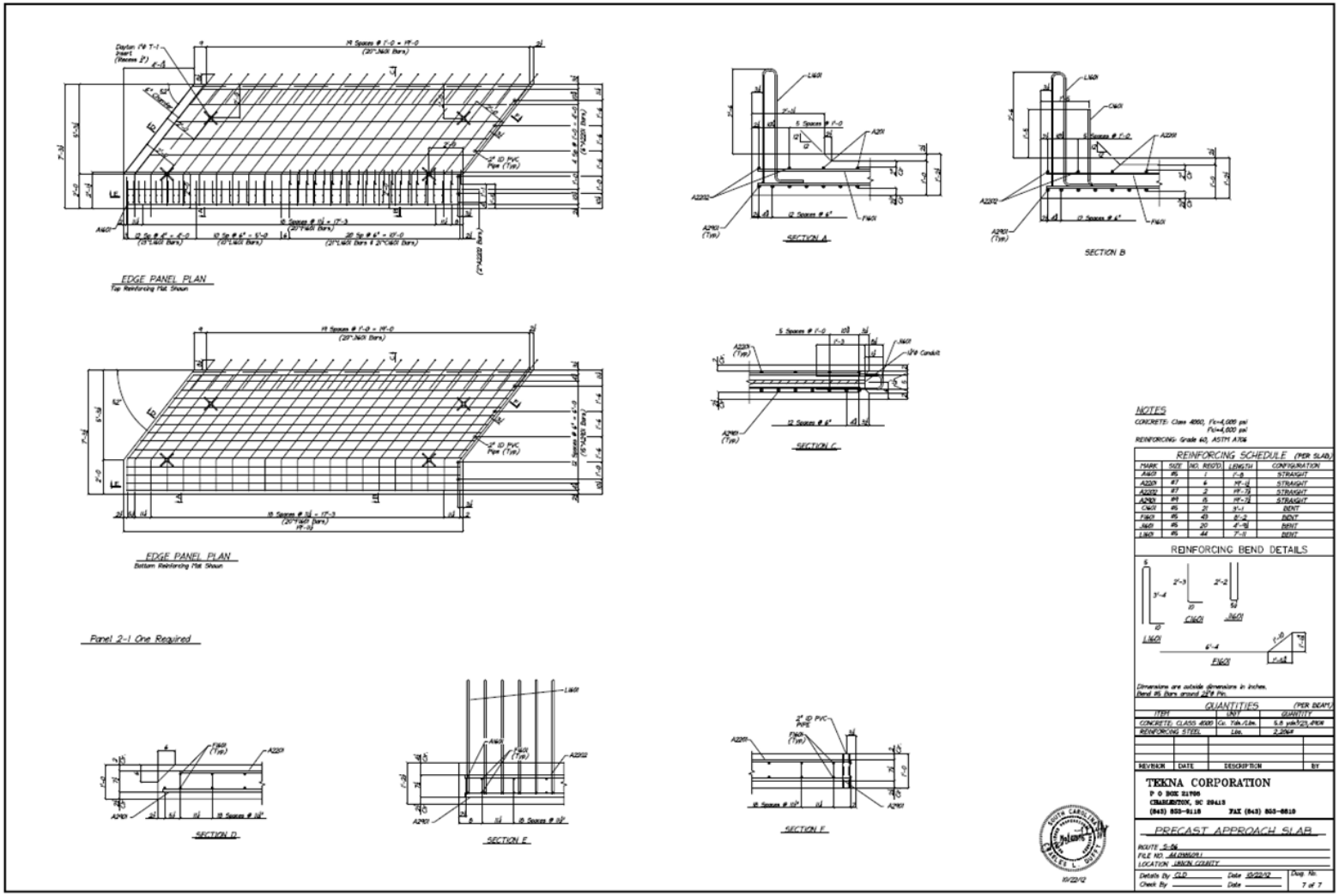

Figure 3.66: Bent Four ‘exterior’ slab 2-1 reinforcement schematic

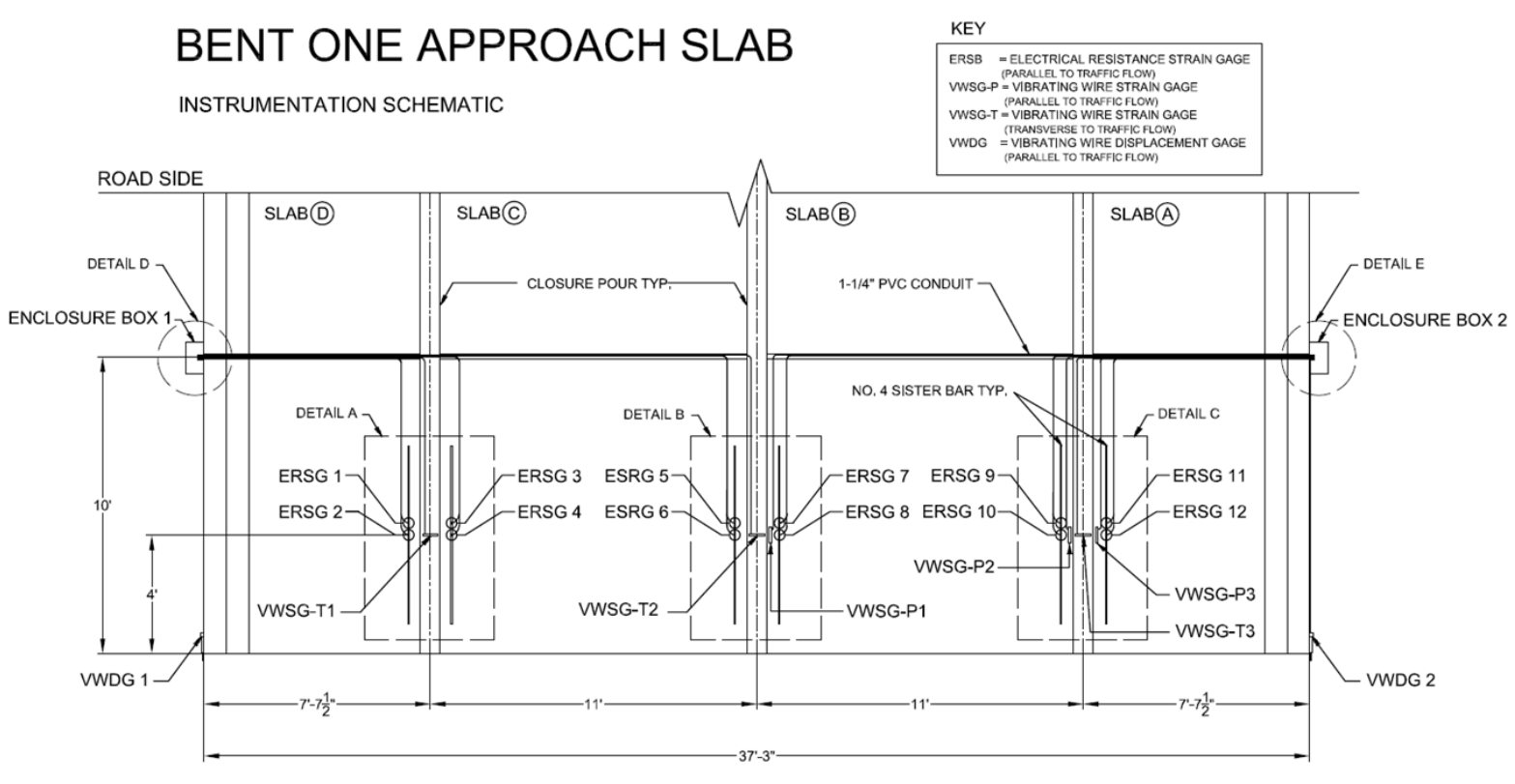

Figure 3.67: Bent One approach slab instrumentation schematic

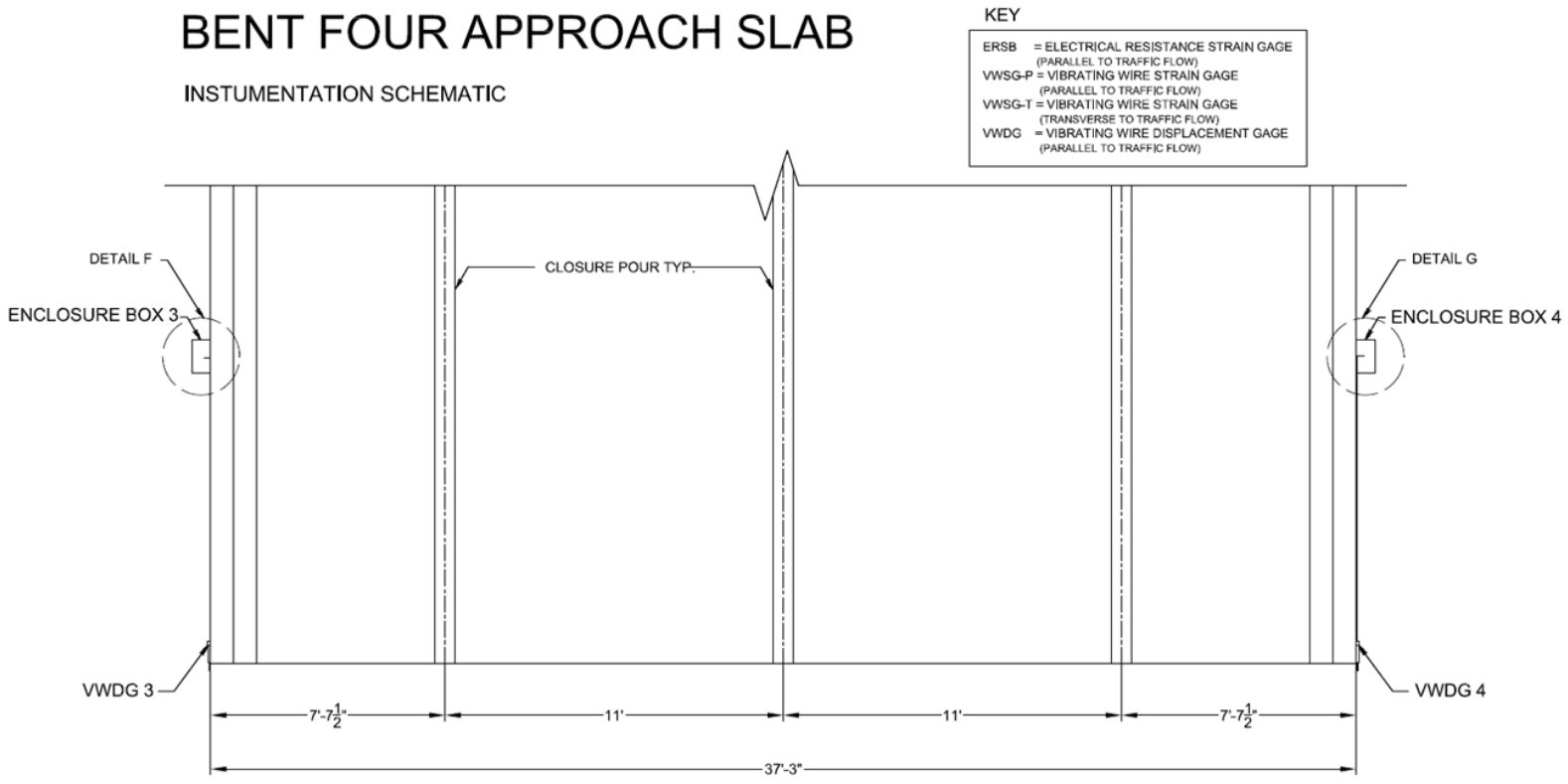

Figure 3.68: Bent Four instrumentation schematic

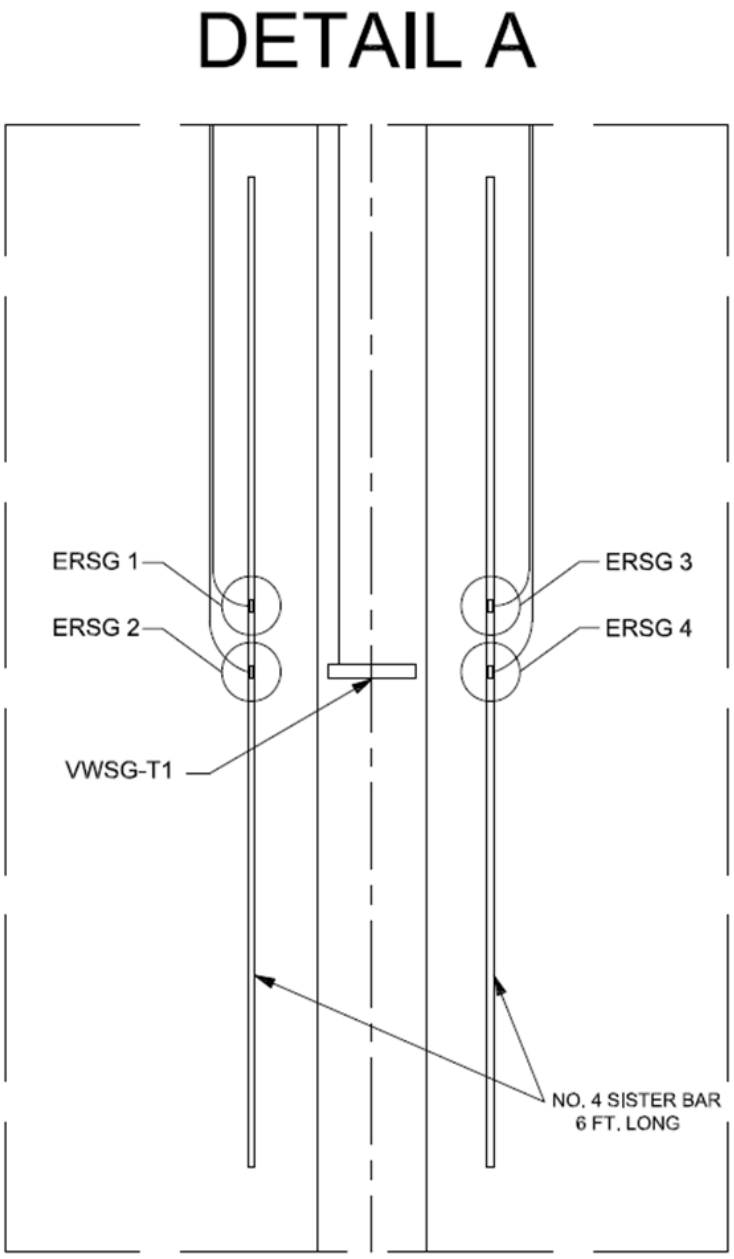

Figure 3.69: Bent One instrumentation schematic: Detail A

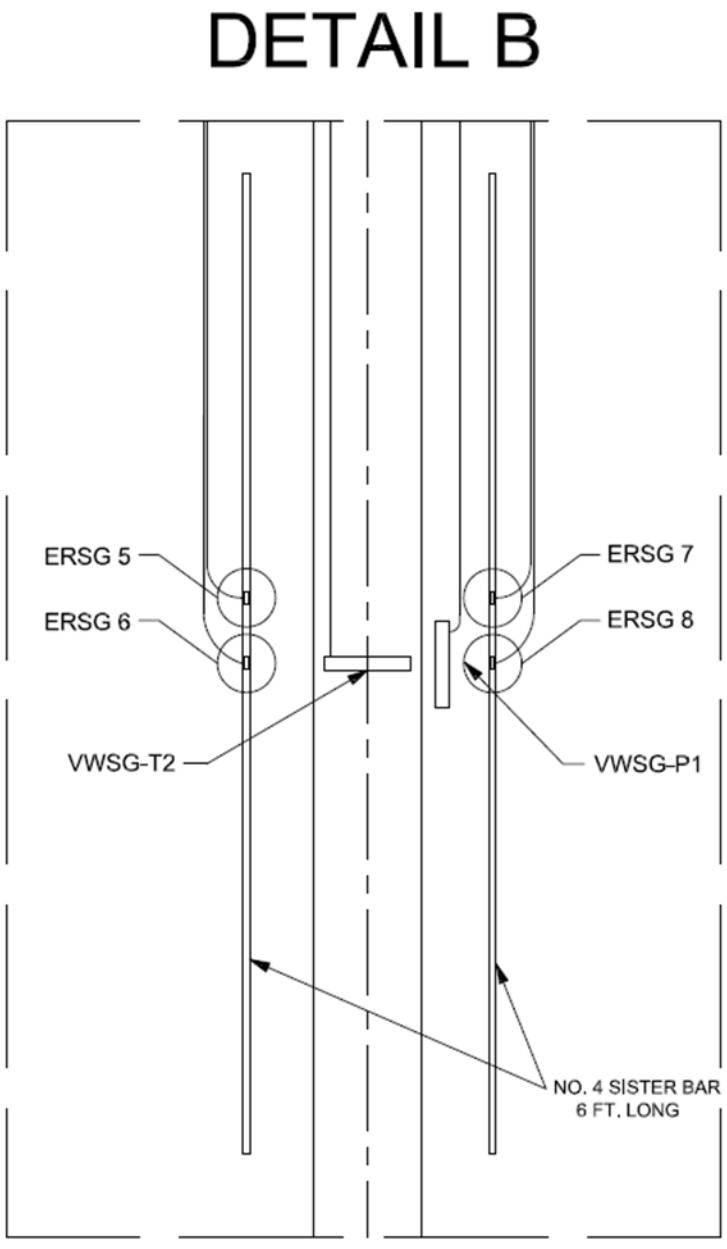

Figure 3.70: Bent One instrumentation schematic: Detail B

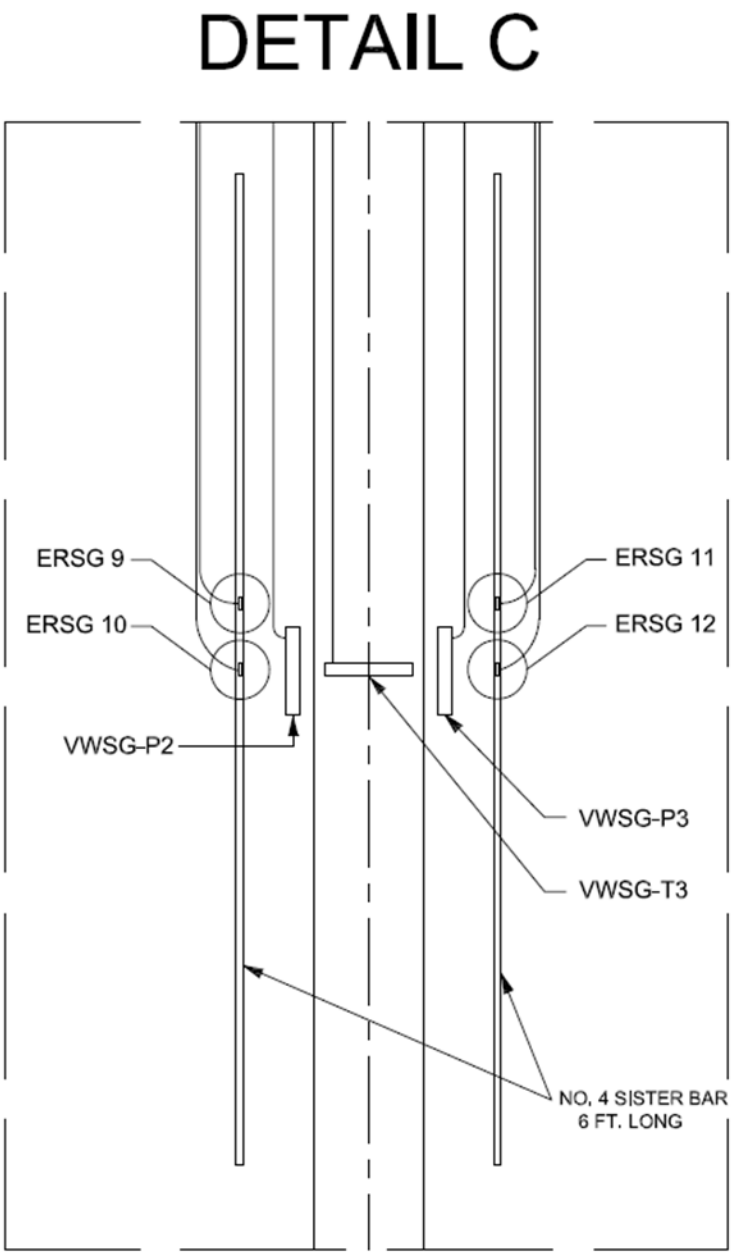

Figure 3.71: Bent One instrumentation schematic: Detail C

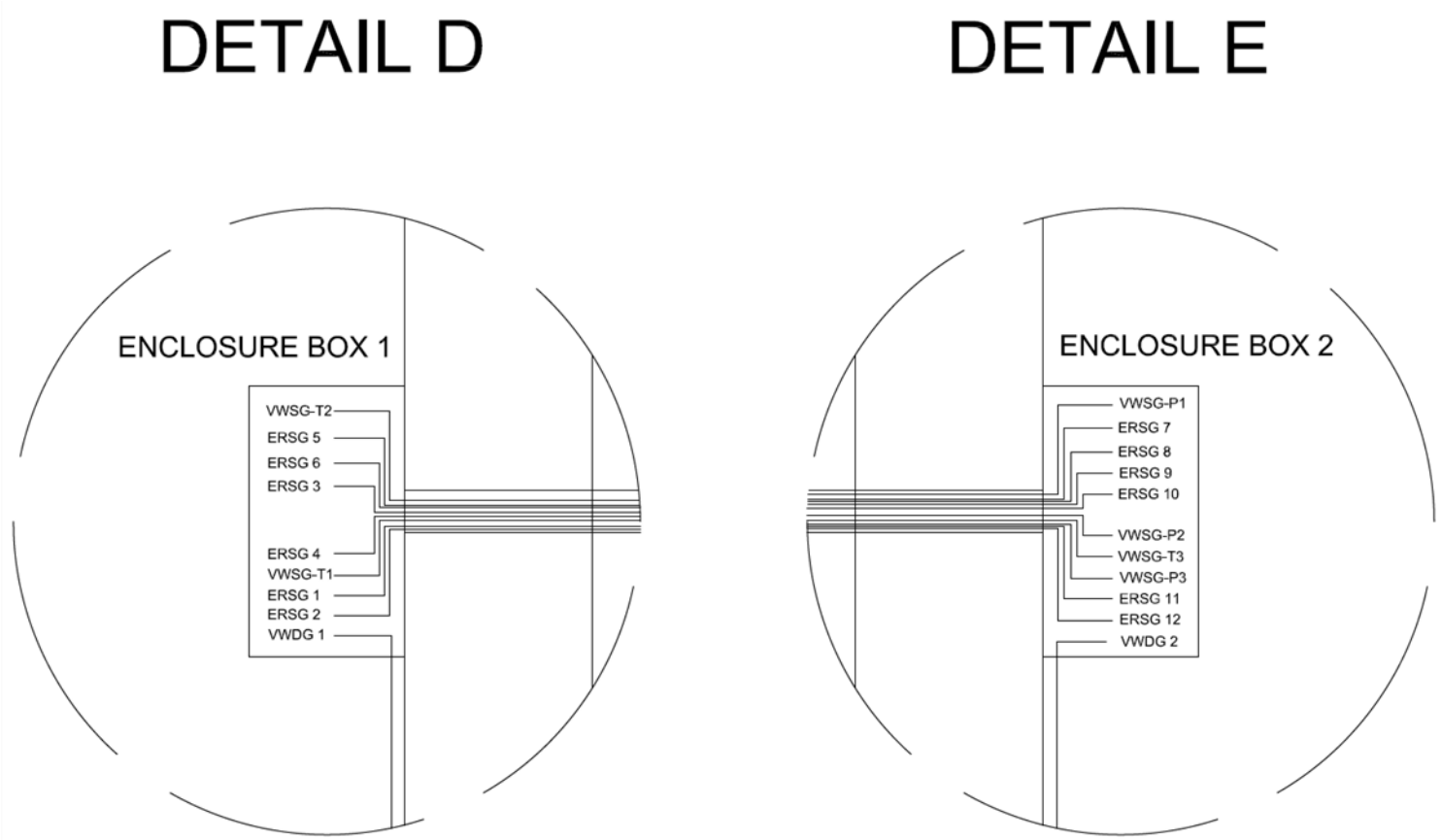

Figure 3.72: Bent One instrumentation schematic: Details D and E

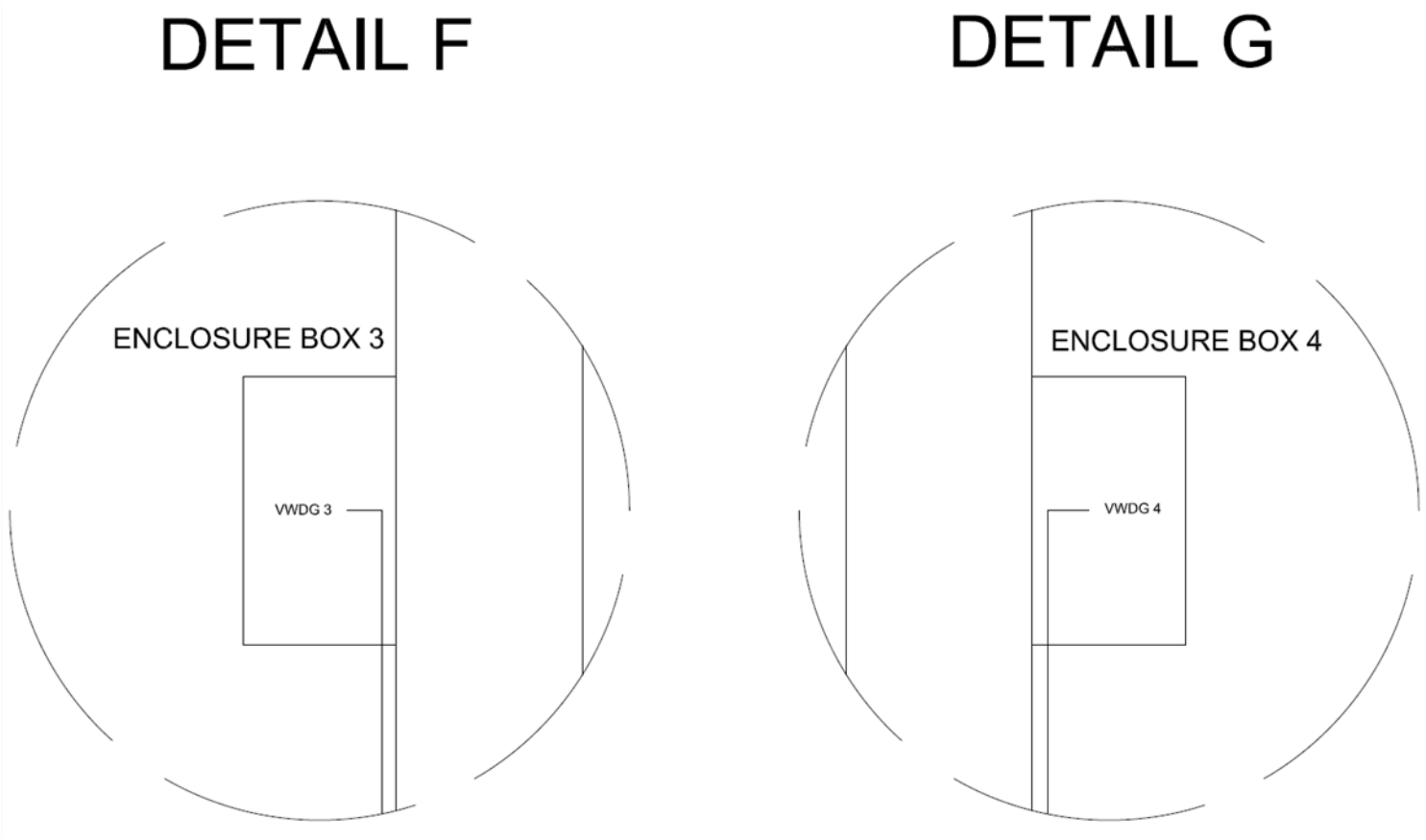

Figure 3.73: Bent One instrumentation schematic: Details F and G

CHAPTER 4

ASSESSMENT OF ALKALI-SILICA REACTION USING ACOUSTIC EMISSION[2]

[2] Matthew K. Jones, Mohamed ElBatanouny, and Paul H. Ziehl. To be submitted to the ASCE Journal of Materials in Civil Engineering.

4.1 ABSTRACT

An alkali-silica reaction (ASR) test was designed to examine the ability of acoustic emission (AE) to detect this damage mechanism. The test consisted of a modified ASTM C1293 experimental setup with twelve specimens of dimensions 3x3x11.25 in. The test specimens were created using an aggregate that is known to be highly reactive. In addition the mix design contained an elevated level of alkalinity. The specimens were placed in controlled environment with high temperature and relative humidity to accelerate the ASR reaction. ASR causes internal pressure in the concrete due to formation of expansive gel which leads to cracking and volume expansion. Length change measurements and petrographic examination were performed periodically to detect ASR damage while AE activity was recorded continuously. AE will enable the detection of micro-cracks forming prior to expansion, which can be related to the degree of ASR related damage. The results of this study show that AE enables the detection of ASR damage with a good agreement with length change measurements. Quantification of ASR damage may also be possible if AE intensity analysis is used.

Keywords: alkali-silica reaction, acoustic emission, ASTM C1293

4.2 INTRODUCTION

Alkali-silica reaction (ASR) is one of the primary chemical reactions causing degradation and loss of service of hardened concrete structures worldwide. ASR is reaction that occurs over time in concrete between aqueous alkaline hydroxides, within the pore solution of the cement paste (Na_2O and K_2O), and amorphous silica, within surrounding aggregates (Swamy 1998). The accumulation of expansive pressure created by the hydrated alkali silicate leads to micro-crack formation within both the cement

paste and aggregates. If left unchecked ASR can cause extensive map-cracking, spalling of joints, excessive movements, and ultimately loss of service and safety of a structure.

Currently the most popular method of preventing ASR related damage to concrete structures is proper selection of aggregates. This can be achieved through field performance assessment of a potential aggregate but aggregates with satisfactory long-term service records are not always regionally available. A number of various test methods have been developed to evaluate the potential of an aggregate to participate in expansive ASR. However, current testing methods have limitations. The two most prevalent standard test methods being used currently are the ASTM C1293 ("Concrete Prism Test") and the ASTM C1260 ("Accelerated Mortar Bar Test"). Both test methods have, in some cases, falsely identified aggregates as innocuous resulting in ASR related damage of in-place structures. For these reasons it is necessary to conduct field assessments in order to evaluate the condition of the structure.

Regular inspections are needed to determine the extent and rate of ASR deterioration. Visual inspection, however, only gives information related to the surface condition of concrete. Therefore, there is a need for an efficient non-destructive testing (NDT) method to monitor the progression of ASR. The lack of a NDT method that is able to detect ASR is a crucial issue, especially with the wide implementation of concrete in NPPs structures and the threat that radioactive leaking imposes. Excessive cracking in such elements might lead to compromising the ability of these structures to fulfill their intended functions. The NDT technique should enable (1) proper assessment of the rate of ASR deterioration and (2) evaluate the remaining service life of the structure. Acoustic emission (AE) methods have advanced significantly in the past years as a real-time,

passive NDT technique for evaluating damage in concrete structures. These advancements pave the way for developing a quantitative method for evaluating ASR (Ziehl 2008). AE is highly sensitive to stress waves emitted from sudden release of energy, such as concrete cracks (Ziehl 2008, Pollock 1986). This allows it to capture and identify propagating damage (ElBatanaonuny et al 2012, Mangual et al 2013). Possible applications of AE monitoring related to the progression of ASR include long-term monitoring and prognosis based on received AE data using parameter based methods.

An accelerated ASR test based upon the ASTM C1293 was designed to enable detection of ASR expansion in a reasonable time frame. The specimens were continuously monitored using AE. Length change measurements were performed periodically using a length comparator along with petrographic examination to serve as a benchmark for ASR detection. The objective of the research is to use AE to assess the development and rate of ASR distress in concrete for use in service life modeling. The results of the test showed the ability of AE to detect ASR progression with a good agreement with length change measurements.

Keywords: Structural health monitoring, non-destructive evaluation, acoustic emission

4.3 EXPERIMENTAL PROGRAM

4.3.1 Experimental Setup

The test matrix included four sets of three for a total of twelve specimens with dimensions of 3x3x11.25 in., according to ASTM C1293, in addition to three dummy specimens of the same dimensions. The primary difference between this test setup and ASTM C1293 is the alkalinity concentration where 5% $Na_2O_{(Eq)}$ was used in the concrete mix as opposed to 1.25% as specified in the ASTM standard. Also, due to the

significantly shortened time frame of this test, a more frequent length change measurement schedule than that of the ASTM C1293 was incorporated.

In addition to higher total alkaline content a highly reactive aggregate originating from Cheyenne, Wyoming, known as Knife River, was used for casting the test specimens. Typically in order evaluate the potential for a coarse aggregate to participate in deleterious ASR a known innocuous fine aggregate would be used as per ASTM C1293. However, for the purposes of this testing (significant ASR expansion desired) both the coarse and fine aggregates were used from the same source and are considered highly reactive. With this exception the aggregates follow the specifications identified in section 7.2 of ASTM C1293. A highly reactive aggregate was chosen in conjunction with elevating total alkaline content in order to ensure that an alkali-silica reaction would occur and that AE data related to expansive ASR damage could be captured within a reasonable period of time.

The specimens were placed in a controlled environment with a 100% relative humidity and temperature of 100±2˚F (Figure 4.2). A sealed insulating chamber was constructed to control the temperature. The chamber has approximate dimensions of 4x4x8 ft and consists of an aluminum frame covered with Lexan panels. In order to create a temperature stable environment a silicon adhesive sealant was applied to corners and seams and expanding polyurethane foam was used in areas where cables were routed into the chamber. A small electric heater with an internal fan (Figure 4.3) was placed inside the chamber and temperature was controlled by a digital thermostat mounted on the wall outside the chamber. Figures 4.2 and 4.4 show the chamber setup and the thermostat is shown in Figure 4.5.

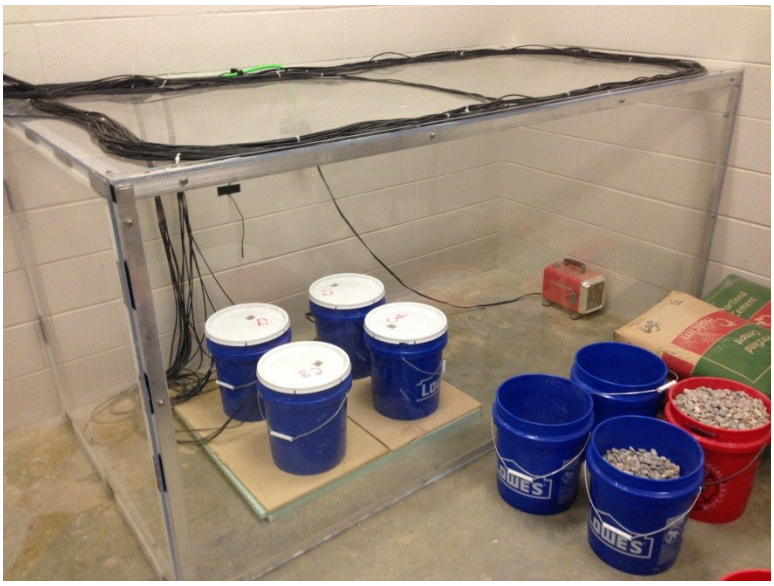

Figure 4.1: Temperature controlled testing chamber

To maintain 100% relative humidity, specimens were placed in polyethylene containers with sealing lids conforming to the specifications identified in section 5.2.2 of the ASTM C1293. The containers were lined with a polypropylene absorbent fabric. A specimen holder consisting of a bottom rack, central rod, and top plate was placed inside of each bucket.

Figure 4.2: Electric heater

Figure 4.3: Storage containers in test chamber

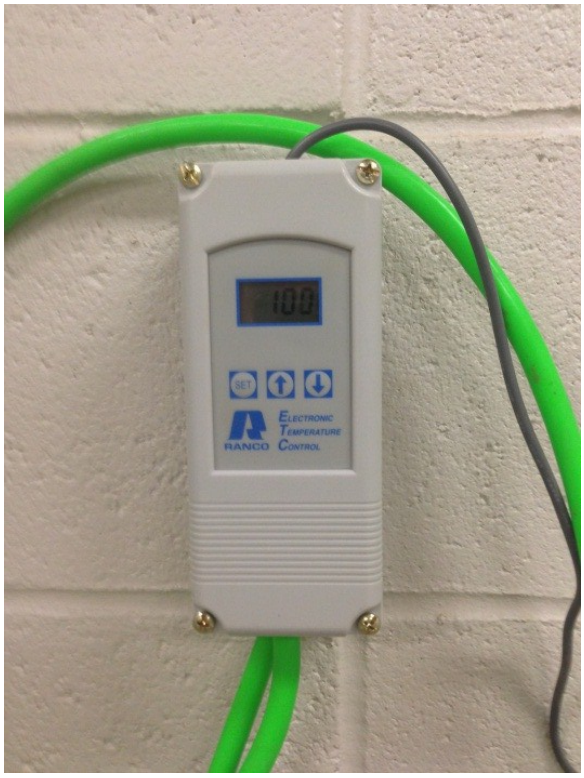

Figure 4.4: Digital thermostat

The purpose of the specimen holder assembly is to provide a means for the secure upright storage of each specimen. The specimen holder assembly was specially made at the University of South Carolina's (U.SC) machine shop and consists of materials that are chemically inert in high moisture environments. The bottom rack and top plate is made of PVC plastic and the central rod is machined from a high-grade stainless steel. This is an important consideration because the capability of AE to detect corrosion in materials has been shown (Idrissi and Liman 2003; Assouli et al. 2005). If any of the materials inside of the storage buckets are subject to corrosion there is a potential for data being captured that is unrelated to ASR damage. A photograph of the storage container and holder assembly is shown in Figure 4.6.

Figure 4.5: Storage container and specimen holder assembly

A single hole was cut in the side of each container to allow access for the AE sensor cables. Once sensor cables were routed into the containers these holes were sealed using rubber grommets and an adhesive silicon sealant. The containers were filled with tap water up to a depth of approximately 1 in. to maintain a relative humidity of 100 %.

The specimens are situated above the surface of the reservoir of water by resting on the bottom rack of the specimen holder assembly. A more detailed photo of the specimen holder with specimens is shown in Figure 4.7. The specimens were maintained in this position and were kept out of contact with the sides of the container. Each container housed 3 individual specimens, yielding a total of four containers.

Figure 4.6: Specimen holder assembly

The containers were rested on a 2.5 x 3.5 ft platform that consisted of two layers of ¾ in. rigid foam insulation and a single piece of ½ in. plywood. The electric heater was positioned at the far side of the chamber was placed on a similar platform. The platforms were provided in an attempt to create a buffer for the instrumented specimens and thus minimize collection of noisy or nonrelevant AE data originating from vibrations in the concrete floor below.

4.3.2 Concrete Materials and Mixture Design

Concrete prisms used for testing have mixture proportions (cement, water, coarse aggregate) designed using the specifications identified in the ASTM C1293. Two batches of concrete were used for making specimens both having the same mixture design and each batch yielding 6 specimens for a total of 12 specimens. Specimens from 'Batch 1' are labeled S1 through S6 while specimens from 'Batch 2' are labeled S7 through S12. The dummy specimens were cast prior to testing and contained aggregates and cement that are known to behave innocuously; they are labeled as D1 through D3.

The ASTM C1293 specifications and concrete mixture design are shown in Tables 4.1 and 4.2. The control specimens were selected from laboratory specimens previously cast that contained aggregates that are known to be innocuous.

Table 4.1: ASTM C1293 Section 7.3 specifications

w/c Ratio*=	0.45
Cement Content=	26.22 lb/ft^3
Volume of Coarse Aggregate per Unit Volume of Concrete=	0.70
**Alkali Content=	5.0% Na_2O_{eq}

* Based upon aggregate saturated surface dry

** Modified from ASTM C1293 (1.25 % $Na_2O_{(Eq)}$)

The coarse and fine aggregate originate from a quarry in Cheyenne, Wyoming and are known to be highly reactive. The properties of the aggregates are shown below in Table 4.3. The specific gravity (S.G.) and absorption were measured by The Wyoming Department of Transportation Materials Lab (Table 4.3). The unit weight of the coarse aggregate was measured at the University of Wyoming using ASTM C29 methodology and is also shown in (Table 4.3). The properties shown in Table 4.3 were used to

proportion the concrete mix as per the ASTM C1293 specifications. The grain size distribution of each aggregate (conforming to ASTM C1293) is shown in Table 4.4. The fine aggregate was sieved and proportioned such that a fineness modulus of 2.75 was achieved. Laboratory grade sodium hydroxide (NaOH) pellets were used to increase the alkalinity of the concrete. The Knife River aggregate and NaOH pellets are shown in Figure 4.8.

Table 4.2: Concrete mixture design

Modified ASTM C1293 Mix Design: One Batch of 6 Prisms ft^3					V_{tot}= 0.3515
Constituent	Weight (lb)	S.G.	Volume (ft^3)	Mix Proportion-Mass Basis (%)	Mix Proportion-Volumetric Air-Free Basis (%)
Cement	9.2090	3.150	0.0469	17.4	13.2
Water	4.438	1.000	0.0711	8.4	20.0
Coarse Aggregate	24.160	2.662	0.1454	45.7	40.8
Fine Aggregate	14.561	2.629	0.0888	27.5	24.9
NaOH Admixture	0.535	2.131	0.0040	1.0	1.1
Total	52.903	-	0.3562	100.0	100.0

Table 4.3: Knife River aggregate properties

Knife River	S.G.	Unit Weight (lb/ft^3)	Absorption (%)
Coarse Aggregate	2.662	98.8	0.67
Fine Aggregate	2.629	-	0.91

A Type I ordinary Portland cement was used in the mix design and was generously provided by Holcim Cement. The cement was analyzed in accordance with the ASTM C114 and the cement alkaline content was measured as 0.509% Na_2O

equivalent. The ASTM C1293 specifies the use of cement having a minimum of 0.90% Na_2O equivalent. However, due to the nature of this test and material availability the lower cement alkaline content was considered reasonable.

Figure 4.7: Knife River aggregate and NaOH pellets

Table 4.4: Concrete aggregate size distribution

Aggregate	Size (U.S. Standard)	Percent Passing	Percent Retained	Cumulative Percent Retained
Coarse	3/4"	100	0	0
	1/2"	66.7	33.3	33.3
	3/8"	33.3	33.3	66.6
	1/4"	0	33.3	100
Fine	No. 4	100	0	0
	No. 8	90	10	10
	No. 16	75	15	25
	No. 30	40	35	60
	No. 50	20	20	80
	No. 100	0	20	100
	Pan	0	0	-

4.3.3 Casting and Instrumentation Program

Concrete used for casting specimens was mixed according to the ASTM C192. A mechanical pail batch mixer was used and the mixing procedure (based on ASTM C192 7.1.2 'Machine Mixing') can be summarized as the following:

1. Dissolve the NaOH pellets in the cool mixing water
2. Add some of the water and coarse aggregate prior to rotation of mixer
3. Start the mixer
4. Add the remaining coarse aggregate, fine aggregate, cement, and water
5. Continue mixing for 3 minutes after all materials have been incorporated
6. Stop the mixer for 3 minutes of rest and cover the opening with plastic
7. Uncover the opening and mix for an additional 2 minutes.
8. Place the mixture in a clean mixing pan.

After the mixture was moved to a clean mixing pan, fresh mixture characteristics and air content tests were performed. Concrete slump was measured per ASTM C143 and immediately following unit weight (bulk density) and yield tests were performed using ASTM C138 methodology. Air content was measured using the ASTM C231 pressure method. The fresh mix characteristics for both batches used in the casting of specimens is shown in Table 4.5. Figures 4.9, 4.10, 4.11 show slump, air content, and unit weight tests being conducted. After testing the concrete was returned to the mixing pan and specimens were cast according to ASTM C157 standards. A photograph of the prism molds is shown in Figure 4.21.

Table 4.5: Fresh mix characteristics

Mix	Slump (in)	Unit Weight (lb/ft^3)	Air Content (%)	Relative Yield
Batch 1	2.5	145.3	1.7	1.02
Batch 2	2.5	144.1	1.8	1.03

Figure 4.8: Slump test being performed

The casting of specimens consisted of filling each mold with concrete up to approximately ½ of its depth and tamping 25 times evenly across the cross-section of the mold and then slightly overfilling and tamping an additional 25 times evenly across the cross-section of the mold. The casting process is shown in Figure 1.

Figure 4.9: Air content test (pressure method)

Figure 4.10: Concrete unit weight test

Figure 4.11: 3 x 3 x 11.25 in. concrete prism molds

Figure 4.12: Casting of specimens

After the top layer was compacted excess concrete was struck off flush with the top surface of the mold and the top surface was trowel finished. The molds were covered with polyethylene plastic and allowed to set undisturbed for a 24 hour period. The freshly cast and finished Batch 1 specimens are shown in Figure 4.14.

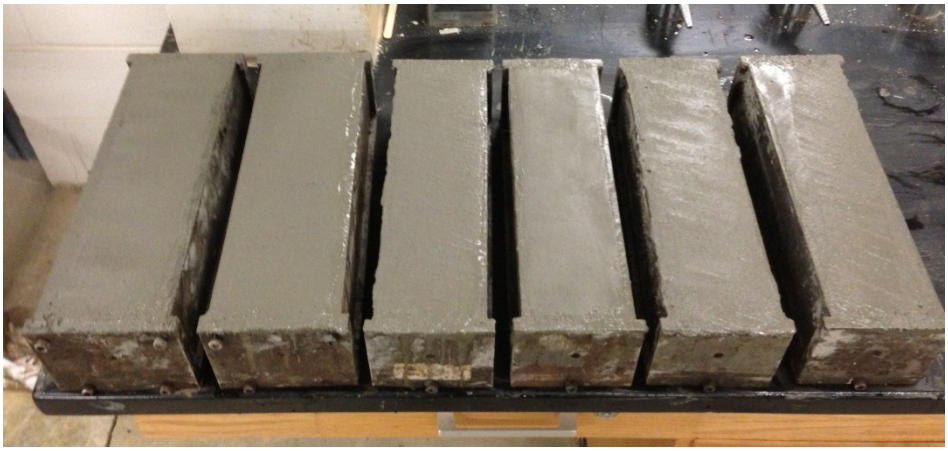

Figure 4.13: Batch 1 specimens just after casting

One batch of 6 specimens was cast and allowed to set for a 24 hour period. Immediately after 24 hours the first batch of specimens was demolded and initial comparatory length measurements were recorded. Acoustic emission sensors were then affixed to the specimens using a two part epoxy (ASTM E1316) and each specimen was subsequently placed in a container for storage. Once the first batch of specimens was properly stored acoustic emission data acquisition was started. Immediately after the first batch of specimens were stored and monitored, the second batch of specimens will be cast and handled using the same methodology as the first batch.

The surface of each specimen was lightly roughened, then cleaned, and the sensors were attached using a standard two part epoxy (ASTM E1316 2006). The sensors were affixed only to sides of the prisms that were in contact with the steel mold in order to promote a clean couple between the surface of the specimen and the AE sensor. The location of sensors on the test specimens is shown in Figure 4.15. However, after two weeks of testing the coupling between the sensors and some of the specimens was weakened due to the high temperature and humidity. Therefore, a two part epoxy manufactured specifically for these conditions was used to re-attach the sensors and no

subsequent coupling issues were encountered. The instrumented Batch 1 and Batch 2 specimens are shown in Figures 4.16 and 4.17.

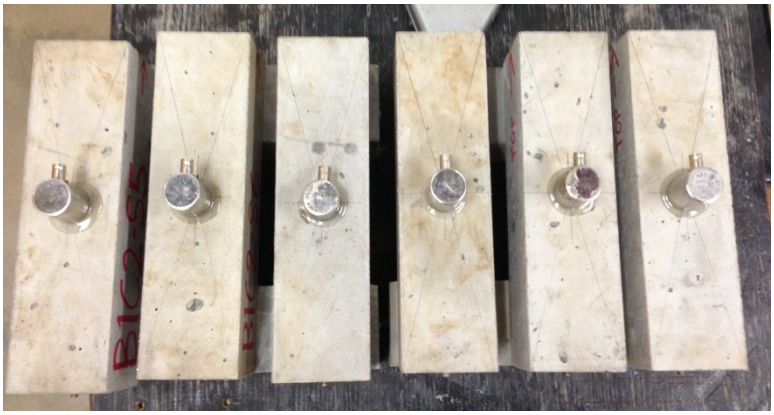

Figure 4.14: Location of sensors

The instrumented specimens were placed in each storage container immediately after the epoxy was allowed to set and cure. The coaxial sensor cables are fitted with a male-to-female connector which allows for the cables to be readily removed from the AE sensors. The specimens with cables attached in the storage containers are shown in Figure 4.18.

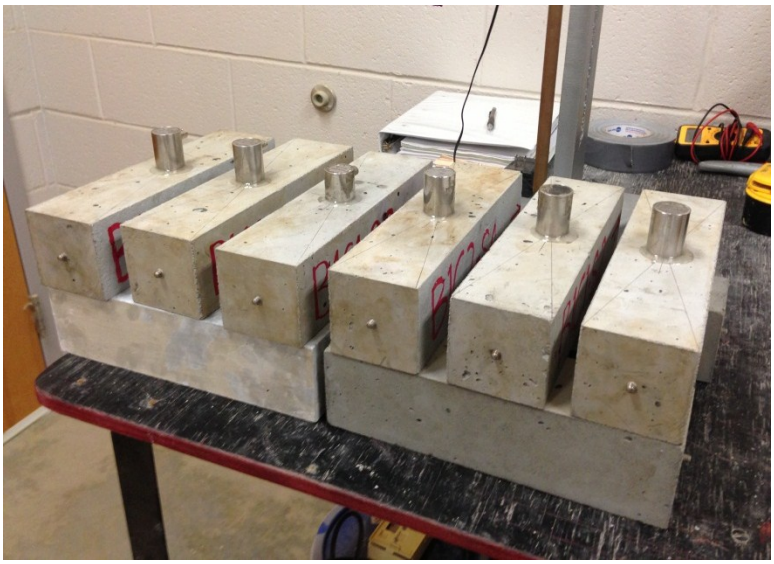

Figure 4.15: Batch 1 specimens with AE sensors attached

Figure 4.16: Batch 2 specimens with AE sensors attached

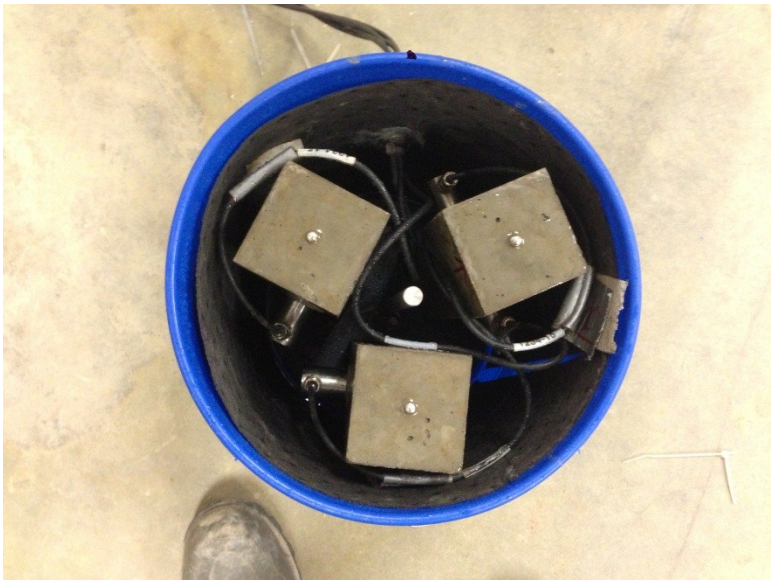

Figure 4.17: Instrumented specimens in storage container

4.3.4 Length Change Measurements

Length change measurements were taken at 1, 7, 10, 14, 21, 28, and 56 days using a Humboldt length comparator equipped with a digital display dial gauge. The length comparator is shown in Figure 4.19. Each time the specimens were removed for length

change measurements the AE data acquisition system was stopped before hand and then measurements were taken. Five readings were recorded for each specimen and the average of those readings was reported. After length change readings were recorded the specimens were returned to storage containers and pencil lead breaks were performed (ASTME1316) in order to ensure the AE sensors were still firmly coupled with the specimens. After pencil lead breaks were performed the containers and chamber were closed and the temperature was allowed to recover for a period of approximately one hour. This was done in order to minimize any noise in the AE data associated with thermal expansion of specimens or materials in contact with the specimens.

Figure 4.18: Length comparator

The subsequent comparator readings were compared to the initial comparator reading to determine the length change percentage. The comparator readings were taken per ASTM C157. The photograph in Figure 4.20 shows length change measurements

being recorded. However, due to the nature of this research program, specifically the AE instrumentation involved, the subsequent comparator readings were not taken in conformance with Section 10.2.2 of ASTM C1293. The process of soaking the specimens for 16 hours in a moist cabinet was omitted from the measurement procedure in order to minimize the time required to measure the specimens. This is an important consideration because AE data was not collected during the process of taking length change readings. The specimens were, therefore, removed from their storage containers and measured immediately for length change. The length change measurement procedure can be summarized as the follows:

1 Stop AE data acquisition

2 Open containment chamber

3 Open a storage container, remove a single specimen, replace container lid

4 Close containment chamber

5 Take length change readings

6 Place measured specimen aside, repeat steps 2-5 for all specimens in the batch

7 Return all specimens to storage containers

8 Perform pencil lead breaks

9 Replace container lids, close chamber, allow temperature to recover for 1 hr.

10 Restart AE data acquisition.

The concrete prisms are rotated in the comparator and a length change reading is taken while the specimen is spinning. The length change measurements are very small (on the order of 0.0001 in.) and it is imperative for the spinning procedure to be as consistent as possible. For this reason counter weights (Figure 4.23) of similar dimension

and weight were machined from stainless steel and affixed to the specimens. The counter weights were located opposite the position of the AE sensors, in order to balance the center of mass of the concrete prism. Erratic 'wobbling' of specimens during spinning and length change readings may result in noisy length change results.

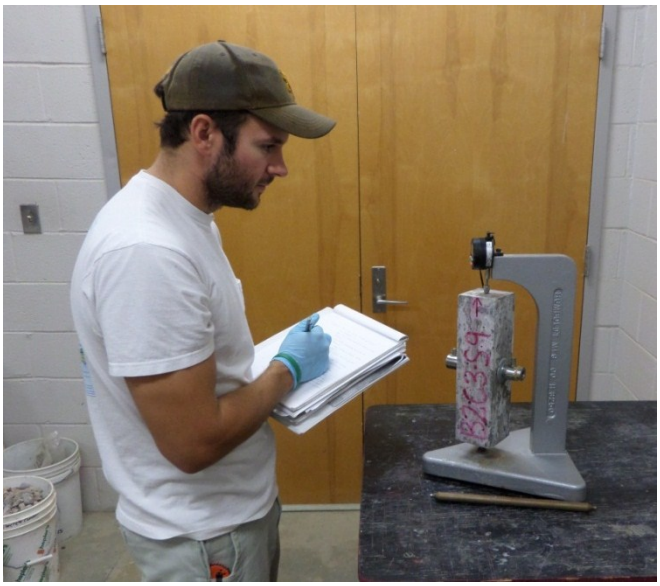

Figure 4.19: Length change measurements being recorded

. The ASTM C 1293 sets forth an expansion limit of 0.04% after one year of testing as the threshold for identifying an aggregate as potentially susceptible to deleterious ASR expansion. This criterion was used as a benchmark for the presence and extent of ASR damage occurring in each specimen.

4.3.5 Petrographic Examination

Three specimens were scheduled to be removed for petrographic examination after 14, 28, and 56 days in order to verify the presence of ASR in conjunction with length change measurement. These specimens were selected at random. Analysis of the specimens using petrographic microscopy is to be performed by Wiss, Janney, Elstner Associates Inc. (WJE) in Austin, TX. The results of the petrographic analysis have not

yet been reported on at the time of this thesis. The remaining three specimens are scheduled to be tested for a full year period and will be delivered to WJE for petrographic examination after testing is complete.

4.3.6 Acoustic Emission Monitoring

The Sensor Highway II System (SHII) manufactured by Mistras Group was used for continuous AE monitoring of the specimens. This system is equipped with 16 high-speed channels and 16 parametric input channels. It is rated for outdoor use and comes housed in a rugged weather proof enclosure. The SHII system is connected to a desk top computer and data collection and processing is achieved through Physical Acoustics Corporation's AEwin software. AEwin is a data acquisition and replay program capable of graphing identified hits/events and waveforms as well as source location and detailed event analysis. AEwin was used to process and filter AE data collected during experimentation. The data acquisition setup is shown in Figure 4.21.

All the specimens were instrumented with one 55 kHz resonant AE sensor having a 40 dB integral pre-amplification (R6i) placed at the centerline of the longitudinal face of the specimen. Four of the specimens were instrumented with an additional broadband AE sensor (WDi). Each storage container housed one specimen being monitored by both a R6i and a WDi sensor and the remaining two specimens being monitored with a R6i alone. Figure 4.22 shows schematic for AE sensor layout. An R6i sensor, WDi sensor, and sensor cable are shown in Figure 4.23.

The data collection threshold was set at 40 dB. AE data was recorded continuously during the test except for the short pauses where length measurements were taken.

Figure 4.20: R6i (right) and WDi (middle) sensors, sensor cable, and counter weight (left)

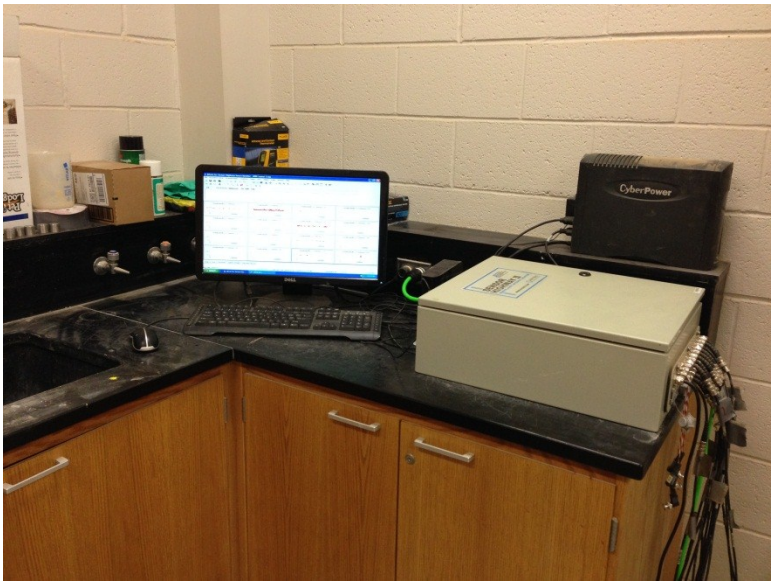

Figure 4.21: Data acquisition setup

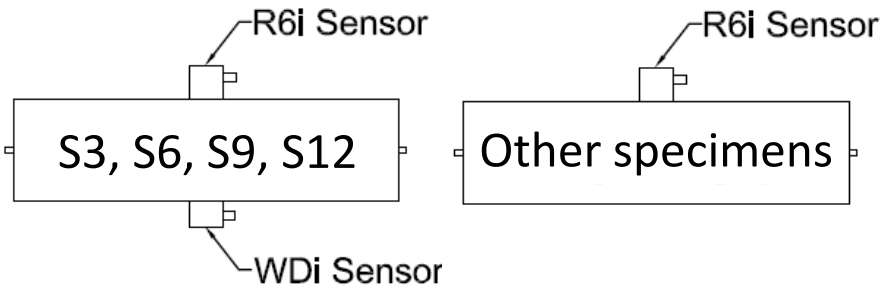

Figure 4.22: AE sensor schedule

4.3.7 Data Acquisition Schedule

The test setup includes petrographic analysis of the specimens periodically to serve as a benchmark for the progression and extent of ASR damage. Three specimens each were removed at 14, 28, and 56 days and shipped to WJE in Austin, TX for petrographic examination. A total of 9 specimens have been tested and sent for petrographic investigation. At the time of this thesis the remaining 3 specimens are still being tested along with the dummy specimens. The results of the petrographic analysis have not yet been reported. The results of petrography and length change and AE data for the 3 remaining test specimens, being monitored up to one year, will be reported on in the future.

4.4 RESULTS

This section discusses length change measurements and AE results for 5 ASR specimens as well as the 3 control specimens. Of the 5 ASR specimens discussed 2 were removed at 56 days for petrographic examination and the other 3 are still being tested but results up to 56 days for these specimens is presented. The control specimens were monitored for AE activity for a period of 42 days following the removal of the first 3 ASR specimens after 14 days of testing.

4.4.1 AE Data Filtering

Amplitude duration and signal strength parameters were used in AE data filtration and analysis. AE data filtering is an essential step to remove data not pertinent to the test. A baseline AE was recorded by placing AE sensors on control specimens to check the noise levels in the environmentally controlled chamber. This test showed that mechanical and electrical noise were generally minimal. Given the small cross-section of the specimens, and since no loading was applied, the irrelevant AE data will be primarily from wave reflections. Therefore, a duration-amplitude filter (D-A) was used to reject AE data related to reflection, also known as Swansong II filter. The filter was determined through visual inspection of AE waveforms. The filter limits are shown in Table 4.6.

Table 4.6: AE data rejection limits for D-A filter

Rejection Limits		Rejection Limits	
Amp (dB)	Duration (µs)	Amp (dB)	Duration (µs)
40-44	400	61-65	1,000
45-48	500	66-70	1,500
47-52	600	71-75	2,500
53-56	700	76-80	3,500
57-60	800	81-95	5,000

4.4.2 AE Results versus Length Change Measurements

The results of the filtered AE data in comparison with length change measurements are presented in this section. The initial comparator reading was considered as the zero point for length change measurement (approximately 24 hours after casting). A line is shown at day 14 on each plot showing AE and length change percentage results. This line marks the point at which the AE sensors were reattached to the specimens using epoxy

which is more suitable for high temperature and humidity conditions. The results from the filtered AE data collected from the 3 control specimens are also shown in this section for comparison with the test specimens. Control specimens D1, D2, and D3 were monitored for 42 days following the removal of the first 3 test specimens for petrographic analysis at day 14.

ASR specimen S3 is shown after 56 days of testing in Figure 4.23. No visible signs of cracking were observed on the surface of the specimen significant staining of the specimen was present. Figure 4.24 shows AE data in terms of amplitude and length change with respect to time for test specimen S3. The first length change reading at 1 day shows a decrease in the length of the specimen which is attributed to shrinkage. Following this measurement the length change steadily increases to a maximum value of 0.013% at 56 days (approximately 33% of the threshold specified by the ASTM C1293 for potentially deleterious aggregates after one year). A marked increase in AE activity can be seen after 14 days. This is due to the deterioration of the original epoxy during the first 14 days of testing which resulted in weakening of couple between the AE sensor and the specimen. The poor coupling attributed to the diminished sensitive of the AE sensors during the first 14 days.

Figure 4.23: Specimen S3 after 56 days of testing

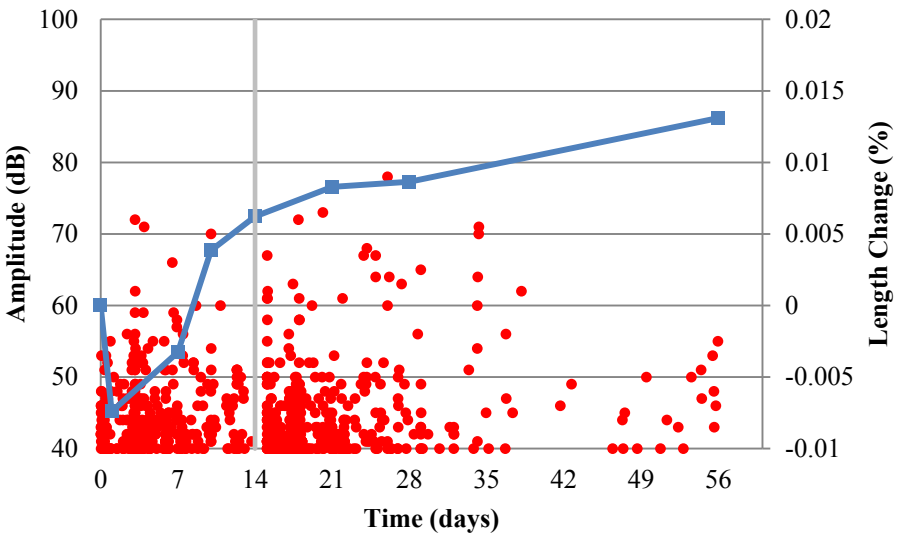

Figure 4.24: Specimen S3 - amplitude and length change versus time

Figure 4.25 shows the cumulative signal strength (CSS) of AE signals and length change with respect to time for specimen S3. CSS graphs are used to give a better indication regarding the degree of degradation in the structure. In this case, an increase in the CSS can be attributed to cracks forming as a result of ASR expansion. As seen in the figure, CSS did not increase significantly during the first 3 days of the test. A significant increase in the rate of CSS was then detected until 28 days. This increase matches the increase in the expansion detected from length change measurements. It is noted that AE has the ability to detect the formation of micro-cracks in real-time. In ASR tests, formations of cracks will precede significant changes in the length measurements; therefore, a behavior such as that shown in Figure 4.25 is expected (high rise in AE activity followed by expansion). The rate of CSS decreased afterwards indicating that fewer cracks are forming during this time (between 28 and 56 days). At the time of this thesis specimen S3 is still being monitored and is scheduled to be tested for a one year period.

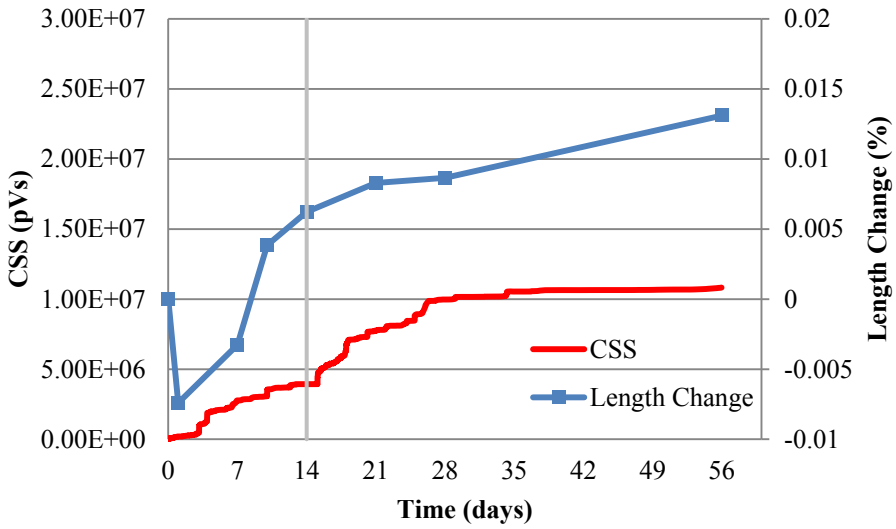

Figure 4.25: Specimen S3 - CSS and length change versus time

ASR specimen S5 is shown in Figure 4.26. The surface of the specimen was significantly stained. Figure 4.27 shows AE data, in terms of amplitude, and length change with respect to time for test specimen S5. Specimen S5 showed the highest amount of AE activity and as expected it also exhibited the largest expansion (0.019 %) of all the specimens monitored for 56 days. A small decrease in length is shown during the first week of testing this is potentially a result of operator error associated with length change measurement. Again a marked increase in AE activity can be observed after 14 days; this is attributed to the better coupling of the moisture resistant epoxy.

Figure 4.26: Specimen S5 after 56 days of testing

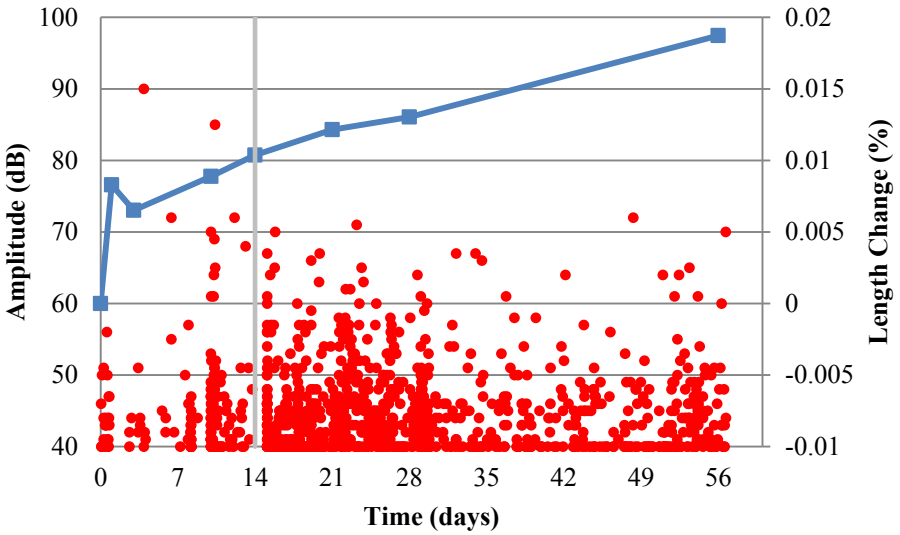

Figure 4.27: Specimen S5 - amplitude and length change versus time

Figure 4.28 shows the CSS of AE signals and length change with respect to time for specimen S5. CSS did not increase significantly during the first 4 days of the test. A relatively steady increase in the rate of CSS was then detected until around up to 56 days. This increase matches well with the increase in the expansion detected from length change measurements. Specimen S5 shows a substantial amount of AE activity continuing to occur up to the 56 day point which indicates that a significant amount of ASR related cracking continues to occur also. This is expected as the rate of length increase steadily increases after the first week up to 56 days. A marked spike in CSS can be observed around day 4 of testing. This increase corresponds well with expansion shown in length change measurements and is attributed to the beginning of significant crack nucleation due to ASR. In general CSS agrees well with measured length change. This indicates that expansive crack formation is captured effectively by acoustic emission. Specimen S5 shows continued AE activity after 56 days. At the time of this thesis Specimen S5 is still being monitored and is scheduled to be tested for a one year period.

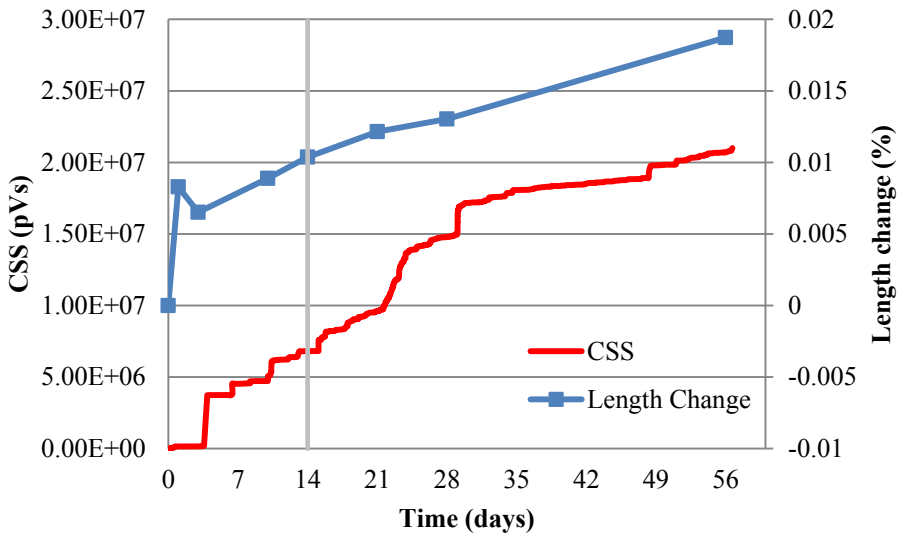

Figure 4.28: Specimen S5 – CSS and length change versus time

ASR specimen S6 shown in Figure 4.29 also showed deep staining at the surface. Figure 4.30 shows amplitude and length change with respect to time for test specimen S6. Specimen S6 showed an expansion of 0.008% after 56 days of testing. Although this expansion is slightly less than that of the other test specimens it still accounts for 20% of the 0.04% limit, specified by ASTM C1293 at one year, after only 2 months of testing. Decreases in length were measured in two instances and these are perceived to be related to operator error associated with the length comparator readings. A poor coupling due to the deterioration of the first epoxy used to attach the AE sensors resulted in very little AE hits occurring during the first 14 days of testing.

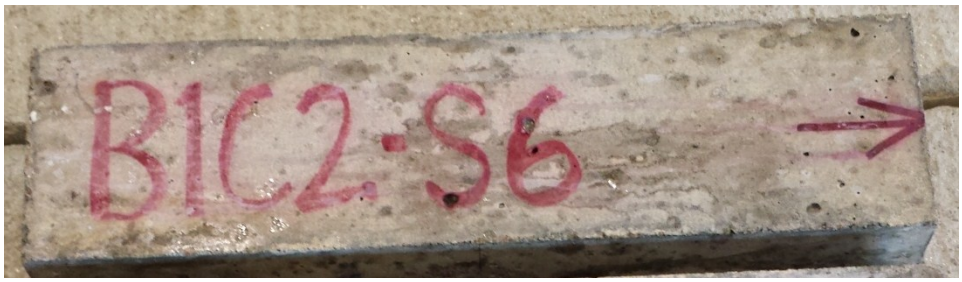

Figure 4.29: Specimen S6 after 56 days of testing

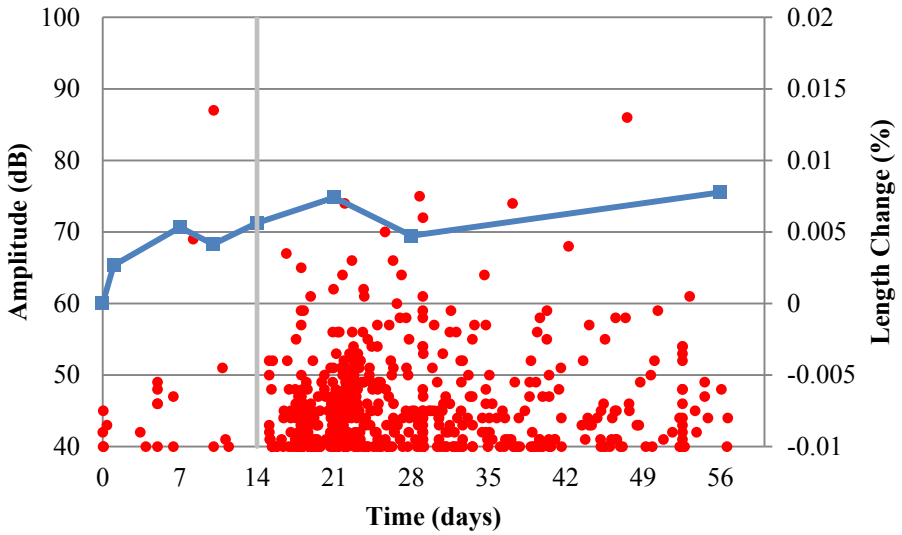

Figure 4.30: Specimen S6 – amplitude and length change versus time

Figure 4.31 shows the CSS of AE signals and length change with respect to time for specimen S6. A clear and steady increase in in CSS is observed after 14 days up to day 56 of testing. Other than a spike around day 10 very little AE is observed in the first 14 days of testing. The sharp rise in CSS at day 10 is considered noise resulting from the deterioration of the original epoxy used to attach the AE sensors. In general the trend in CSS agrees well with length change measurements.

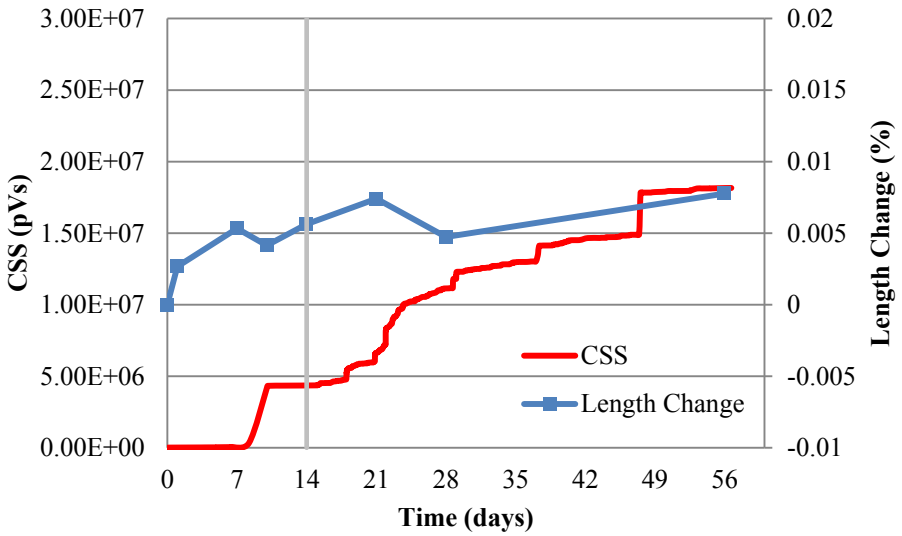

Figure 4.31: Specimen S6 – CSS and length change versus time

ASR specimen S10 after 56 days of testing is shown in Figure 4.32. As with other ASR specimens S10 showed marked staining at the surface. Amplitude and length change with respect to time is shown in Figure 4.33. Specimen S10 increased in length by 0.012% at 56 days. Due to the weakened couple between the AE sensor and the specimen a limited number of AE hits were recorded during the first 14 days of testing. However, from 14 days up to day 56 a significant number of events were recorded. Some decreases in length were measured on days 10 and 21. These decreases are small (less than .0025%) and are attributed to operator error associated with the length comparator. In general the length change measurements agree well with the AE data. Specimen S10 remained very active up to day 56 and is scheduled to be monitored for a one year period.

Figure 4.32: Specimen S10 after 56 days of testing

Figure 4.34 shows the CSS of AE signals and length change with respect to time for specimen S10. A steady increase in CSS is shown from day 14 up to day 56 which corresponds with the steady increase in length that was measured. As crack formation progresses both expansion and CSS are expected to increase which is the case for specimen S10. Again, very little CSS due to AE activity was observed during the first 14 days of testing. This is attributed to the deterioration of the first epoxy used to attach AE sensors which compromised the couple between the sensor and specimen.

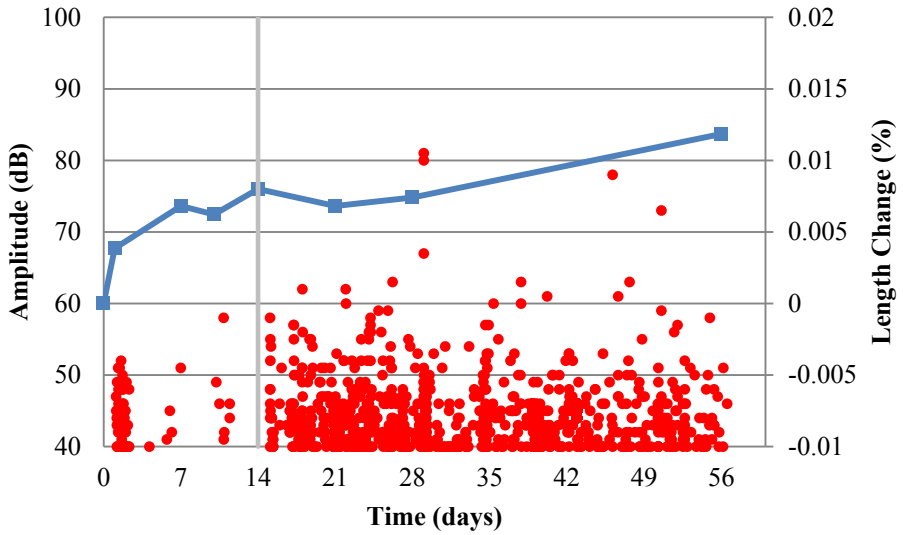

Figure 4.33: Specimen S10 – amplitude and length change versus time

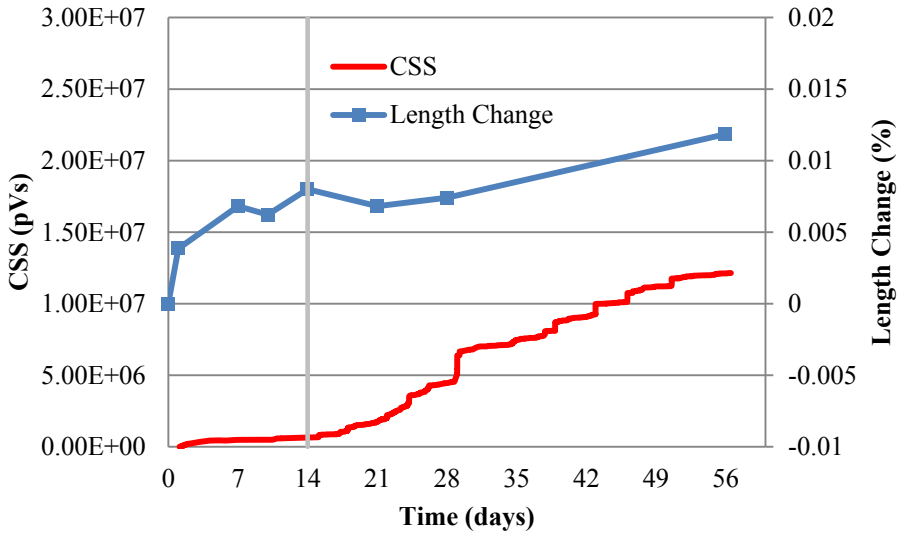

Figure 4.34: Specimen 10 – CSS and length change versus time

ASR specimen S12 is shown Figure 4.35. Like the other test specimens significant staining was present on the surface of the specimen S12. Figure 4.36 shows amplitude and length change with respect to time for test specimen S12. An expansion of 0.010% was measured for specimen S12 (25% of threshold ASTM C1293 for deleterious aggregates) after 56 days of testing. Some decrease in length was measured during the

first week and this is attributed to shrinkage. Overall a general trend of increasing length was observed which corresponds well with AE activity. Like the other specimens a limited amount of AE was collected during the first 14 days due to the problems associated with the deterioration of epoxy used to attach the AE sensors to the specimens. The figure shows that a decrease of AE activity was detected towards the end of the test. This was attributed to a dominant period in crack growth which follows the formation of the initial cracks within the aggregates and the formation of expansive ASR gel.

Figure 4.35: Specimen S12 after 56 days of testing

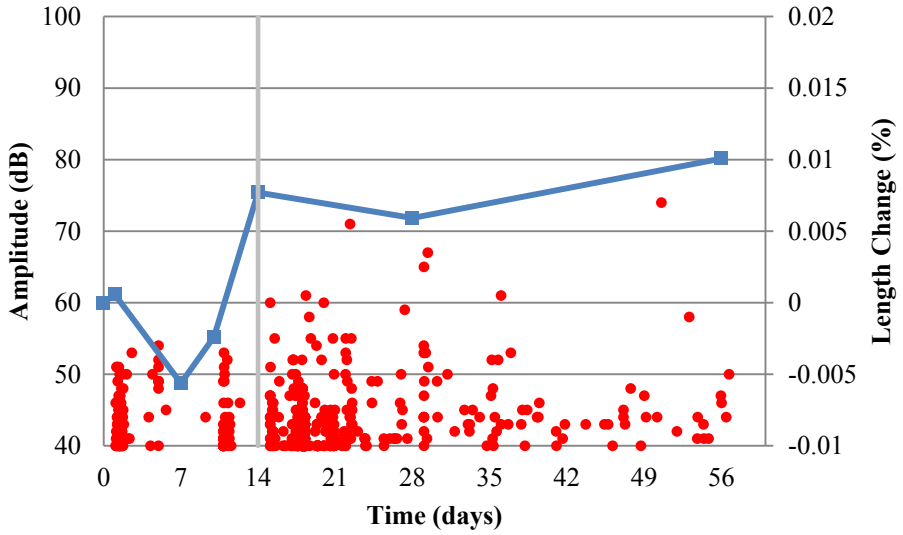

Figure 4.36: Specimen 12 – amplitude and length change versus time

Figure 4.37 shows the CSS of AE signals and length change with respect to time for specimen S12. In general a trend of increasing CSS corresponds with the overall increase in length that was measured for the specimen. A small decrease in length was measured at day 28. This is attributed to operator error associated with the length comparator readings.

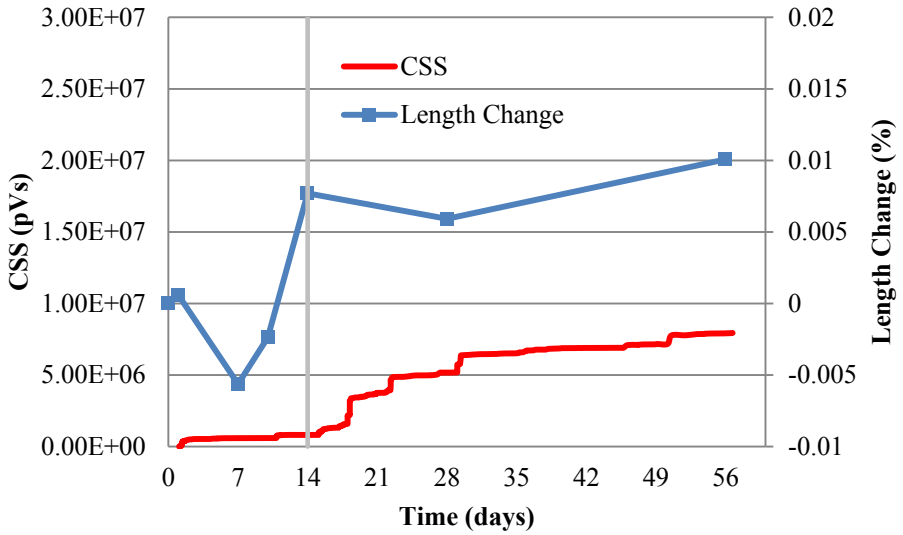

Figure 4.37: Specimen 12 – CSS and length change versus time

Control specimen D1 is shown in Figure 4.38 after 42 days of testing. No staining appeared on at the surface of the specimen as with the ASR specimens. Figure 4.39 shows amplitude with respect to time for control specimen D1. The figure shows that very little AE hits were recorded for control specimen D1 in comparison with all of the other test specimens. It should be noted that, due to the highly sensitive nature of AE, even with proper filtering techniques it is impossible to remove all noise and nonrelevant information from the AE data set. The hits shown in Figure 4.39 are either caused by noise or are a result of phenomena unrelated to ASR induced expansion and cracking.

This is confirmed through inspection of the individual waveforms associated with each hit on the control specimen.

Figure 4.38: Control specimen D1 after 42 days of testing

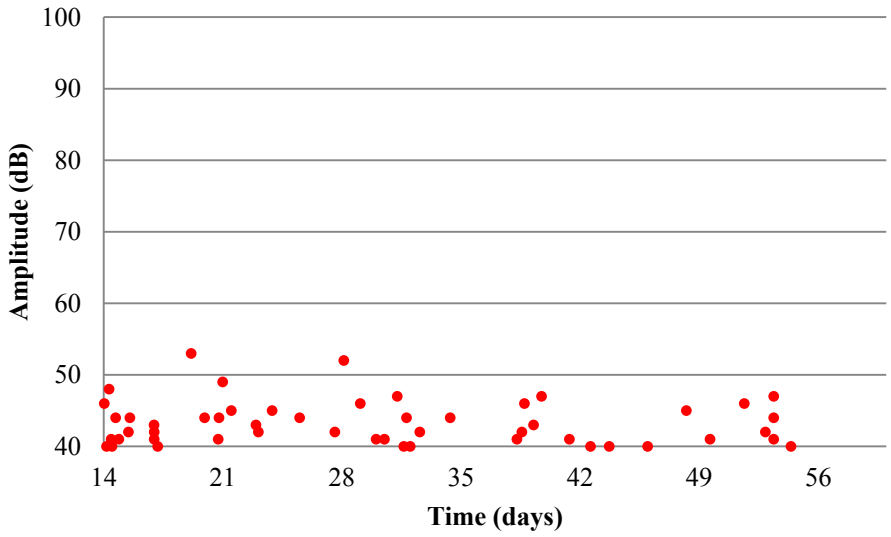

Figure 4.39: Control specimen D1 – amplitude versus time

Figure 4.40 shows the CSS of AE signals with respect to time for control specimen D1. The figure shows that the increase in CSS during the 42 days AE data was collected was negligible. The minimal amount of hits recorded and the resulting insignificant CSS for control specimen D1 can be attributed to the fact that no crack formation is occurring within the specimens due to ASR.

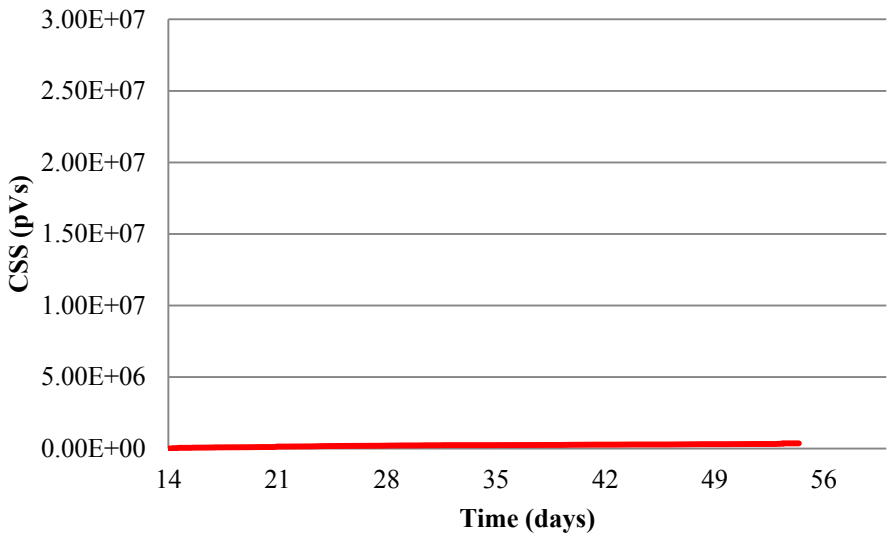

Figure 4.40: Control specimen D1 – CSS versus time

Control specimen D2 is shown in Figure 4.41. No staining was observed on the surface of the specimen. Figure 4.42 shows the amplitude with respect to time for control specimen D2. The figure shows that in general the number of AE hits recorded was much less than that of the ASR specimens. The majority of the AE hits occur during the first 28 days of monitoring. Inspection of the AE waveforms associated with the individual hits confirms that these signals are primarily a result of noise or other mechanisms that are unrelated to ASR deterioration.

Figure 4.41: Control specimen D2 after 42 days of testing

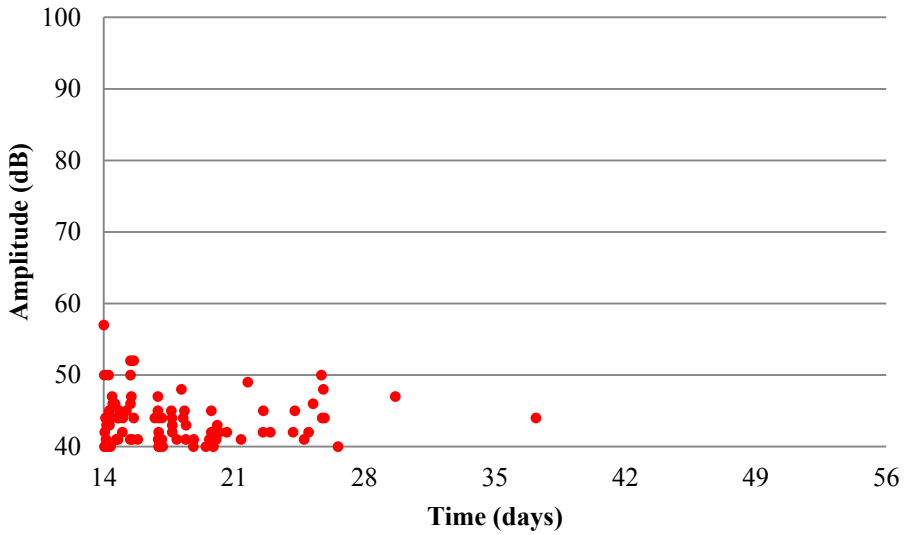

Figure 4.42: Control specimen D2 – amplitude versus time

Figure 4.43 shows the CSS of AE signals with respect to time for control specimen D2. The figure shows that CSS is negligible compared to the ASR specimens. After day 28 CSS is essentially constant. This indicates that no cracking or release of energy is occurring within the specimen related to ASR. This behavior is expected because the control specimens contain low-alkaline cement and innocuous aggregates.

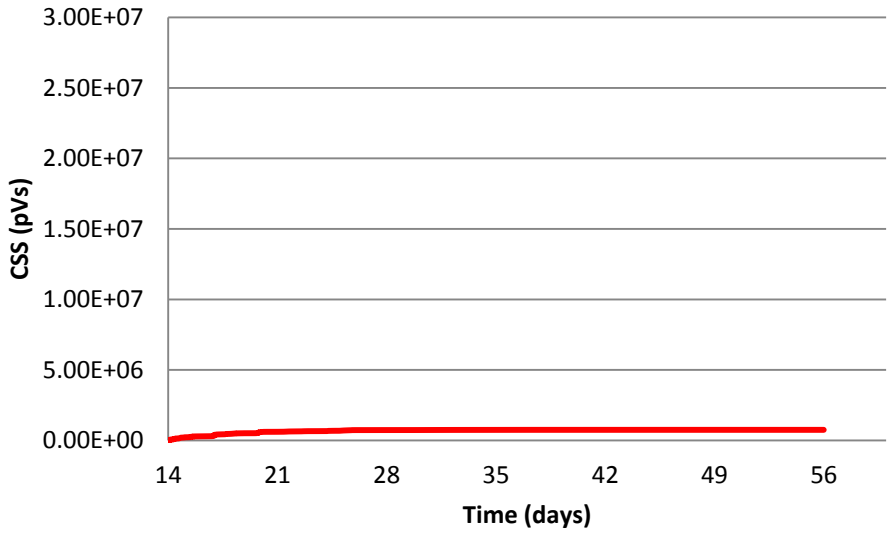

Figure 4.43: Control specimen D2 – CSS versus time

Control specimen D3 is shown in Figure 4.44. The specimen showed no staining on the surface. Figure shows the amplitude with respect to time for control specimen D3. The number of hits shown in the figure is much less than that of the test specimens. Inspection of the waveforms associated with these hits indicates that they are primarily caused by noise or irrelevant sources.

Figure 4.44: Control specimen D3 after 42 days of testing.

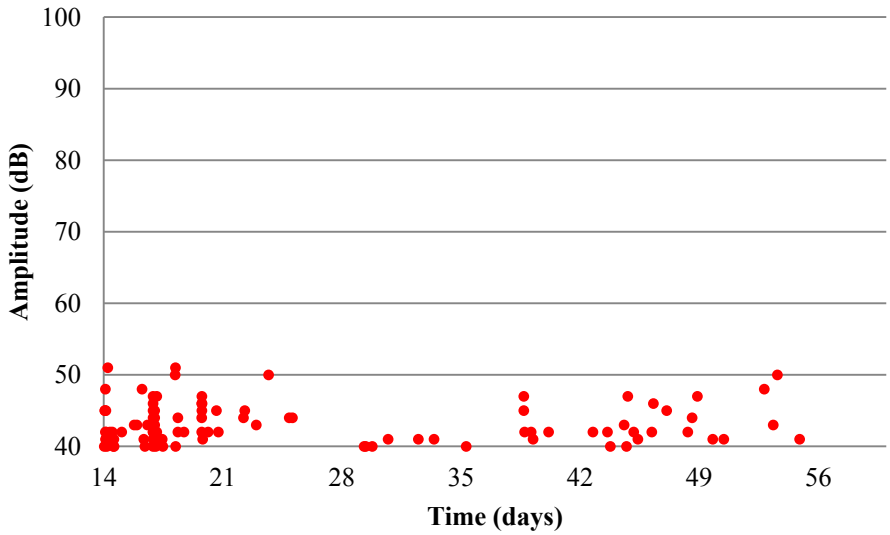

Figure 4.45: Control specimen D3 – amplitude versus time

Figure 4.46 shows the CSS of AE signals with respect to time for control specimen D3. The figure shows that control specimen D3 experienced a negligible increase in CSS during monitoring. Like the other dummy specimens this behavior is

expected for innocuous behavior of the aggregates. The insignificant level of AE activity indicates that no ASR induced expansive cracking is occurring in the specimen.

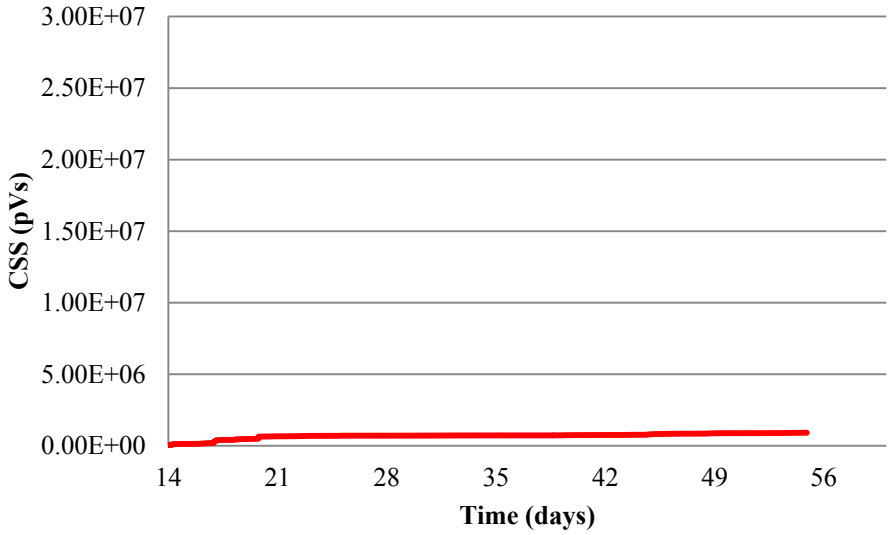

Figure 4.46: Dummy specimen D3 – CSS versus time

A summary of the maximum length change of each of the ASR specimens along with maximum CSS value (test and dummy specimens) is reported in Table 4.7. Length change at 56 days of the ASR specimens ranges from 0.008% to 0.019%. After 56 days of testing, length change values range from around 20% to 50% of the limit value (after one year of testing) specified by ASTM C1293 for identifying aggregates as potentially deleterious. S6 has the least length change percentage and specimen S12 has the least CSS value. In general the value of length change percentage and CSS are comparable between the test specimens. The control specimens were not measured for length change but they contain cement and aggregates that are known to behave innocuously and therefore negligible length change is anticipated for these specimens. The CSS values for the control specimens are in general 2 orders of magnitude less than that of the test specimens. This illustrates the potential of CSS as an indication of ASR damage. However, CSS can

only be used as an indication based on the rate of change because assigning numerical values with such parameters will be highly influenced by the specimen size and AE attenuation, which changes even in very similar specimens.

Table 4.7: Length change measurements and AE data

Specimen Number	Length Change (%)	Cumulative Signal Strength (pVs)
S3	0.013	$1.08x10^7$
S5	0.019	$2.10x10^7$
S6	0.008	$1.82x10^7$
S10	0.012	$1.21x10^7$
S12	0.010	$7.94x10^6$
Dummy 1	-	$3.68x10^5$
Dummy 2	-	$7.52x10^5$
Dummy 3	-	$9.13x10^5$

4.4.3 AE Intensity Analysis versus Length Change Measurements

AE intensity analysis was used to provide a better assessment of ASR damage. This approach was initially developed to assess damage in fiber reinforced polymer vessels (Fowler et al 1989). Recently, intensity analysis was used to quantify damage mechanisms in quantify concrete structures such as corrosion (ElBatanouny et al. 2011). The method uses the signal strength (SS) to calculate two parameters; historic index and severity. Historic index, $H(t)$, estimates the change in the slope of the CSS in historic approach while severity, S_r, is the average signal strength of the largest 50 hits. Historic index and severity can be calculated using Eq. (1) and Eq. (2) where: N is number of hits up to a time (t), S_{oi} is the signal strength of the *i-th* event, and K is empirically derived factor that varies with number of hits. In this study, the value of K was selected to be: a)

N/A if $N \leq 50$, b) $K=N-30$ if $51 \leq N \leq 200$, c) $K=0.85N$ if $201 \leq N \leq 500$, and d) $K=N-75$ if $N \geq 501$.

$$H(t) = \frac{N}{N-K} \frac{\sum_{i=K+1}^{N} S_{oi}}{\sum_{i=1}^{N} S_{oi}} \quad (1)$$

$$S_r = \frac{1}{50} \sum_{i=1}^{i=50} S_{oi} \quad (2)$$

The intensity analysis chart is obtained by plotting the maximum severity and historic index acquired during the test where the points plotted to the top-right corner of the figure indicates more damage. Figure 4.47 shows the intensity analysis results for the ASR specimens (length change % on each data point) and the 3 control specimens. As seen in the figure, the control specimen data plots towards the bottom-left corner of the figure while the data from the ASR specimens plot towards the top-right corner. With more data, empirical boundaries classifying ASR damage levels can be established which enables the quantification of this damage mechanism in similar specimens.

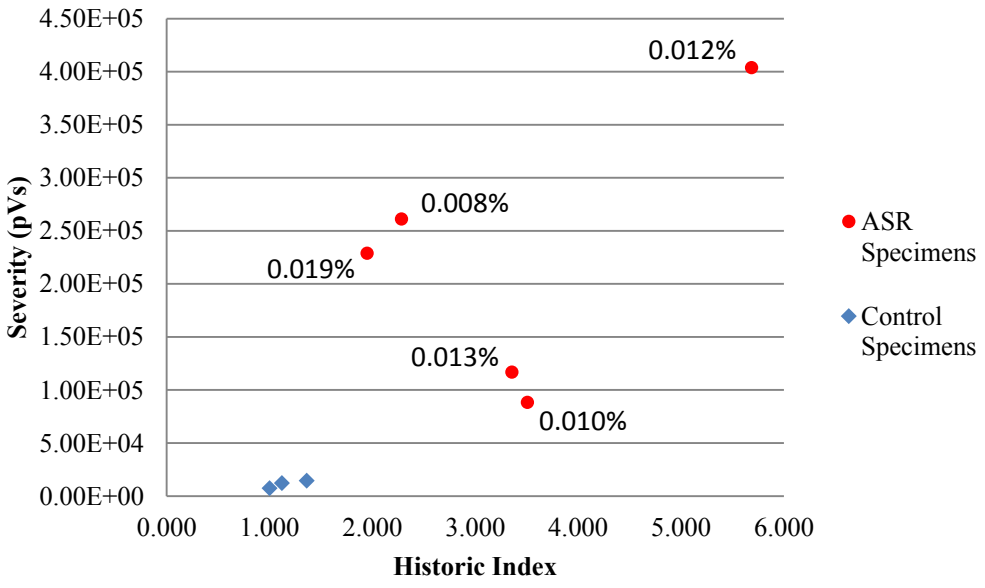

Figure 4.47: Intensity analysis

4.5 SUMMARY AND CONCLUSIONS

An accelerated alkali-silica reaction (ASR) test was designed to examine the ability of acoustic emission (AE) to detect this damage mechanism. ASR is a chemical reaction occurring between alkaline hydroxides from the cement past and certain types of amorphous silica within mineral aggregates. ASR causes an accumulation of internal pressure due to the formation of an expansive gel which leads to swelling and cracking of concrete. AE is highly sensitive to stress waves emitted from sudden release of energy, such as formation of cracks in concrete. This allows it to capture and identify propagating damage. AE has the potential to detect micro-cracks forming prior to expansion, which can be related to the degree of ASR damage.

The experimental setup consisted of an adapted ASTM C1293 test, twelve specimens of dimensions 3x3x11.25 in. created using a highly reactive aggregate as well as an elevated alkaline content, and 3 control specimens of similar dimensions incorporating innocuous aggregates and low-alkaline cement. The specimens were placed in controlled environment with high temperature and relative humidity to accelerate the ASR reaction. Length change measurements and petrographic examination were performed periodically to detect ASR damage while AE activity was recorded continuously.

The results of this study show that AE is able to detect ASR damage with a good agreement with length change measurements. The specimens containing reactive aggregate, along with elevated alkalinity show a general trend of increasing length which indicates the presence of ASR damage. The results of petrographic analysis have not yet been reported on, however, significant staining was observed on the surface of the ASR

affected specimens. Staining and discoloration is often a precursor for ASR induced crack formation at the surface. AE cumulative signal strength also corresponded well with the length change associated with ASR damage. An AE intensity analysis was performed using severity and historic index parameters. The ASR distressed specimens plotted in the higher damage regions of the intensity analysis chart which demonstrates its viability for classification of ASR damage. This research program is ongoing and with the progress of testing, more data will be available which may help in the determination of damage level boundaries.

This study is intended to determine the feasibility of AE for condition assessment of structures subject to ASR deterioration. A more thorough investigation is needed to establish how AE parameters might be used to develop algorithms which can predict the degree of ASR damage that has occurred over a period of time. It is also important for the ASR damage assessment program to have the capability of distinguishing AE related to ASR distress as opposed to other mechanisms such as loading or thermal expansion/contraction.

4.6 REFERENCES

ASTM C1293. 2008. Standard Test Method for Determination of Length Change of Concrete Due to Alkali-Silica Reaction. American Standard for Testing and Materials, 1-7.

Swamy, R.N. 1998: The Alkali-Silica Reaction in Concrete. New York, Blackie and Son Ltd.

ASTM C 1260-07. 2007. Potential Alkali Reactivity of Aggregate (Mortar-Bar Method). American Society for Testing Materials, Philadelphia, 652-655.

Ziehl, P. 2008. Applications of Acoustic Emission Evaluation for Civil Infrastructure. SPIE Proc. SPIE Smart Structures NDE, San Diego, CA, 9.

Pollock, A.A. 1986. Classical Wave Theory in Practical AE Testing. Progress in AE III, Proceedings of the 8th International AE Symposium, Japanese Society for Nondestructive Testing, 708-721.

ElBatanouny, M.K, Larosche, A., Mazzoleni, P., Ziehl, P.H, Matta, F., and Zappa, E. 2012. Identification of Cracking Mechanisms in Scaled FRP Reinforced Concrete Beams using Acoustic Emission. Experimental Mechanics, DOI 10.1007/s11340-012-9692-3, November (online).

Mangual, J., ElBatanouny, M. K., Ziehl, P., and Matta, F. 2013. Acoustic-Emission-Based Characterization of Corrosion Damage in Cracked Concrete with Prestressing Strand. ACI Materials Journal, 110(1), 89.

Idrissi, H., and Limam, A. 2003. Study and characterization by acoustic emission and electrochemical measurements of concrete deterioration caused by reinforcement steel corrosion. NDT & E International, 36(8), 563-569.

Assouli, B., Simescu, F., Debicki, G., and Idrissi, H. 2005. Detection and identification of concrete cracking during corrosion of reinforced concrete by acoustic emission coupled to the electrochemical techniques. NDT & E International, 38(8), 682-689.

ASTM C157 / C157M – 08. 2008. Standard Test Method for Length Change of Hardened Hydraulic-Cement Mortar and Concrete. American Society for Testing and Materials, 1-5.

ASTM C29 / C29M – 09. 2009. Standard Test Method for Bulk Density ("Unit Weight") and Voids in Aggregate. American Society for Testing and Materials, 1-13.

ASTM C114 – 13. 2013. Standard Test Methods for Chemical Analysis of Hydraulic Cement. American Society for Testing and Materials, 1-16.

ASTM C192 / C192M - 13a. 2013. Standard Practice for Making and Curing Concrete Test Specimens in the Laboratory. American Society for Testing and Materials, 7-20.

ASTM C138 / C138M - 13a. 2013. Standard Test Method for Density (Unit Weight), Yield, and Air Content (Gravimetric) of Concrete. American Society for Testing and Materials, 1-9.

ASTM C231 / C231M – 10. 2010. Standard Test Method for Air Content of Freshly Mixed Concrete by the Pressure Method. American Society for Testing and Materials, 1-9.

ASTM E1316. 2006. Standard Terminology for Nondestructive Examinations. American

Society for Testing and Materials, 1-33.

Fowler, T., Blessing, J., and Conlisk, P. 1989. New Directions in Testing. Proc. 3rd International Symposium on AE from Composite Materials, Paris, France.

ElBatanouny, M., Mangual, J., Ziehl, P., and Matta, F. 2011. Corrosion Intensity Classification in Prestressed Concrete using Acoustic Emission Technique. Proc. American Society for Nondestructive Testing (ASNT) Fall Conference and Quality Testing Show 2011, Palm Springs, CA. October 24-28, 10.

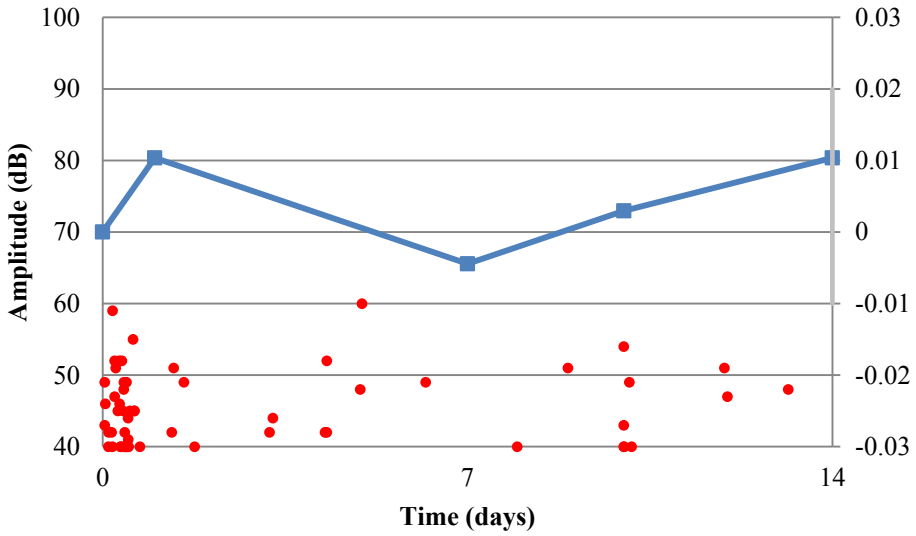

Figure 4.48: Specimen S1 (tested 14 days) – amplitude versus time

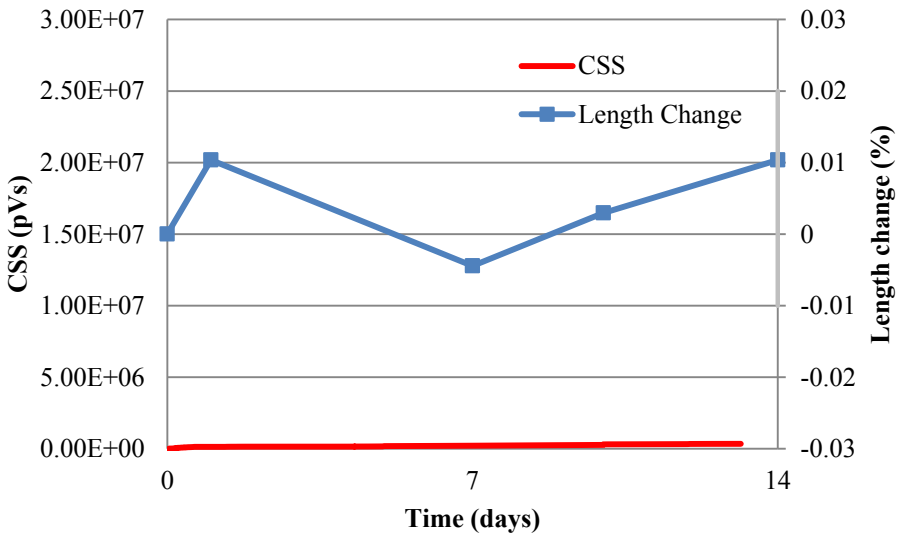

Figure 4.49: Specimen S1 (tested 14 days) – CSS versus time

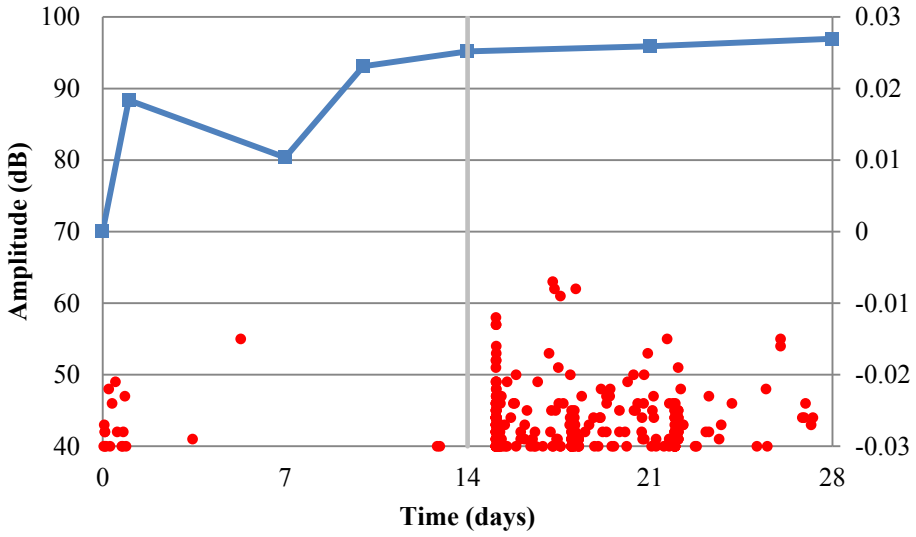

Figure 4.50: Specimen S2 (tested 28 days) – amplitude versus time

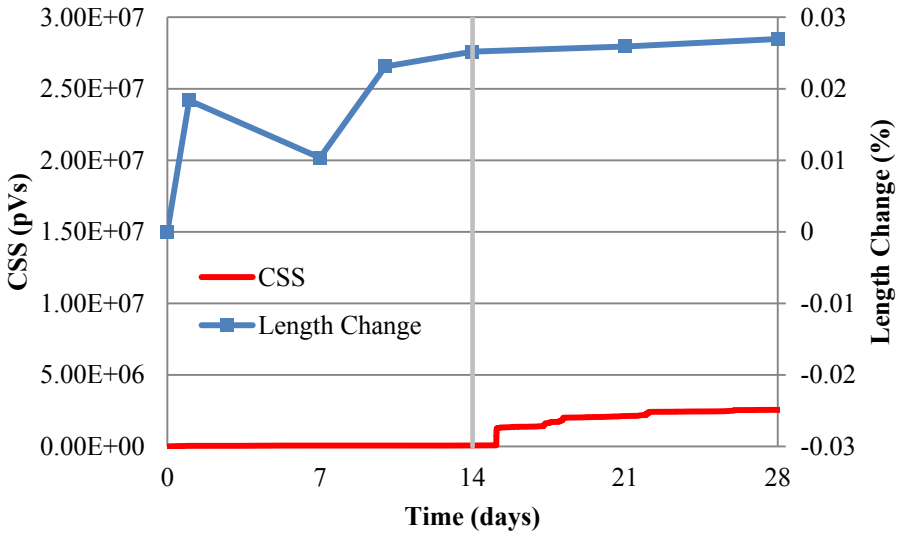

Figure 4.51: Specimen S2 (tested 28 days) – CSS versus time

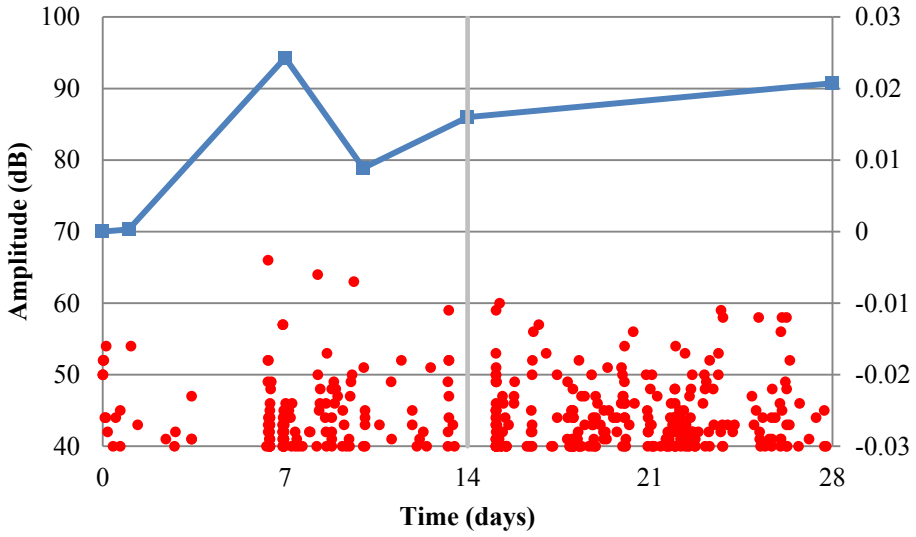

Figure 4.52: Specimen S4 (tested 28 days) – amplitude versus time

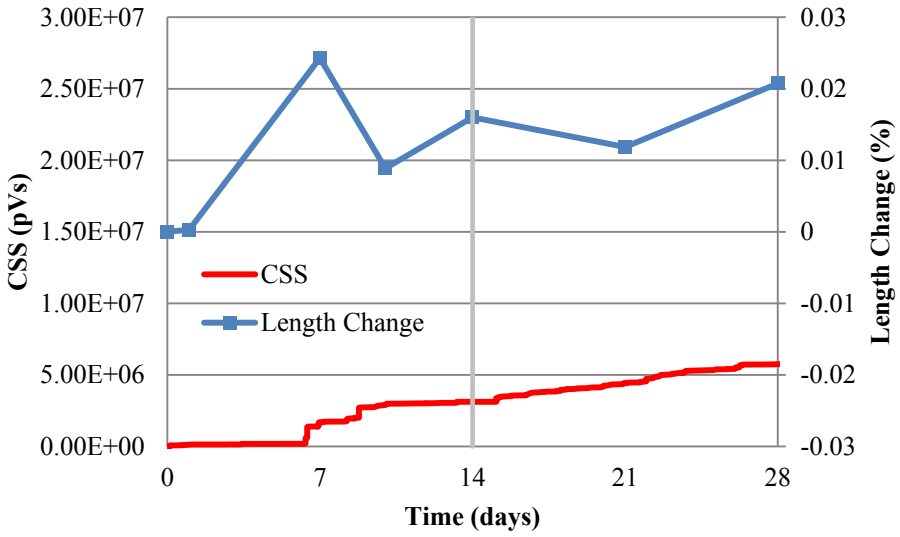

Figure 4.53: Specimen S4 (tested 28 days) – CSS versus time

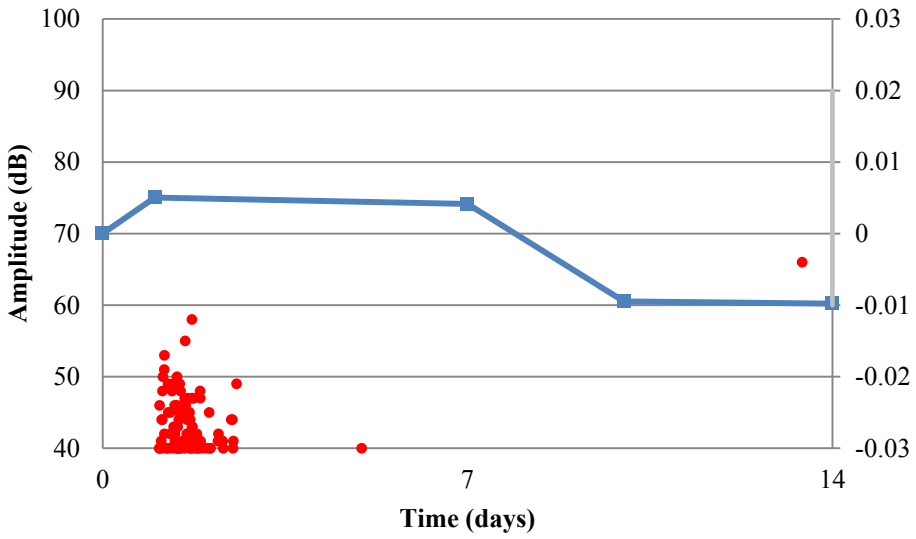

Figure 4.54: Specimen S7 (tested 14 days) – amplitude versus time

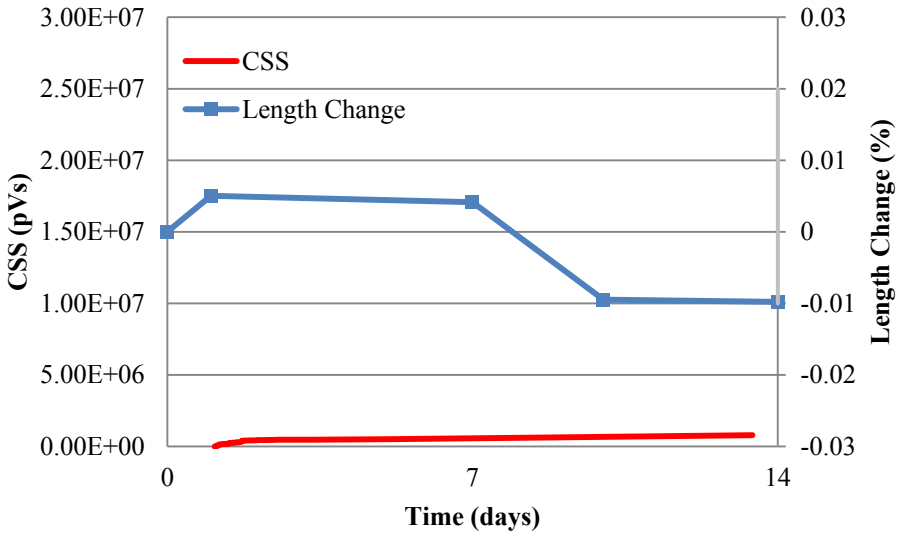

Figure 4.55: Specimen S7 (tested 14 days) – CSS versus time

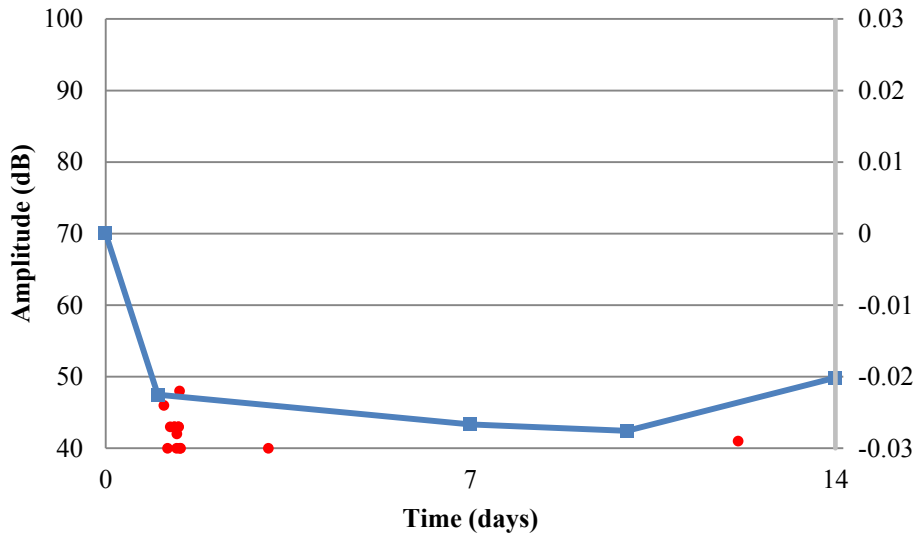

Figure 4.56: Specimen S8 (tested 14 days) – amplitude versus time

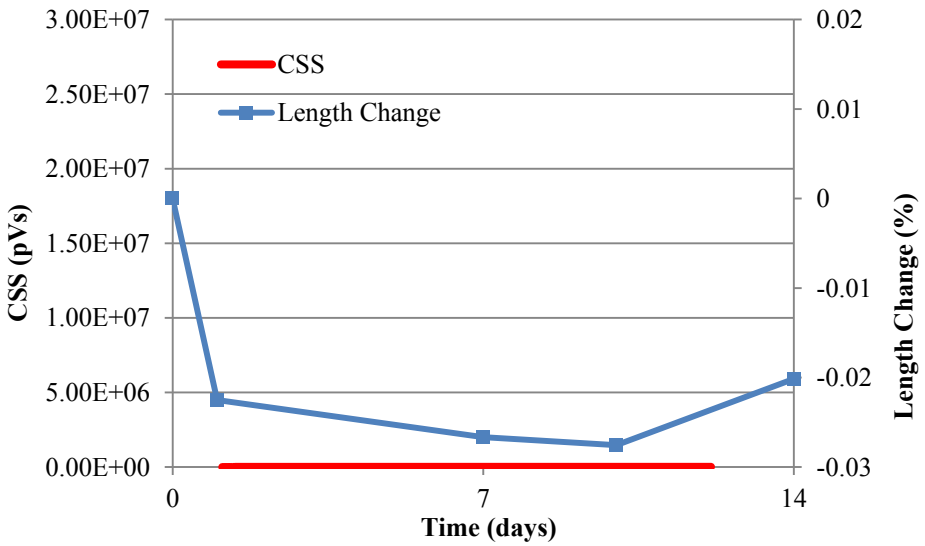

Figure 4.57: Specimen S8 (tested 14 days) – CSS versus time

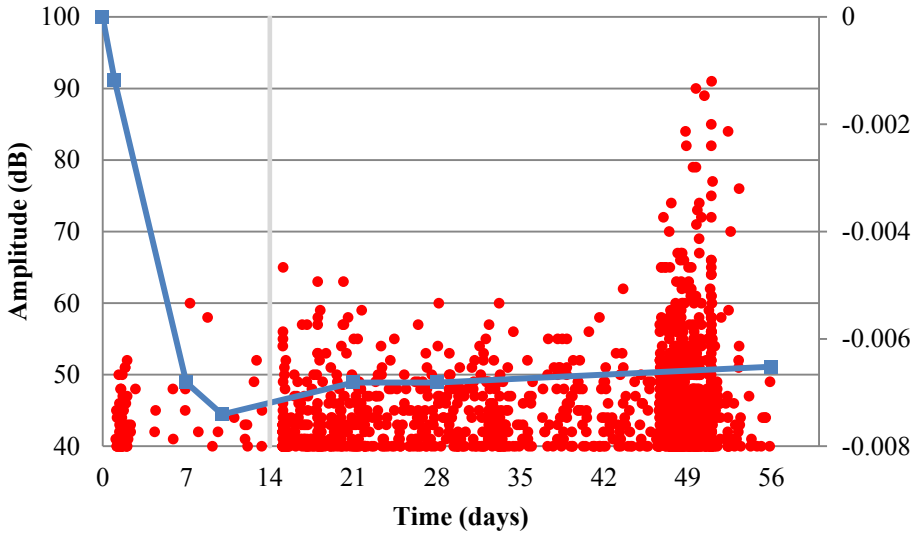

Figure 4.58: Specimen S9 (tested 56 days) – amplitude versus time

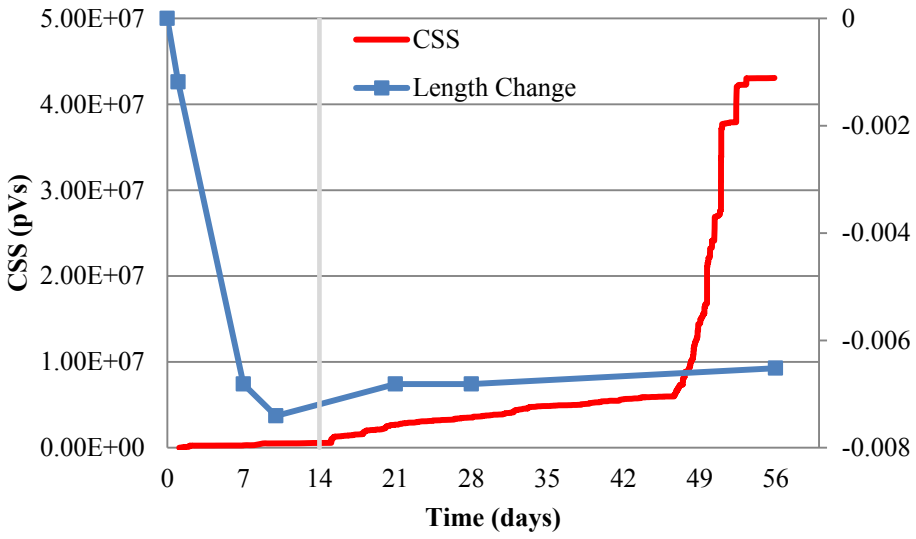

Figure 4.59: Specimen S9 (tested 56 days) – CSS versus time

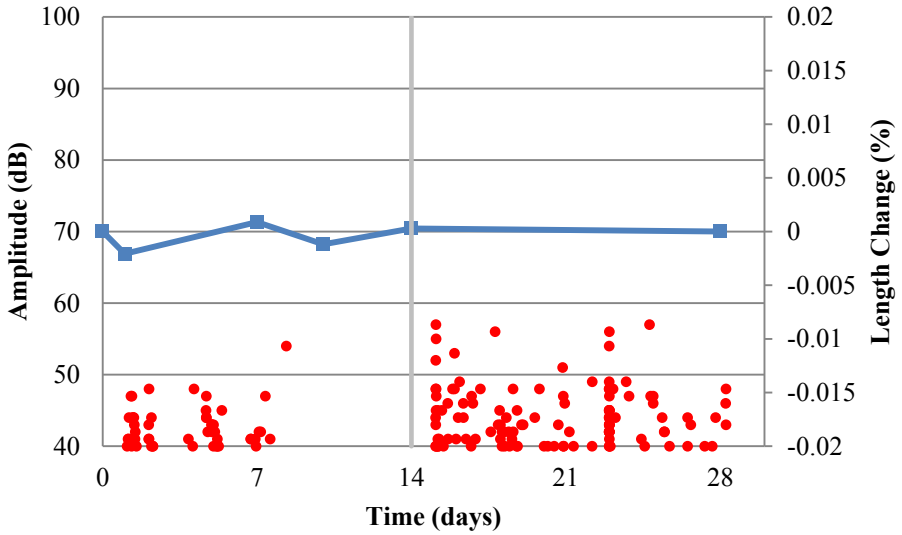

Figure 4.60: Specimen S11 (tested 28 days) – amplitude versus time

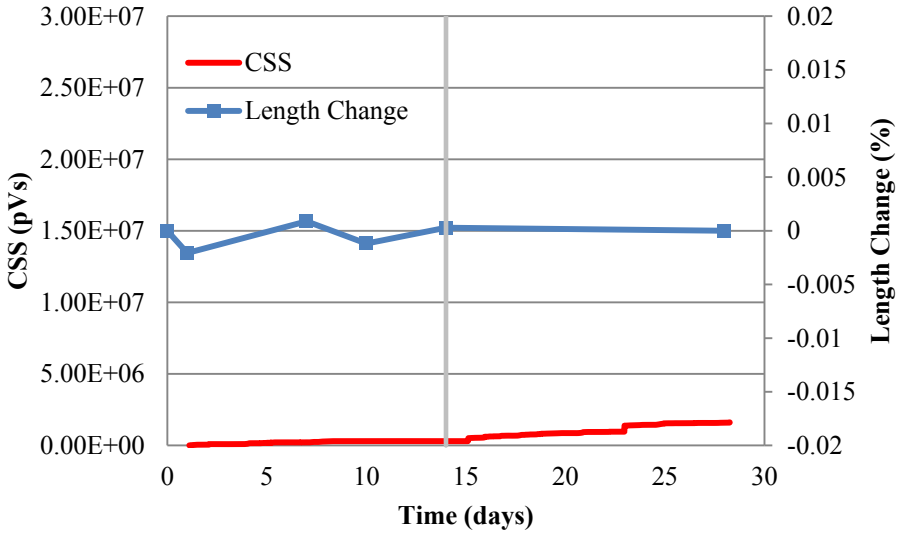

Figure 4.61: Specimen S11 (tested 28 days) – CSS versus time

CHAPTER 5

SUMMARY AND CONCLUSIONS

5.1 SUMMARY AND CONCLUSIONS OF EACH STUDY

A brief summary of each of the research projects presented in this thesis is provided in the following sections along with discussion of the main conclusions that may be drawn from each study.

5.1.1 Performance Assessment of In-situ Precast Approach Slab Systems

This purpose of this research is to assess the performance of precast concrete slabs placed on the approaches of a replacement bridge in Union County, S.C. The use of full depth precast panels in bridge construction has been limited by problems associated with the durability of connection joints between adjacent panels. However, the use of precast concrete in highway and bridge construction is particularly attractive as it offers substantial time savings in the construction schedule in comparison to cast-in-place concrete. The approach slabs were fitted with an improved longitudinal shear key detail consisting of lopped interlocking reinforcement bars. The South Carolina Department of Transportation (SCDOT) is considering the use of this structural system in the future for bridge construction. This research program aims to evaluate the performance of the precast concrete approach slab system and determine the practicality of further implementation as an alternative to current methods. Emphasis is placed on the potential changes in long-term behavior of the approach slab systems due to service loadings.

After 6 months of service, both the Bent One and Bent Four approach slab systems on the replacement bridge over Big Brown Creek in Union, SC appear to be functioning as intended based on long-term strain and displacement measurements as well as strain readings collected during load testing. No cracking or deformations have been observed around shear key joints connecting adjacent precast slabs or in other areas on the approach. Measured strains within precast panels and within shear key joints are generally below the calculated rupture strains for the approach slab system. Displacement readings collected from vibrating wire strain gages were small and indicate negligible movement of the approach slabs relative to the cast-in-place bridge deck. Strains measured during the first load test on the Bent One approach slab system were generally below the calculated rupture strains and indicate that the approach slabs are functioning adequately at this time.

This research project is ongoing. The results from long-term monitoring and load testing to be conducted in the following 12 months will be reported on in the future.

5.1.2 Assessment of Alkali-Silica Reaction Using Acoustic Emisson

An accelerated alkali-silica reaction (ASR) test was designed to examine the ability of acoustic emission (AE) to detect this damage mechanism. ASR is a chemical reaction occurring between alkaline hydroxides from the cement past and certain types of amorphous silica within mineral aggregates. ASR causes an accumulation of internal pressure due to the formation of an expansive gel which leads to swelling and cracking of concrete. AE is highly sensitive to stress waves emitted from sudden release of energy, such as formation of cracks in concrete. This allows it to capture and identify propagating

damage. AE has the potential to detect micro-cracks forming prior to expansion, which can be related to the degree of ASR damage.

The experimental setup consisted of an adapted ASTM C1293 test, twelve specimens of dimensions 3x3x11.25 in. created using a highly reactive aggregate as well as an elevated alkaline content, and 3 control specimens of similar dimensions incorporating innocuous aggregates and low-alkaline cement. The specimens were placed in controlled environment with high temperature and relative humidity to accelerate the ASR reaction. Length change measurements and petrographic examination were performed periodically to detect ASR damage while AE activity was recorded continuously.

The results of this study show that AE is able to detect ASR damage with a good agreement with length change measurements. The specimens containing reactive aggregate, along with elevated alkalinity show a general trend of increasing length which indicates the presence of ASR damage. The results of petrographic analysis have not yet been reported on, however, significant staining was observed on the surface of the ASR affected specimens. Staining and discoloration is often a precursor for ASR induced crack formation at the surface. AE cumulative signal strength also corresponded well with the length change associated with ASR damage. An AE intensity analysis was performed using severity and historic index parameters. The ASR distressed specimens plotted in the higher damage regions of the intensity analysis chart which demonstrates its viability for classification of ASR damage. This research program is ongoing and with the progress of testing, more data will be available which may help in the determination of damage level boundaries.

This study is intended to determine the feasibility of AE for condition assessment of structures subject to ASR deterioration. A more thorough investigation is needed to establish how AE parameters might be used to develop algorithms which can predict the degree of ASR damage that has occurred over a period of time. It is also important for the ASR damage assessment program to have the capability of distinguishing AE related to ASR distress as opposed to other mechanisms such as loading or thermal expansion/contraction.

REFERENCES

Precast/Prestressed Concrete Institute (PCI) Industry Handbook Committee. 1999. PCI Design Handbook, 5th Ed., PCI, Chicago, 1–21.

Clifton, J.R. 1991. Predicting the Remaining Service Life of Concrete. NISTIR 4712. U.S. Department of Commerce, National Institute of Standards and Technology, Gaithersburg, Maryland.

NRC IN 2011-20. 2011. Concrete Degradation by Alkali-Silica Reaction. Nuclear Regulatory Commission (NRC), November 18, Washington, DC.

ASTM C 289-07. 2007. Potential Alkali-Silica Reactivity of Aggregates (Chemical Method). American Society for Testing and Materials, 159-165.

ASTM C 295 / C295M-12. 2012. Petrographic Examination of Aggregates for Concrete. American Society for Testing and Materials, 176-183.

ASTM C1293. 2008. Standard Test Method for Determination of Length Change of Concrete Due to Alkali-Silica Reaction. American Standard for Testing and Materials, 1-7.

ASTM C 1260-07. 2007. Potential Alkali Reactivity of Aggregate (Mortar-Bar Method). American Society for Testing Materials, Philadelphia, 652-655.

Ziehl, P. 2008. Applications of Acoustic Emission Evaluation for Civil Infrastructure. SPIE Proc. SPIE Smart Structures NDE, San Diego, CA, 9.

Pollock, A.A. 1986. Classical Wave Theory in Practical AE Testing. Progress in AE III, Proceedings of the 8th International AE Symposium, Japanese Society for Nondestructive Testing, 708-721.

ElBatanouny, M.K, Larosche, A., Mazzoleni, P., Ziehl, P.H, Matta, F., and Zappa, E. 2012. Identification of Cracking Mechanisms in Scaled FRP Reinforced Concrete Beams using Acoustic Emission. Experimental Mechanics, DOI 10.1007/s11340-012-9692-3, November (online).

Mangual, J., ElBatanouny, M. K., Ziehl, P., and Matta, F. 2013. Acoustic-Emission-Based Characterization of Corrosion Damage in Cracked Concrete with PrestressingStrand, ACI.Materials.Journal, 110(1),89.

Chi, M., Saadat, S.A. 1985. Precast Concrete Modular Bridge Deck Case Studies. Final Report submitted to Federal Highway Administration. Report No. FHWA-TS-85-232.

Issa, M., Idriss, A-T., Kaspar, I., Khayyat,S. 1995. Full Depth Precast, Prestressed Concrete Bridge Deck Panels. PCI Journal, Vol. 40, No. 1, 59-80.

Issa, M., Yousif, A., Issa, M.A., Kaspar, I., Khayyat, S. 1995. Field Performance of Full Depth Precast Concrete Panels in Bridge Deck Reconstruction. PCI Journal, Vol. 40, No. 3, May-Jun 1995, 82-108.

Markowski, S. 2005. Experimental and Analytical Study of Full-depth Precast / Prestressed Concrete Deck Panels for Highway Bridges. MS Thesis, Department of Civil and Environmental Engineering, University of Wisconsin-Madison.

Merritt D., B. Frank McCullough, Ned H. Burns, and Anton K. Schindler. 2000. The Feasibility of Using Precast Concrete Panels to Expedite Highway Pavement Construction. ReportFHWA/TX-01/1517-1.

Li, L., Ma, Z., Griffey, M., & Oesterle, R. 2010. Improved Longitudinal Joint Details in Decked Bulb Tees for Accelerated Bridge Construction: Concept Development. Journal of Bridge Engineering, 327-336

Stanton, J., and Mattock, A.H. 1986. Load distribution and connectiondesign for precast stemmed multibeam bridge superstructures. Rep. No. 287, TRB, National Research Council, Washington, D.C.

Ma, Z., et al. 2007. Field test and 3D FE modeling of decked bulb-tee bridges. J. Bridge Eng., 123, 306–314.

Martin, L. D., and Osborn, A. E. N. 1983. Connections for modular precast concrete bridge decks. Rep. No. FHWA/RD-82/106, Federal Highway Administration, Washington, D.C.

Swamy, RN 1998: The Alkali-Silica Reaction in Concrete. New York, Blackie and Son Ltd.

Stanton, T.E. 1941. Expansion of concrete through reaction between cement and aggregate. Am. Soc. Civil Eng. Trans, Paper 2129 and its Discussion, 54–126.

Farney, J. A., and Kosmatka S. H. 1997. Diagnosis and Control of Alkali-Aggregate Reactions in Concrete. Concrete Information Series No. IS413.01T, Portland Cement Association, Skokie, IL.

Nicholas, W. B. 2012. Understanding Cement: An Introduction to Cement Production, Cement Hydration and Deleterious Processes in Concrete. WHD Microanalysis Consultants

Leming, M. L. 1996. Alkali-Silica Reactivity: Mechanisms and Management. Mining Engineering, Vol. 48, No. 12, 61-64.

Prezzi, M., Monteiro, Paulo J. M. and Sposito, Garrison. 1997. The Alkali-Silica Reaction, Part I: Use of the Double-Layer Theory to Explain the Behavior of Reaction-Product Gels. ACI Materials Journal, Vol. 94, No. 1, 10-17.

Stanton, T.E. 1940 Expansion of Concrete through Reaction between Cement and Aggregate. Proceedings, Am. Soc. of Civil Engineers, Vol. 66, 1781–1811.

ASTM C 227-10. 2010. Potential Alkali Reactivity of Cement-Aggregate Combinations (Mortar-Bar Method), American Society for Testing and Materials, 129-133.

Bérubé, M.A. & Fournier, B. 1992. Accelerated test methods for alkali-aggregate reactivity. In CANMET ACI International Symposium on Advances in Concrete Technology, Athens, Greece, 42.

Touma, W.E., Fowler, D.F. and Carrasquillo, R.L. 2001. Alkali-silica reaction in Portland cement concrete: Testing methods and mitigation alternatives. Report ICAR 301-1F, International Center for Aggregates Research, Austin, Texas.

Thomas, M.D.A, M.H. Shehata. 2004. Use of blended cements to control expansion of concrete due to alkali silica reaction, fly ash, silica fume, slag, and natural pozzolans in concrete. Proceedings of the Eighth CANMET/ACI International Conference, Supplementary Papers, 591–607.

ASTM C150 / C150M – 12. 2012. Standard Specification for Portland Cement. American Society for Testing and Materials, 10-13.

Rivard P., Bérubé M.A., Ballivy G., Ollivier J. 2003. Effect of drying–rewetting on the alkali concentration of the concrete pore solution. Cement and Concrete Research, Volume 33, Issue 6, 927-929.

ASTM E1316. 2006. Standard Terminology for Nondestructive Examinations. American Society for Testing and Materials, 1-33.

Hamstad, M. 1986. A Review: Acoustic Emission, a Tool for Composite-Materials Study. Experimental Mechanics 26(1), 7-13.

Fowler, T., Blessing, J., and Conlisk, P. 1989. New Directions in Testing. Proc. 3rd International Symposium on AE from Composite Materials, Paris, France.

CARP. 1999. Recommended Practice for Acoustic Emission Evaluation of Fiber Reinforced Plastic (FRP) Tanks and Pressure Vessels. Draft I, The Committee on Acoustic Emission for Reinforced Plastics (CARP), A Division of the Technical Council of the American Society for Nondestructive Testing, Inc., Columbus.

ASTM C39 / C39M – 12a. 2012. Standard Test Method for Compressive Strength of Cylindrical Concrete Specimens. American Society for Testing and Materials, 1-12.

ASTM C469 / C469M – 10. 2010. Standard Test Method for Static Modulus of Elasticity and Poisson's Ratio of Concrete in Compression. American Society for Testing and Materials, 1-12.

ASTM C31 / C31M – 12. 2012. Standard Practice for Making and Curing Concrete Test Specimens in the Field. American Society for Testing and Materials, 1-7.

ASTM C143 / C143M – 12. 2012. Standard Test Method for Slump of Hydraulic-Cement Concrete. American Society for Testing and Materials, 1-5.

Building Code Requirements for Structural Concrete (ACI 318-08) and Commentary. 2008. An ACI Standard. Farmington Hills, MI.: American Concrete Institute

Idrissi, H., and Limam, A. 2003. Study and characterization by acoustic emission and electrochemical measurements of concrete deterioration caused by reinforcement steel corrosion. NDT & E International, 36(8), 563-569.

Assouli, B., Simescu, F., Debicki, G., and Idrissi, H. 2005. Detection and identification of concrete cracking during corrosion of reinforced concrete by acoustic emission coupled to the electrochemical techniques. NDT & E International, 38(8), 682-689.

ASTM C157 / C157M – 08. 2008. Standard Test Method for Length Change of Hardened Hydraulic-Cement Mortar and Concrete. American Society for Testing and Materials, 1-5.

ASTM C29 / C29M – 09. 2009. Standard Test Method for Bulk Density ("Unit Weight") and Voids in Aggregate. American Society for Testing and Materials, 1-13.

ASTM C114 – 13. 2013. Standard Test Methods for Chemical Analysis of Hydraulic Cement. American Society for Testing and Materials, 1-16.

ASTM C192 / C192M - 13a. 2013. Standard Practice for Making and Curing Concrete Test Specimens in the Laboratory. American Society for Testing and Materials, 7-20.

ASTM C138 / C138M - 13a. 2013. Standard Test Method for Density (Unit Weight), Yield, and Air Content (Gravimetric) of Concrete. American Society for Testing and Materials, 1-9.

ASTM C231 / C231M – 10. 2010. Standard Test Method for Air Content of Freshly Mixed Concrete by the Pressure Method. American Society for Testing and Materials, 1-9.

Fowler, T., Blessing, J., and Conlisk, P. 1989. New Directions in Testing. Proc. 3rd International Symposium on AE from Composite Materials, Paris, France.

ElBatanouny, M., Mangual, J., Ziehl, P., and Matta, F. 2011. Corrosion Intensity Classification in Prestressed Concrete using Acoustic Emission Technique. Proc. American Society for Nondestructive Testing (ASNT) Fall Conference and Quality Testing Show 2011, Palm Springs, CA. October 24-28, 10.